Observation of a Lee-Huang-Yang Fluid

Thomas Guldager Skov
Department of Physics and Astronomy
Aarhus University, Denmark

PhD Thesis
July 2021

Abstract

Bose-Einstein condensates (BEC) serve as excellent platforms for studying quantum physics in regimes that are otherwise inaccessible, since both internal and external parameters are highly controllable. In particular, the interactions between the constituent particles can be tuned arbitrarily by the use of Feshbach resonances, which enables many different research directions. In the studies presented in this thesis, BECs of ^{39}K are used to study three topics, which are made possible by the rich Feshbach resonance structure of the atomic species.

In the first experiment, the physics of impurities interacting with a bosonic medium is studied. The impurity picture is realized by transferring a small fraction of the BEC population into another state and the BEC thus composes a bosonic environment for the impurities. The experiments investigate the dynamical properties of the system across different interaction strengths and reveal how the system evolves from an initial superposition state into polaron quasiparticles. These experiments serve as a quantum simulation of a phenomenon that is challenging to study in its original context of solid state physics.

The second direction constitutes the experimental realization of a Lee-Huang-Yang (LHY) fluid. In this experiment, the interactions strengths and atom numbers in a two-component BEC are tuned such that the usually dominant mean-field interactions cancel. The interactions of the system are then governed by the next-order contribution to the energy, which originates in quantum fluctuations. The dominant contribution from quantum fluctuations manifests in the monopole oscillation frequency of the system, which is measured and found to agree with detailed simulations. The realized LHY fluid serves as a platform for new quantum simulation experiments and for observing even-higher order effects.

The final study concerns BECs with vanishing two-body interactions. In this case, the interactions in the system are governed by three-body scattering, which influence the collective behaviour similar to the previous experiment. Measuring this effect using ^{39}K requires the production of BECs at a larger magnetic field strength than previously done using the experimental apparatus, and within the thesis, current progress towards such an experiment is described.

Resumé

Danish Abstract

Bose-Einstein-kondensater (BEC) udgør en fremragende platform for undersøgelser af kvantefysikken i regimer, som ellers er svært tilgængelige, da både interne og eksterne parametre kan kontrolles til høj præcision. I særdeleshed kan vekselvirkningsstyrken mellem BEC'ets partikler justeres arbitrært gennem brugen af Feshbach resonanser, hvilket muliggør mange forskellige forskningsområder. I denne afhandling anvendes BEC'er af ^{39}K til at studere tre forskellige emner, der alle mulliggøres af denne kaliumisotops særegne Feshbach resonansstruktur.

I det første eksperiment undersøges fysikken af urenheder som interagerer med et bosonisk medie. Urenhedsbilledet realiseres ved at overføre en lille brøkdel af BEC-populationen til en anden tilstand, og BEC'et udgør således et bosonisk miljø for urenhederne. I eksperimenterne undersøges systemets dynamiske egenskaber for forskellige vekselvirkningsstyrker, og det observeres hvordan systemet udvikler sig fra en superpositionstilstand til polaroniske kvasipartikler. Eksperimenterne udgør en kvantesimulering af et fænomen som ellers er udfordrende at undersøge indenfor faststoffysikken, som er dets oprindelige kontekst.

Det andet forskningsprojekt udgør den eksperimentelle observation af en Lee-Huang-Yang (LHY) -fluid. I dette eksperiment justeres vekselvirkningsstyrkerne og atomtallene i et tokomponent-BEC, således at de normalt dominerende middelfeltsinteraktioner udgår. Systemets vekselvirkninger styres da af bidraget til energien af næste orden, som stammer fra kvantefluktuationer. Det dominerende bidrag fra kvantefluktuationer manifesterer sig i systemets monopoloscillationsfrekvens, og denne måles til at være i overensstemmelse med detaljerede simuleringer. Den realiserede LHY-fluid udgør en lovende platform for nye kvantesimuleringseksperimenter og til målinger af effekter af endnu højere orden.

Det sidste studie omhandler BEC'er med forsvindende tolegemeinteraktioner. I dette tilfælde styres systemets interaktioner af trelegemespredning, hvilket influerer dets kollektive opførsel på lignende måde som i det forrige eksperiment. For at måle denne effekt med ^{39}K er det nødvendigt at producere BEC'er ved højere magnetfeltsstyrker end der før er anvendt med det eksperimentelle apparatur. I denne afhandling beskrives fremskridt mod et sådant eksperiment.

Preface

This thesis culminates four years of research performed during my time in the Ultracold Quantum Gases Group lead by Jan J. Arlt. The research was carried out in the MIX laboratory, and explores the physics of ^{39}K Bose-Einstein condensates with tunable interactions.

My path into the research group began when I first met Jan, who taught the course in atomic, molecular, and optical physics in my third year as a Bachelor student. At that point, I knew that I wanted to do research in experimental physics, however, I was not sure about which subject to pursue. I remember Jan showing pictures from the lab and explaining how today physicists are able to manipulate atoms in order to study fundamental quantum mechanics experimentally.

My discussions with Jan lead me to doing my Bachelor's project in his research group in the first half of 2016. The project consisted of designing and constructing a laser system for eliminating the gravitational sag between ultracold samples of Rb and K, and was performed under supervision of Lars J. Wacker, who at the time was a postdoc in the group. Lars taught me how to work with optics and lasers, and his passion for research was a big inspiration.

After finishing my Bachelor's project, I participated in the summer student programme at CERN. Here I got my first real experience of working as an experimental physicist at the ISOLTRAP experiment. I want to thank my supervisor Vladimir Manea, and the rest of the team for being so welcoming and inspiring me to continue in experimental physics, even though I did not end up in nuclear physics.

In the first year of my Master's studies, I began to realize just how fascinating ultracold quantum gas experiment are. It never ceases to amaze me how BEC experiments simultaneously serve as examples of textbook quantum physics while also enabling research at the frontiers of physics. I therefore did not hesitate when Jan asked me to join the group as a PhD student on the MIX experiment, of which I was already familiar based on my Bachelor's project. Thanks for giving me the opportunity to study such a fascinating topic, for your supervision, and for your understanding during the inevitable stressful periods of a PhD project.

Most of my work in the group was performed in close collaboration with Nils B. Jørgensen and Magnus G. Skou who, together with myself, made up the MIX team throughout a large part of my PhD studies. Thanks to both of you for making the time in the MIX lab such an enjoyable experience. Thanks to Nils for your mentoring, and to Magnus for sharing the ups and downs of running a quantum gas experiment. I will really miss our times in the lab. In the last year, Andreas M. Morgen joined the team as the newest PhD student. It has been a pleasure to work together on the new research projects and I wish you the best of luck going forward. I am sure that great results are to come.

In addition to those mentioned above, the extended research group composed of the MIX, Lattice, and HiRes teams have featured some fantastic people throughout the last four years. Thanks to Theis, Anders, Mick, Mikkel, Toke, Søren, Jeppe, Claus, Robert, Ottó, Jens, Carrie, and Dipto – you have been phenomenal colleagues. Special thanks go to Carrie, Andreas, Robert, Magnus, Jan, and Mick for proofreading parts of the thesis and providing valuable feedback.

During my time as a PhD student, I have also been a part of the organizing groups for the annual PhD day, and the 2021 edition of the Young Atom Opticians conference. Thanks to everyone who helped out and made the events possible despite the coronavirus pandemic. It was a real pleasure to meet and work together with so many people from different research groups.

Finally, I want to thank my family and friends for their support during my PhD studies, and a very special thanks goes to Emilie for her unwavering support and for listening to my frustrations while going through similar challenges in her own studies.

Thomas Guldager Skov,
Aarhus, Wednesday July 28th, 2021.

List of Publications

M. G. Skou, T. G. Skov, N. B. Jørgensen, K. K. Nielsen, A. Camacho-Guardian, T. Pohl, G. M. Bruun, and J. J. Arlt, Non-equilibrium quantum dynamics and formation of the Bose polaron, Nature Physics **17**, 731–735 (2021).

M. G. Skou, T. G. Skov, N. B. Jørgensen, and J. J. Arlt, Initial Dynamics of Quantum Impurities in a Bose–Einstein Condensate, Atoms **9**, 22 (2021).

T. G. Skov, M. G. Skou, N. B. Jørgensen, and J. J. Arlt, Observation of a Lee-Huang-Yang Fluid, Physical Review Letters **126**, 230404 (2021).

M. G. Skou, K. K. Nielsen, T. G. Skov, A. M. Morgen, N. B. Jørgensen, A. Camacho-Guardian, T. Pohl, G. M. Bruun, and J. J. Arlt, Life and Death of the Bose Polaron, in preparation.

Contents

CHAPTER 1

Introduction

Throughout the twentieth century, the understanding of the physical world was revolutionized by the development of quantum mechanics, which describes the physics of objects at small length scales. Its name is derived from one of its core concepts, namely that physical quantities are restricted to certain values and are therefore *quantized*. This concept was first employed by M. Planck who hypothesized the quantization of energies to explain the blackbody radiation spectrum [1]. Soon after, it was used by A. Einstein to explain the photoelectric effect [2], and in 1913, N. Bohr hypothesized the quantization of the hydrogen atom [3], which provided an explanation for its emission spectrum.

Another central concept of quantum mechanics is that of *wave-particle duality*, which says that quantum mechanical objects may be described as either waves or particles depending on the context, as exemplified by the light quanta used by Einstein to explain the photoelectric effect. These light quanta can be considered as particles, called photons, and carry momentum as measured by A. Compton in experiments on inelastic scattering of X-rays on electrons [4]. In his 1924 PhD thesis, L. de Broglie postulated that *all* matter has characteristics of both particles and waves, and this remarkable statement was verified experimentally in the following years, where diffraction phenomena were observed using electrons [5, 6] and atoms [7]. Consequently, quantum mechanical objects such as electrons and atoms are described by *wave functions* $\Psi(\mathbf{r}, t)$, which are spread out in space, rather than as localized particles, and these wave functions can display wave phenomena such as diffraction and interference. The matter-wave concept was extended by E. Schrödinger, who introduced the equation governing the physics of quantum mechanical wave functions [8], and in 1926, the wave function was interpreted statistically by M. Born with its modulus square $|\Psi(\mathbf{r}, t)|^2$ describing the probability of finding the particle at position $\mathbf{r}$ at time t [9].

One of most striking examples of a matter-wave phenomenon is perhaps the concept of *Bose-Einstein condensation*. Based on work by S. N. Bose on the statistics of photons [10], Einstein extended the theory to massive particles and concluded that below a critical temperature, a macroscopic fraction of the population would be in the quantum mechanical ground state [11]. The resulting state of matter has since become known as a Bose-Einstein Condensate (BEC) and constitutes a macroscopic quantum mechanical object where a large number of atoms all occupy same coherent matter wave. Moreover, a BEC is also macroscopic in terms of its size, which for dilute gases is large enough to be probed by optical means [12].

In 1995, more than 70 years after Einstein's original proposal, the techniques for cooling and confinement of neutral atoms had finally matured sufficiently to enable the production of BECs. This was exemplified by three different research groups independently realizing BECs in ^{87}Rb, [13],^{23}Na [14], and ^{7}Li [15] within the same year. Four years later, the first degenerate Fermi gas was realized in ^{40}K [16]. In 2001, the Nobel prize was awarded to E. Cornell, W. Ketterle, and C. Wieman for *"the achievement of Bose-Einstein condensation in dilute gases of alkali atoms, and for early fundamental studies of the properties of the condensates"* [17]. Today, more than 100 research groups worldwide investigate the physics of BECs and their technological applications [18].

In addition to improving the fundamental understanding of the physical world, the development of quantum mechanics lead to significant technological achievements such as the transistor [19] and the laser [20], which served as the technological foundation of the information age. The scientific and technological developments throughout the twentieth century are known together as the first quantum revolution, and with the coming of the new millennium, a second quantum revolution has begun [21]. Today, systems are engineered to have quantum mechanical properties, which enable new types of computing [22], cryptography [23], and sensing [24], as well as *quantum simulation*, as first envisioned by R. Feynman in 1982 [25].

Feynman argued that since nature is quantum mechanical, the platform on which one attempts to simulate it, must also be quantum mechanical. In particular, BECs serve as an excellent platform for quantum simulation experiments, since both the internal and external degrees of freedom are highly controllable. This is exemplified by how the external potential provided by off-resonant laser light [26] can be tailored arbitrarily using beam shaping techniques and by the tunability of the interatomic interactions via magnetic Feshbach resonances [27]. This controllability enables the simulation of other quantum systems in regimes that are otherwise inaccessible, and quantum simulation experiments find application in such diverse fields as solid state physics, quantum chemistry, high-energy physics, and cosmology [28]. In addition to the platform provided by BECs, quantum simulation experiments can also be realized in systems such as ultracold atoms in optical lattices [29, 30], trapped ions [31], photons [32], and superconducting circuits [33].

In this thesis, BECs of ^{39}K are employed to explore three different research directions, which all make use of the ability to tune the interaction strength, parametrized by the scattering length, via Feshbach resonances.

The first considers the general scenario of an impurity interacting with a surrounding medium, where the impurity-medium interactions can lead to the formation of polaron quasiparticles. This scenario was considered by L. Landau and S. I. Pekar in the context of electrons interaction with a crystal lattice [34–36] and has since found numerous applications with examples ranging from high–T_C superconductors [37] to Λ-particles in nuclear matter [38]. Experimentally, the polaron scenario has been realized in both fermionic [39–47] and bosonic [48–50] quantum gases. These experiments serve as a prime examples of quantum simulations, since the impurity-medium interaction strength can be tuned arbitrarily and the diluteness of ultracold gases results in density-dependent timescales being sufficiently large for time-resolved experiments.

In this project, the dynamical evolution of impurities immersed in a BEC was studied, and the results were published in Refs. [51, 52]. The impurity scenario was realized by transferring a small fraction of the BEC population into a different internal state with the majority component serving as the medium. By using an interferometric sequence, the impurity coherence was measured from weak to strong impurity-medium interactions. The dynamical evolution of the impurity coherence reflects the underlying scattering processes between the impurity and medium atoms, and the measurement thus enabled tracking the evolution from an initial coherent superposition state to the emergence of polaronic quasiparticles.

The second research direction concerns the Lee-Huang-Yang (LHY) fluid proposed by our group in 2018 [53], which was experimentally realized in this work and lead to the publication of Ref. [54]. The thesis title is based on this project since it contains my largest contribution. By tuning the atom numbers and interaction strengths in a two-component BEC, the usually dominant mean-field contribution to the energy can be cancelled such that the interactions in the system are governed by the next-order contribution to the energy density, which originates in quantum fluctuations. This contribution was first calculated in 1957 by Lee, Huang, and Yang [55] and is therefore known as the LHY correction. In recent years, the LHY correction has been employed to realize quantum droplets [56–61] in systems that would otherwise collapse due to attractive mean-field interactions. Similar experiments were performed using dipolar quantum gases [62–65], which most recently, culminated in the observation of supersolid behaviour in these systems [66–68].

The LHY fluid was realized experimentally in a mixture of two internal states of ^{39}K, and the collective behaviour of the system was measured. The experimental results were compared to detailed simulations of the system, taking into account the experimental preparation method and the effect of inelastic losses, which confirmed that the interactions are governed by the LHY correction. The realized LHY fluid serves as a promising platform for new quantum simulation experiments since the interactions scale differently compared to a typical BEC, and it may enable the measurement of even higher-order effects.

The final research direction also considers a system with vanishing mean-field interactions, however, in this case, the scattering length is tuned to zero such that both mean-field and LHY contributions vanish. The interactions of the system are then governed by three-body collisions characterized by the three-body scattering hypervolume [69, 70]. Similar to the LHY fluid, the influence of three-body interactions is predicted to manifest in the collective excitations from which the size of the three-body scattering hypervolume can be inferred [71]. Measuring this effect thus serves as a natural continuation of the previous research project. The experimental realization of this scenario, however, requires the production of BECs at larger magnetic fields than previously achieved using the experimental apparatus. The procedure must therefore be changed accordingly, and in this work, progress towards this experiment is presented, which includes the successful production of ^{39}K BECs at the required magnetic field strength.

Thesis Outline

The remaining thesis is structured as follows:

Chapter 2 *Bose-Einstein Condensation in Dilute Atomic Gases.*

The essential theory required to understand Bose-Einstein condensation is presented along with the basics of scattering theory, which enables a description of the condensed state and its elementary excitations.

Chapter 3 *Atom-Light Interactions.*

The basic interaction between atoms and electromagnetic radiation is presented. It is shown how coherent laser radiation can be used to manipulate the internal state of atoms, and how light can be used to cool and confine atomic samples, which enables the production of BECs.

Chapter 4 *Production of ^{39}K Bose-Einstein Condensates.*

An overview of the existing experimental apparatus, which is capable of producing BECs of ^{39}K, ^{41}K, and ^{87}Rb is given. The recently added optical setup for a third trapping beam is described in more detail, and the resulting trap potential is characterized.

Chapter 5 *Impurity Dynamics.*

Experiments on the dynamical evolution of impurities interacting with a surrounding BEC are presented. By measuring the impurity coherence using an interferometric method, different regimes of impurity scattering are identified and the evolution towards polaron quasiparticles is observed.

Chapter 6 *Lee-Huang-Yang Fluid.*

The experimental realization of a Lee-Huang-Yang fluid is presented. Detailed simulations of the system are performed and compared to experimental measurements of the collective behaviour, which confirm that the system interactions are governed by the LHY correction.

Chapter 7 *Progress on Hypervolume Experiments.*

Progress towards a new experiment measuring the three-body scattering hypervolume is presented. ^{39}K BECs are successfully produced and imaged under the necessary experimental conditions, and preparatory measurements are described.

Chapter 8 *Conclusion and Outlook.*

The results of PhD project are summarized and an outlook for future research directions is provided.

CHAPTER 2

Bose-Einstein Condensation in Dilute Atomic Gases

The wave-like nature of particles becomes relevant when the corresponding wavelength of the particle is comparable to the characteristic size of the system. For massive particles, the thermal de Broglie wavelength

$$\lambda_T = \sqrt{\frac{2\pi\hbar^2}{mk_\mathrm{B}T}}, \tag{2.1}$$

can be used to describe the spatial extent of the wave function, where $\hbar$ is the reduced Planck constant, m is the mass, k_B is the Boltzmann constant, and T is the temperature. For quantum mechanical effects to become important, λ_T must be on the order of the interparticle spacing.

The free electrons in a solid can be considered as an example. The lattice spacing in a typical solid is around $d = 0.3\,\mathrm{nm}$ [72], so setting $\lambda_T = d$ and inserting the electron mass yields $T \lesssim 6 \times 10^4\,\mathrm{K}$. The free electrons in a solid are thus definitely quantum mechanical.

Conversely, for a dilute gas with density $n \sim 1 \times 10^{14}\,\mathrm{cm}^{-3}$, temperatures on the order of µK are necessary for the wave functions to start overlapping[1].

---

[1] The used value for the density is typical of an atomic oven [73].

It is thus clear that dilute atomic gases must be cooled down to very low temperatures for quantum mechanical effects to become important.

When this is the case, two or more identical particles are likely to occupy the same single-particle state, and the quantum statistics of the particles therefore becomes relevant. It is therefore important whether the particles in question are bosons or fermions. Bosonic wave functions are symmetric under particle exchange, whereas fermionic wave functions are anti-symmetric. As a consequence, indefinitely many bosons may occupy the same single-particle state, whereas two identical fermions cannot, since then the total wave function equals zero.

In statistical physics, this fact reveals itself when looking at the average number of particles in a state ν. The resulting Fermi-Dirac (FD) and Bose-Einstein (BE) distribution functions look as follows,

$$f_{\mathrm{FD}}(\epsilon_\nu) = \frac{1}{e^{(\epsilon_\nu-\mu)/k_{\mathrm{B}}T}+1} \quad \text{(fermions)}, \tag{2.2}$$

$$f_{\mathrm{BE}}(\epsilon_\nu) = \frac{1}{e^{(\epsilon_\nu-\mu)/k_{\mathrm{B}}T}-1} \quad \text{(bosons)}, \tag{2.3}$$

where ϵ_ν is the energy of state ν and μ is the chemical potential. In the limit of high temperatures, $\mu \ll \epsilon_0$ such that $e^{(\epsilon_\nu-\mu)/k_{\mathrm{B}}T} \gg 1$ for all ϵ_ν. In this case, both distributions reduce to the Maxwell-Boltzmann distribution $f(\epsilon_\nu) \approx e^{-(\epsilon_\nu-\mu)}$, highlighting that in this limit, the quantum statistics of the particles is unimportant.

Conversely, for low temperatures, the subtle sign difference of the distribution functions Eqs. (2.2) and (2.3) turns out to have dramatic consequences as will be revealed in the following sections. In particular, for the bosonic atoms considered in this thesis, a macroscopic population condense in the quantum mechanical ground state below a critical temperature.

The remainder of the chapter is structured as follows. In Sec. 2.1, the basic theory for Bose-Einstein condensation of non-interacting particles is described. After this, the basic concepts of scattering theory are presented in Sec. 2.2 as a prerequisite for understanding the interactions in ultracold gases and BECs. The derivation of the celebrated Gross-Pitaevskii equation for the condensed state is then outlined in Sec. 2.3 and some of its applications are discussed. Finally, in Sec. 2.4 the spectrum of elementary excitations in a BEC is presented, leading to the Lee-Huang-Yang correction to the ground state energy.

2.1 Bose-Einstein Condensation of Non-Interacting Particles

The basic properties of BECs such as the critical temperature and condensate fraction can be derived by considering a gas of non-interacting bosons. The derivations within this section are based on a combination of the books by C. J. Pethick and H. Smith [12] and D. V. Schroeder [74], as well as a set of excellent lecture notes by G. M. Bruun [75].

The starting point is a system of non-interacting bosons in thermal equilibrium, distributed across states ν according to Eq. (2.3). From Eq. (2.3) it is evident that $\mu \leq \epsilon_0$, for the Bose distribution function to be positive when evaluated for the lowest-lying state. The chemical potential can be found from the total atom number by summing up the occupancy of each single-particle state. By setting the ground state energy to zero, $\epsilon_0 = 0$, the total atom number can be written as

$$N = \frac{1}{e^{-\mu/k_\mathrm{B}T} - 1} + \int_0^\infty \mathrm{d}\epsilon \, \frac{g(\epsilon)}{e^{(\epsilon-\mu)/k_\mathrm{B}T} - 1} = N_0 + N_\mathrm{ex} \, , \tag{2.4}$$

where the occupancy of the lowest lying state N_0 has been separated out explicitly. The number of atoms in excited states N_ex can be determined in a semi-classical approximation assuming that N is large and that the temperature is large compared to the level spacing $T \gg \Delta\epsilon/k_\mathrm{B}$, which allows the sum over excited states to be converted into an integral. Here, $g(\epsilon)$ is the density of states, which describes the number of single-particle states per unit energy. Equation (2.4) determines the chemical potential μ, which increases from negative values towards 0 as the temperature decreases while keeping N fixed. This in turn, causes the first term of Eq. (2.4) to increase, which results in a macroscopic population of the ground state.

2.1.1 Critical Temperature

The condensation occurs at the critical temperature T_C, which is determined from the lowest temperature, where all particles can be distributed among the excited states. The integral over excited states in Eq. (2.4) has its maximum value for $\mu = 0$, so T_C can be determined by setting $\mu = 0$ and $N_0 = 0$,

$$N = N_\mathrm{ex}(T_\mathrm{C}, \mu = 0) = \int_0^\infty \mathrm{d}\epsilon \, \frac{g(\epsilon)}{e^{\epsilon/k_\mathrm{B}T_\mathrm{C}} - 1} . \tag{2.5}$$

The density of states depends on the external potential confining the atoms, and here the most relevant cases are The 3D homogeneous system of volume $\mathcal{V}$ (3D box) and the 3D harmonic oscillator potential of frequencies ω_i $(i = x, y, z)$. For these cases, the density of states are

$$g(\epsilon) = \frac{\mathcal{V} m^{3/2}}{\sqrt{2}\pi^2\hbar^3}\epsilon^{1/2}, \quad \text{3D box,} \tag{2.6}$$

$$g(\epsilon) = \frac{\epsilon^2}{2\hbar^3\omega_x\omega_y\omega_z}, \quad \text{3D harmonic oscillator.} \tag{2.7}$$

The density of states can generally be written in the form $g(\epsilon) = C_\alpha \epsilon^{\alpha-1}$, where C_α is a constant and $\alpha = 3/2$ and 3 for the 3D box and harmonic oscillator, respectively. The integral in Eq. (2.5) has solution

$$N = C_\alpha \Gamma(\alpha)\zeta(\alpha)(k_\mathrm{B} T_\mathrm{C})^\alpha, \tag{2.8}$$

where $\Gamma(\alpha)$ is the Gamma function and $\zeta(\alpha)$ is the Riemann zeta function. The critical temperatures for the two cases are then given by

$$k_\mathrm{B} T_\mathrm{C} = \frac{2\pi}{\zeta(3/2)^{2/3}}\frac{\hbar^2 n^{2/3}}{m} \approx 3.31\frac{\hbar^2 n^{2/3}}{m}, \quad \text{3D box,} \tag{2.9}$$

$$k_\mathrm{B} T_\mathrm{C} = \frac{\hbar\bar{\omega}N^{1/3}}{\zeta(3)^{1/3}} \approx 0.94\hbar\bar{\omega}N^{1/3}, \quad \text{3D harmonic oscillator,} \tag{2.10}$$

where

$$\bar{\omega} = (\omega_x\omega_y\omega_z)^{1/3} \tag{2.11}$$

is the geometric mean of the harmonic oscillator frequencies.

Before moving on, it is worthwhile to reflect on the above results for the critical temperature. In deriving Eqs. (2.9) and (2.10), the temperature was assumed to be larger than the level spacing, $T_\mathrm{C} \gg \Delta\epsilon/k_\mathrm{B}$. Bose-Einstein condensation is thus a remarkable consequence of the quantum statistics of the bosonic particles. For a system obeying Maxwell-Boltzmann statistics, particles would also pile up in the ground state for $T \to 0$, however this would only happen for $k_\mathrm{B} T \ll \Delta\epsilon$. As such, the large critical temperature for

Bose-Einstein condensation is a direct consequence of the counting statistics coming from the symmetry requirement of the bosonic wave function and is thus a macroscopic quantum mechanical effect.

In the beginning of the chapter, it was stated that the thermal de Broglie wavelength must be on the order of the interparticle spacing for the quantum mechanical nature of the particles to become important. This criterion can be written in terms of the phase-space-density $\mathrm{PSD} = \lambda_T^3 n$, defined as the number of particles within a cube of sides λ_T. Evaluating the phase-space-density at T_C for a 3D box yields $\mathrm{PSD} = \zeta(3/2) \approx 2.612$, and it must therefore approach unity for Bose-Einstein condensation to occur.

2.1.2 Condensate Fraction

The fraction of atoms in the condensate below T_C , can be determined by first considering the number of atoms in excited states

$$N_\mathrm{ex} = C_\alpha \Gamma(\alpha)\zeta(\alpha)(k_\mathrm{B} T)^\alpha. \tag{2.12}$$

Dividing by Eq. (2.8) for the critical temperature and using that $N_\mathrm{ex}(T) = N - N_0(T)$ then yields

$$N_0 = N\left[1 - \left(\frac{T}{T_\mathrm{C}}\right)^\alpha\right] \tag{2.13}$$

for the number of particles in the condensate with α determined by the external potential.

As shown here, several important properties of BECs can be calculated from the assumption of non-interacting atoms. Including finite particle numbers and interactions smoothes out the BEC transition [76], however, the critical temperature and condensate fraction derived here hold to a good approximation [77].

2.2 Scattering in Atomic Gases

In the previous section, the dilute gas consisted of non-interacting particles. In reality, interactions between the atoms in the gas have significant impact on the wave function of the condensate, and in certain cases it can even cause it to collapse as described in Sec. 2.3. In this section the basics of scattering theory are presented based on a combination of the books [12, 72, 78, 79]. Using the method of partial waves, it is shown how the scattering cross section depends on a single parameter, called the scattering length. It is furthermore shown how this parameter can be tuned by an external magnetic field, which directly enables the research directions considered in Chs. 5 to 7 of this thesis.

The scattering of two distinguishable particles is considered. In centre-of-mass (COM) coordinates, the wave function for the relative motion can be written as

$$\psi = e^{i\mathbf{k}\cdot\mathbf{r}} + \psi_{\mathrm{sc}}(\mathbf{r}), \tag{2.14}$$

where the first term is an incoming plane wave with wave vector **k** describing the COM motion, the second term is a scattered wave describing the relative motion, and **r** is the relative coordinate of the particles. For large interatomic distances, the scattered wave is an outgoing spherical wave. The wave function then becomes

$$\psi = e^{ikz} + f(\theta)\frac{e^{ikr}}{r}, \tag{2.15}$$

where the relative velocity of the incoming wave has been chosen as the z-direction and the scattering amplitude $f(\theta)$ is a function of only the scattering angle θ, when considering scattering in a spherically symmetric potential.

In the low energy limit valid for ultracold atomic gases $k \to 0$ and $f(\theta) \to -a$, where a is a constant called the *scattering length.* Inserting this into Eq. (2.15) then yields

$$\psi = 1 - \frac{a}{r}, \tag{2.16}$$

and a thus gives the intercept of the asymptotic wave function with the r-axis.

The differential cross section $\mathrm{d}\sigma/\mathrm{d}\Omega$ is defined as the ratio between the incident probability current through the infinitesimal area $\mathrm{d}\sigma$ and the scattered probability current through the infinitesimal solid angle $\mathrm{d}\Omega$. From Eq. (2.15), it can be calculated that

$$\frac{\mathrm{d}\sigma}{\mathrm{d}\Omega} = |f(\theta)|^2. \tag{2.17}$$

The scattering amplitude and the total cross section can be determined by *the method of partial waves* as follows. For spherically symmetric potentials, the wave function for the relative motion can be expanded in terms of Legendre polynomials $P_l(\cos\theta)$,

$$\psi = \sum_{l=0}^{\infty} A_l P_l(\cos\theta) R_{kl}(r). \tag{2.18}$$

The radial wave functions $R_{kl}(r)$ satisfy the radial equation

$$\frac{\mathrm{d}^2 R_{kl}(r)}{\mathrm{d}r^2} + \frac{2}{r}\frac{\mathrm{d}R_{kl}(r)}{\mathrm{d}r} + \left[k^2 - \frac{l(l+1)}{r^2} - \frac{2m_\mathrm{r}}{\hbar^2}U(r)\right] R_{kl}(r) = 0, \tag{2.19}$$

where $U(r)$ is the potential and the energy of the state $E = \hbar^2 k^2 / 2m_\mathrm{r}$ with reduced mass m_r has been inserted. From Eq. (2.19), the radial wave function for $r \rightarrow \infty$ can determined to,

$$R_{kl}(r) \rightarrow \frac{1}{kr}\sin\left(kr - \frac{l\pi}{2} + \delta_l\right), \tag{2.20}$$

where δ_l is the l-wave phase shift describing the effect of the interaction on the l'th partial wave. By considering Eq. (2.15) in the limit of large r, expanding the incoming plane wave in Legendre polynomials and inserting Eq. (2.20), the scattering amplitude can be found to,

$$f(\theta) = \frac{1}{2ik}\sum_{l=0}^{\infty}(2l+1)(e^{i2\delta_l} - 1)P_l(\cos\theta). \tag{2.21}$$

The total cross section can then be obtained by integrating the differential cross section over all solid angles:

$$\sigma = \frac{4\pi}{k^2}\sum_{l=0}^{\infty}(2l+1)\sin^2\delta_l. \tag{2.22}$$

The scattering length can be determined from the requirement, that the asymptote of the radial wave function in Eq. (2.20) vanishes at $r = a$. For ultracold gases, the dominant contribution comes from s-wave scattering with $l = 0$, which results in the s-wave scattering length

$$a = -\lim_{k\to 0} \frac{1}{k} \tan \delta_0(k). \tag{2.23}$$

Evaluating Eq. (2.22) for $l = 0$ then yields

$$\sigma = \frac{4\pi}{k^2} \sin^2 \delta_0 = 4\pi a^2, \tag{2.24}$$

when inserting Eq. (2.23) and the total cross section is thus determined solely by the scattering length. For identical bosons, one must also take into account that the wave function must be symmetric under particle exchange. The resulting cross section for s-wave scattering then becomes $\sigma = 8\pi a^2$. For identical fermions, σ vanishes for $l = 0$. The simple dependence of the interparticle interactions contained in Eq. (2.24) turns out to have significant consequence as will be shown in the next section.

2.2.1 Feshbach Resonances

The scattering length a determines the scattering cross section and thus the strength of the interaction as explained in Sec. 2.2. In Sec. 2.3 it will be shown how the value of a has a significant impact on the theory of the condensed state, and the ability to tune its sign and magnitude therefore enables a multitude of research directions.

In this section, the phenomenon of magnetic Feshbach resonances is considered, which allows a to be tuned from $-\infty$ to ∞ by simply controlling the external magnetic field. To understand the occurrence of Feshbach resonances, the scattering theory must be extended to the multi channel case, where the term channel describes the set of quantum numbers characterizing the atoms taking part in a scattering process.

It turns out that the scattering properties in one channel can be drastically altered by the presence of a bound state in a different channel. This resonance phenomenon was investigated independently in the context of nuclear reactions [80] and to describe the asymmetric line shape resulting from inelastic scattering of electrons on helium [81]. Since its first observation in ultracold gases [82], the utilization of Feshbach resonances has become an invaluable

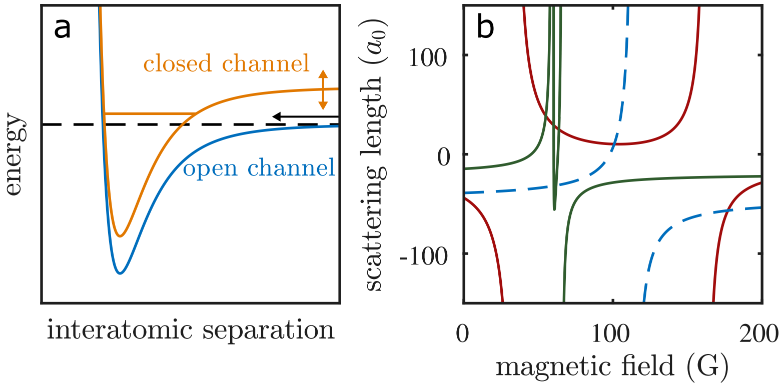

FIGURE 2.1: (a) Schematic representation of a the occurance of a Feshbach resonance. A pair of atoms with energy given by the black arrow scatter in the open channel (blue). The presence of a bound state in the closed channel (orange) leads to strong mixing between the two channels, as the particles in the open channel can scatter via an intermediate state in the closed channel. The vertical arrow indicates how the energy of the bound state can be tuned via the magnetic field. (b) Feshbach resonance structure for selected states of ^{39}K. The red curve corresponds to scattering between $|F = 1, m_F = -1\rangle$ atoms [83, 84], the green curve to $|F = 1, m_F = 0\rangle$ atoms [85], and the dashed blue curve to interstate scattering [48, 86]. Panel (a) is adopted from Ref. [87].

tool in the cold atom community, and in this section, the basic properties of Feshbach resonances are described based on the review by Chin *et al.* [27].

Figure 2.1(a) shows a schematic representation of how a Feshbach resonance occurs based on the two channels featuring the molecular potentials given in blue and orange. For large interatomic separations, the *open* channel (blue) connects to two free atoms. The low-energy collision processes in an ultracold gas happens with energy just above the scattering threshold of this channel. For a Feshbach resonance to occur, the energetically *closed* channel (orange) must support a bound state near the threshold of the open channel. If the energy of the bound state is close to the scattering state in the open channel, strong mixing between the two channels can occur. This process can be interpreted as two particles in the open channel scattering via an intermediate state in the closed channel, before quickly decaying back into the open channel.

If the magnetic moments of the states in the open and closed channels are different, the position of the bound state can be tuned relative to the threshold of the open channel. As a consequence, the scattering length depends on the magnetic field B and the scattering length takes the form

$$a(B) = a_{\mathrm{bg}} \left(1 - \frac{\Delta}{B - B_0}\right), \tag{2.25}$$

where a_{bg} is the background scattering length reflecting the off-resonant value, B_0 denotes the resonance position and Δ the width of the resonance [27]. For $B = B_0$, the scattering length diverges, and this regime is referred to as the unitary regime. The origin of this term comes from the $\sin^2 \delta_0$ factor of the cross section in Eq. (2.24) which becomes unity at the resonance position. In this regime, the relevant parameter of the interparticle interactions is no longer the scattering length, but the thermal de Broglie wavelength for thermal atoms, and the interparticle spacing for a BEC.

The implications of Feshbach resonances on the field of ultracold atomic gases cannot be understated. As an example, Fig. 2.1(b) shows the Feshbach resonance structure of the $|F = 1, m_F = -1\rangle$ and $|F = 1, m_F = 0\rangle$ states in ^{39}K investigated in this thesis. Importantly, the tunability of the scattering length allows Bose-Einstein condensation of ^{39}K despite its negative background scattering length, which otherwise prevents condensation as considered in Sec. 2.3. Furthermore, the rich Feshbach resonance structure enables the different research directions presented in Chs. 5 to 7, which all rely on the ability to tune the relevant interactions strengths.

2.2.2 Inelastic Collisions

Until now only elastic collisions where the total kinetic energy is conserved have been considered. Collision processes may, however, also occur where the kinetic energy of one or more of the colliding particles increases enough for the particle to leave the trap. For two-body collisions, this may occur if there is an exit channel available with lower energy. In this case, the two particles may be lost in spin-exchange processes where the excess energy is converted to kinetic energy.

Another loss mechanism comes from collisions involving three particles. In this case, two of the colliding particles may form a diatomic molecule, where the binding energy of the molecule is converted to kinetic energy leading to loss of all three particles. The three-body loss coefficient, L_3, is given by [88]

$$L_3 = C\frac{3\hbar}{m}a^4, \tag{2.26}$$

where C is a system-dependent dimensionless factor. The resulting loss rate in the atom number N is can be determined by integrating the local three-body loss rate $L_3 n^3$ over the sample,

$$\frac{\dot{N}}{N} = -L_3\langle n^2\rangle, \tag{2.27}$$

where $\langle \dots \rangle$ denotes the average over the density distribution in the trap.

In many cases, the above loss mechanism limit the achievable densities and lifetimes of trapped ultracold gases. However, loss measurements also serve as a powerful probe enabling the characterization of Feshbach resonances [82], observation of Efimov states [89], and the loss of atoms can be used as a spectroscopic signal [48].

2.3 The Gross-Pitaevskii Equation

In this section, the theory of the condensed state is presented and used to derive the Gross-Pitaevskii equation, which governs the physics of a BEC when including interactions. The derivations are based on Refs. [12, 75, 90].

All particles in the BEC occupy the same single particle wave function $\phi(\mathbf{r}_i)$ with the usual normalization,

$$\int \mathrm{d}\mathbf{r}\ |\phi(\mathbf{r})|^2 = 1, \tag{2.28}$$

and the total wave function is thus a symmetrized product of N single-particle wave functions,

$$\Psi(\mathbf{r}_1, \mathbf{r}_2, \dots, \mathbf{r}_N) = \prod_{i=1}^{N} \phi(\mathbf{r}_i). \tag{2.29}$$

In general, two atoms in the condensate interact via the potential $V_{\text{int}}(\mathbf{r}_i - \mathbf{r}_j)$. The system consist of a dilute gas of atoms, and the interparticle separations are therefore large compared to the typical distances where two atoms interact. In terms of the density and scattering length, this corresponds to $na^3 \ll 1$ meaning that the number of atoms within a "scattering volume" is small. This enables replacing the interatomic by a contact potential

$$V_{\text{int}}(\mathbf{r}_i - \mathbf{r}_j) \rightarrow U_0 \delta(\mathbf{r}_i - \mathbf{r}_j), \tag{2.30}$$

where $\delta(\mathbf{r}_1 - \mathbf{r}_2)$ is the Dirac delta function, and U_0 is related to the scattering length by

$$U_0 = \frac{4\pi\hbar^2 a}{m}. \tag{2.31}$$

The Hamiltonian for a gas of N interacting atoms is then given by

$$\hat{H} = \sum_{i=1}^{N} \left[-\frac{\hbar}{2m} \nabla_i^2 + V_{\text{trap}}(\mathbf{r}_i) \right] + U_0 \sum_{i<j} \delta(\mathbf{r}_i - \mathbf{r}_j), \tag{2.32}$$

where $V_{\text{trap}}(\mathbf{r})$ is the external trap potential. The energy of the N-particle state is given by the expectation value of the Hamiltonian in Eq. (2.32), $E = \langle \Psi | \hat{H} | \Psi \rangle$,

$$E = N \int d\mathbf{r} \left[-\phi^*(\mathbf{r}) \frac{\hbar^2}{2m} \nabla^2 \phi(\mathbf{r}) + V_{\text{trap}}(\mathbf{r}) |\phi(\mathbf{r})|^2 + \frac{N-1}{2} U_0 |\phi(\mathbf{r})|^4 \right]. \tag{2.33}$$

Introducing the condensate wave function $\psi(\mathbf{r}) = N^{1/2} \phi(\mathbf{r})$ with the normalization condition

$$\int d\mathbf{r}\, |\psi(\mathbf{r})|^2 = N \tag{2.34}$$

makes the density $n(\mathbf{r}) = |\psi(\mathbf{r})|^2$. Ignoring terms of order $1/N$, the energy then becomes

$$E = \int d\mathbf{r} \left[-\psi^*(\mathbf{r}) \frac{\hbar^2}{2m} \nabla^2 \psi(\mathbf{r}) + V_{\text{trap}} |\psi(\mathbf{r})|^2 + \frac{1}{2} U_0 |\psi(\mathbf{r})|^4 \right]. \tag{2.35}$$

From here, Eq. (2.35) is minimized under the constraint that the total number of particles (Eq. (2.34)) is constant. This is done by minimizing $E - \mu N$, with the chemical potential entering as a Lagrange multiplier. The resulting equation is then the time-independent Gross-Pitaevskii (GP) equation,

$$-\frac{\hbar^2}{2m}\nabla^2\psi(\mathbf{r}) + V_{\text{trap}}(\mathbf{r})\psi(\mathbf{r}) + U_0|\psi(\mathbf{r})|^2\psi(\mathbf{r}) = \mu\psi(\mathbf{r}). \tag{2.36}$$

Equation (2.36) has the form of a Schrödinger equation with the chemical potential as the eigenvalue and an additional non-linear term in the potential corresponding to the mean field produced by the other atoms in the condensate. The time-dependent generalization of Eq. (2.36) has the form,

$$i\hbar\frac{\partial\psi(\mathbf{r},t)}{\partial t} = -\frac{\hbar^2}{2m}\nabla^2\psi(\mathbf{r},t) + V_{\text{trap}}(\mathbf{r})\psi(\mathbf{r},t) + U_0|\psi(\mathbf{r},t)|^2\psi(\mathbf{r},t), \tag{2.37}$$

which is known as the time-dependent Gross-Pitaevskii equation. Solving Eqs. (2.36) and (2.37) thus allows determination of ground states and dynamics of the condensate wave function, and in Chs. 6 and 7, they will be used extensively to model the experiments.

2.3.1 Thomas-Fermi Limit

Despite the assumption that the atomic gas is dilute or weakly interacting in the sense $na^3 \ll 1$, interactions turn out to have a large effect on the condensate wave function. For a harmonically trapped BEC, the strength of the interactions relative to the kinetic energy is determined by the dimensionless quantity Na/a_{ho}, where $a_{\text{ho}} = \sqrt{\hbar/m\bar{\omega}}$ is the characteristic quantum mechanical length scale of the harmonic oscillator. This parameter is typically on the order of 10^3 to 10^4, resulting in interactions dominating the condensate wave function.

In the limit $Na/a_{\text{ho}} \gg 1$, the kinetic energy term in Eq. (2.36) can be neglected such that

$$\left(V_{\text{trap}}(\mathbf{r}) + U_0|\psi(\mathbf{r})|^2\right)\psi(\mathbf{r}) = \mu\psi(\mathbf{r}), \tag{2.38}$$

which is known as the Thomas-Fermi approximation. Solving for the density then yields

$$n(\mathbf{r}) = |\psi(\mathbf{r})|^2 = \frac{\mu - V_{\text{trap}}(\mathbf{r})}{U_0} \tag{2.39}$$

for $\mu > V_{\text{trap}}(\mathbf{r})$ and $n(\mathbf{r}) = 0$ outside. The density distribution thus has the form of an inverted parabola which vanishes at the Thomas-Fermi radius R_{TF} defined by $\mu = V_{\text{trap}}(R_{\text{TF}})$. For a harmonic trapping potential

$$R_{\text{TF}} = a_{\text{ho}} \left(\frac{15Na}{a_{\text{ho}}} \right)^{1/5}, \tag{2.40}$$

and the radius of the condensate is thus typically wider than a_{ho} as a consequence of the interaction term in Eq. (2.36). The condition for the boundary of the cloud $\mu = V_{\text{trap}}(R_{\text{TF}})$ can be interpreted in the sense that the trap potential is "filled up" to the height of the chemical potential.

2.3.2 Collapse for Attractive Interactions

For negative scattering lengths $a < 0$, the energy of the gas given by Eq. (2.35) is lowered by increasing the density in the centre of the trap. This effect is counteracted by the zero-point kinetic energy of the condensate wave function, however, for sufficiently attractive interactions, the system collapses and, as a consequence of the increased density, atoms are lost due to three-body recombination. The resulting *Bose nova* has been observed experimentally by preparing a BEC at repulsive interactions before employing a Feshbach resonance to make $a < 0$ [91–95]. For a spherically symmetric trap, the critical atom number for stability can be calculated to [96]

$$\frac{N_{\text{cr}}\, a}{a_{\text{ho}}} = -0.575, \tag{2.41}$$

and the experimentally measured atom number after collapse approximately matches this value [92].

2.3.3 Inelastic losses

Three-body losses can readily be included within the framework of the time-dependent GP equation, by assuming that the lost atoms leave the cloud without interacting with the remaining atoms. This is done by adding imaginary loss terms of the form $-i\hbar(K_3/2)|\psi|^4\psi$ to the right hand side of Eq. (2.37) [97]. This leads to a decay in the modulus square of the wave function proportional to the cube of the density,

$$\frac{\partial}{\partial t}\int_{\mathcal{V}} \mathrm{d}\mathbf{r}\,|\psi|^2 = -K_3\int_{\mathcal{V}} \mathrm{d}\mathbf{r}\,|\psi|^6, \tag{2.42}$$

where due to the indistinguishability of bosonic atoms [98, 99] the three-body loss coefficient K_3 is reduced by a factor $1/3!$ compared to the loss coefficient for thermal atoms.

2.3.4 Mixtures

In the case where two species of atoms are simultaneously condensed, the GP equation must be extended to account for both intra- and interspecies interactions. By denoting the two species by subscripts $i, j = 1, 2$, the two-component GP equations can be written as

$$-\frac{\hbar^2}{2m_1}\nabla^2\psi_1 + V_{\mathrm{trap},\,1}(\mathbf{r})\psi_1 + g_{11}|\psi_1|^2\psi_1 + g_{12}|\psi_2|^2\psi_1 = \mu_1\psi_1, \tag{2.43}$$

and

$$-\frac{\hbar^2}{2m_2}\nabla^2\psi_2 + V_{\mathrm{trap},\,2}(\mathbf{r})\psi_2 + g_{22}|\psi_2|^2\psi_2 + g_{12}|\psi_1|^2\psi_2 = \mu_2\psi_2, \tag{2.44}$$

where the constants g_{ij} are related to the intra- and interspecies scattering lengths a_{ij} by $g_{ij} = 2\pi\hbar^2 a_{ij}/m_{ij}$ with reduced mass $m_{ij} = m_i m_j/(m_i + m_j)$. Equation Eqs. (2.43) and (2.44), can be applied both in the case of different atomic species such as the ^{39}K–^{87}Rb mixtures previously investigated using the experimental apparatus [100] and for mixtures of spin states, which is the focus of Ch. 6. By considering the energy functional leading to Eqs. (2.43) and (2.44), the following stability conditions can be derived,

$$g_{11} > 0, \quad g_{22} > 0, \quad \text{and} \quad g_{11}g_{22} > g_{12}^2. \tag{2.45}$$

At the mean-field level, stability thus requires that the intraspecies interaction strengths must each be repulsive, and if the interspecies interactions are attractive, they must be overcome by the combined intraspecies repulsion. The last requirement can be rewritten in the terms of the scattering lengths by introducing

$$\delta a = a_{12} + \sqrt{a_{11}a_{22}}, \tag{2.46}$$

which is used extensively to characterize the system in Ch. 6.

2.3.5 Numerical Simulations of the Gross-Pitaevskii Equation

Many interesting problems can be analysed by solving the GP equation such as the calculation of ground states for different trap potentials and interaction strengths, and the dynamical behaviour of the condensate wave function.

In Chs. 6 and 7 the numerical toolbox GPELab [101, 102] is used extensively in order to solve the extended GP equations describing the physical systems. To compute the ground state of Eq. (2.36), GPELab uses the *projected gradient method* [103], which is commonly referred to as the *imaginary time method* [104] in the physics community.

The basic principle consists of the expanding the wave function in energy eigenstates $\Psi = \sum_n c_n e^{-iE_n t/\hbar}\psi_n$, and making the substitution $t = -i\tau$. By letting the time evolution happen in imaginary time τ, states of higher energy E_n will decay faster. If one then renormalizes Ψ after each numerical iteration, the wave function converges towards the ground state with lowest energy.

GPELab includes several methods for performing the time evolution. Within this work, the Backward Euler pseudoSPectral (BESP) scheme is used for the ground state calculations as generally recommended [101], and the Time-Splitting pseudoSPectral (TSSP) scheme is used for the dynamical calculations. Further detail on the methods employed by GPELab is out of the scope of the thesis, since it was only used as a tool for the numerical calculations.

2.4 The Bogoliubov Approximation

In this section the elementary excitations of a BEC are considered based on a microscopic theory for the Bose gas, which includes the quantum mechanical nature of the excitations. This leads to the famous Bogoliubov spectrum, and allows the calculation of the leading order corrections to the condensate density and ground state energy. The derivations in this section are based on Refs. [12, 75, 90].

The effective Hamiltonian in Eq. (2.32) describing N interacting bosons, can be written in second-quantized form as,

$$\hat{H} = \int d\mathbf{r}\Bigg[-\hat{\psi}^\dagger(\mathbf{r})\frac{\hbar^2}{2m}\nabla^2\hat{\psi}(\mathbf{r}) + V(\mathbf{r})\hat{\psi}^\dagger(\mathbf{r})\hat{\psi}(\mathbf{r}) + \frac{U_0}{2}\hat{\psi}^\dagger(\mathbf{r})\hat{\psi}^\dagger(\mathbf{r})\hat{\psi}(\mathbf{r})\hat{\psi}(\mathbf{r})\Bigg]. \tag{2.47}$$

In this notation, the bosonic field operator $\hat{\psi}^\dagger(\mathbf{r})$ creates a boson at $\mathbf{r}$, and $V(\mathbf{r})$ is the external potential. The field operator can be expanded in single-particle creation operators

$$\hat{\psi}(\mathbf{r}) = \sum_\nu \phi_\nu(\mathbf{r})\hat{a}_\nu, \tag{2.48}$$

where $\hat{a}_\nu^\dagger$ creates a particle in the single-particle state $|\phi_\nu\rangle$.

A BEC has a macroscopic population in the ground state, and it is therefore sensible to view the system as the condensed state plus a fluctuation term. This approach was first employed by N. Bogoliubov [105] and formally corresponds to writing the field operator as

$$\hat{\psi}(\mathbf{r}) = \sqrt{N_0}\phi_0(\mathbf{r}) + \sum_{\nu>0}\phi_\nu(\mathbf{r}) = \psi(\mathbf{r}) + \delta\hat{\psi}(\mathbf{r}), \tag{2.49}$$

where the single-particle operators for the ground state have been replaced by their eigenvalues $\hat{a}_0 \sim \hat{a}_0^\dagger \sim \sqrt{N_0}$, assuming that $N_0 \gg 1$. Note, that if the fluctuation term $\delta\hat{\psi}(\mathbf{r})$ is neglected, Eq. (2.47) reduces to Eq. (2.32), which is the Hamiltonian used to derive the GP equation.

2.4.1 Elementary Excitations

A uniform Bose gas consisting of N atoms confined within the volume $\mathcal{V}$ is now considered. Within the Bogoliubov approximation, Eq. (2.47) can be diagonalized by introducing the quasiparticle operators $\hat{\alpha}^{\dagger}_{\mathbf{p}}$ and $\hat{\alpha}_{\mathbf{p}}$, which create and destroy elementary excitations with momentum $\mathbf{p}$, respectively. The Hamiltonian thus becomes

$$\hat{H} = \frac{N^2 U_0}{2\mathcal{V}} + \sum_{\mathbf{p}\,(\mathbf{p}\neq 0)} \epsilon_p \hat{\alpha}^{\dagger}_{\mathbf{p}} \hat{\alpha}_{\mathbf{p}} - \frac{1}{2} \sum_{\mathbf{p}\,(\mathbf{p}\neq 0)} (\epsilon^0_p + n_0 U_0 - \epsilon_p), \tag{2.50}$$

and the resulting energy spectrum has the form

$$\epsilon_p = \sqrt{(\epsilon^0_p)^2 + 2\epsilon^0_p n_0 U_0}, \tag{2.51}$$

where $\epsilon^0_p = p^2/2m$. In the limit of small momenta, the spectrum has the linear dependence characteristic of sound waves $\epsilon_p \simeq sp$, where $s = \sqrt{n_0 U_0/m}$ is the speed of sound. Conversely, for large momenta $\epsilon_p \simeq n_0 U_0 + \epsilon^0_p$ corresponding to the energy spectrum of free particles shifted by the mean field.

In Fig. 2.2, the spectrum is shown together with the linear dispersion valid for $p\xi \ll 1$. Here, the healing length $\xi = \hbar/\sqrt{2mn_0 U_0}$ describes the length scale over which the condensate wave function varies when subjected to a localized perturbation. In these units, the Bogoliubov spectrum can readily be interpreted: For small energies corresponding to length scales longer than the healing length, the BEC has time to respond and the excitation can be regarded as a phonon. However, when $p \sim 1/\xi$, the BEC can no longer respond to the excitation, which can be regarded as a free particle.

2.4.2 Depletion of the Condensate

When including interactions in the description of the Bose gas, the condensate atom number is lowered and this is referred to as depletion of the condensate. The depletion can be determined by considering the operator for the total particle number given by

$$\hat{N} = \sum_{\mathbf{p}} \hat{a}^{\dagger}_{\mathbf{p}} \hat{a}_{\mathbf{p}} = N_0 + \sum_{\mathbf{p}\,(\mathbf{p}\neq 0)} \hat{a}^{\dagger}_{\mathbf{p}} \hat{a}_{\mathbf{p}}, \tag{2.52}$$

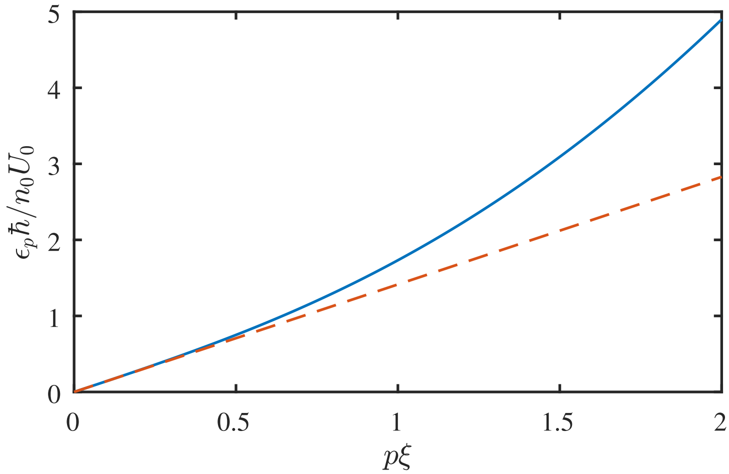

FIGURE 2.2: Bogoliubov spectrum for the energy of the elementary excitations. Eq. (2.51) is shown in blue and the linear dispersion valid for $p\xi \ll 1$ is shown in dashed orange.

where the replacement $\hat{a}_0 \sim \hat{a}_0^\dagger \sim \sqrt{N_0}$ for the ground state has been made.

The number of particles in excited states can be evaluated by expressing Eq. (2.52) in terms of the quasiparticle operators $\hat{\alpha}_{\mathbf{p}}$. Remarkably, it turns out that in the ground state with no elementary excitations present, there is still a fraction of atoms with momentum larger than zero, since the zero-point energy of the Bogoliubov modes causes fluctuations in the atom number. The relative size of the fluctuations to the total density can be calculated to

$$\frac{n_{\text{ex}}}{n_0} = \frac{8}{3\sqrt{\pi}}(n_0a^3)^{1/2}, \tag{2.53}$$

such that

$$n = n_0 + n_{\text{ex}} = n_0\left(1 + \frac{8}{3\sqrt{\pi}}(n_0a^3)^{1/2}\right). \tag{2.54}$$

Since $na^3 \ll 1$ for most experimental cases, the quantum depletion is typically on the order of one percent. However, by tuning the scattering length using Feshbach resonances, the depletion can be enhanced and in 2017 Eq. (2.53) was directly measured using a ^{39}K BEC confined in an optical box potential [106].

2.4.3 The Lee-Huang-Yang Correction to the Ground State Energy

When calculating the ground state energy using Eq. (2.50), one has to include the energy contribution from fluctuations in addition to the contribution from the condensed state. To do this consistently, the simple approximation of U_0 for the effective interaction cannot be used, since it is only valid for small momenta and the sum in Eq. (2.50) diverges linearly when $p \to \infty$. In order to make a consistent calculation, one must use an effective interaction which is cut off at momentum p_c. For small p_c and $E = 0$, the effective interaction is given by

$$U(p_\mathrm{c}) = U_0 + \frac{U_0^2}{\mathcal{V}} \sum_{\mathbf{p}\,(p<p_\mathrm{c})} \frac{1}{2\epsilon_p^0}, \tag{2.55}$$

and evaluating the ground state energy omitting momenta in excess of the cut-off then yields

$$E_0 = \frac{N^2 U_0}{2\mathcal{V}} - \frac{1}{2} \sum_{\mathbf{p}\,(p<p_\mathrm{c})} \left[\epsilon_p^0 + n_0 U_0 - \epsilon_p - \frac{(nU_0)^2}{2\epsilon_p^0} \right]. \tag{2.56}$$

If one now choses the cut-off momentum such that $ms \ll p_\mathrm{c} \ll \hbar/a$, the result becomes independent of p_c. Using that $n_0 \simeq n$, the ground state energy can be calculated to

$$\frac{E_0}{\mathcal{V}} = \frac{n^2 U_0}{2} \left[1 + \frac{128}{15\sqrt{\pi}} (na^3)^{1/2} \right]. \tag{2.57}$$

This calculation was first performed by Lee, Huang, and Yang in 1957 [55], and the second term in the square brackets is therefore known as the LHY correction. Since the LHY correction describes the energy contribution from quantum fluctuations, it has the same $\sqrt{na^3}$ scaling as the depletion.

CHAPTER 3

Atom-Light Interactions

In order to realize a BEC in a dilute gas, the atomic sample must be confined and cooled below the critical temperature. In practice, this is done by manipulating the atomic sample using electromagnetic fields in the form of static fields and radiation. In this chapter, the interaction of atoms with coherent electromagnetic radiation is presented, since it forms the basis for many of the steps in BEC production and allows the manipulation of the internal state of the atoms, which is used in the experiments of Chs. 5 and 6. The atomic interaction with static magnetic fields is discussed in Ch. 4.

The chapter is structured in the following way. In Sec. 3.1, the atomic interaction with coherent light is presented within the dipole approximation. The concepts of Rabi oscillations and adiabatic passages, which are used to manipulate the internal state of atoms are then derived in Sec. 3.2 and Sec. 3.3. Following this, the Bloch vector, which gives a useful representation of the atomic state is presented in Sec. 3.4, and subsequently, it is used to explain Ramsey interferometry in Sec. 3.5. The mechanical forces on atoms resulting from the interaction with electromagnetic radiation are then discussed, with Sec. 3.6 presenting the radiation-pressure force, which enables laser cooling. Finally, the dispersive dipole force leading to optical trapping is presented in Sec. 3.7. The derivations in this chapter are primarily based on the notes by D. A. Steck [107].

3.1 Two-Level Atom Interacting with Coherent Light

For the purposes considered within this work, a semi-classical description of the atom-light interaction is sufficient. In this case, the atom is treated as a two-level system that interacts with a classical electromagnetic field, which is assumed to be monochromatic with angular frequency ω corresponding to the output of a laser.

The electric field is thus given by $\mathbf{E}(t) = \hat{\mathbf{e}} E_0 \cos(\omega t)$, where $\hat{\mathbf{e}}$ is the unit polarization vector of the field and E_0 is its amplitude. The spatial dependence of the field has been neglected, which corresponds to making the dipole approximation, where the wavelength of the field is assumed to be much larger than the extent of the atom.

The atom is approximated as a two-level system with ground state $|\mathrm{g}\rangle$ and excited state $|\mathrm{e}\rangle$. The two states are separated by the energy splitting $\hbar\omega_0$, where ω_0 is the resonant transition frequency, and the difference between the laser frequency and the atomic resonance is given by the detuning $\Delta = \omega - \omega_0$.

The total Hamiltonian of the atom and field is the sum of the free atomic Hamiltonian and the interaction Hamiltonian

$$H = H_\mathrm{A} + H_\mathrm{I}, \tag{3.1}$$

where $H_\mathrm{A} = \hbar\omega_0 |\mathrm{e}\rangle\langle\mathrm{e}|$ is the atomic Hamiltonian with the ground-state energy is set to zero. The interaction Hamiltonian in the dipole approximation is given by

$$H_\mathrm{I} = -\mathbf{d} \cdot \mathbf{E}, \tag{3.2}$$

where $\mathbf{d}$ is the atomic dipole operator in terms of the electron position $\mathbf{r}_\mathrm{e}$ and the elementary charge e

$$\mathbf{d} = -e\mathbf{r}_\mathrm{e}. \tag{3.3}$$

In terms of the atomic lowering operator $\sigma = |\mathrm{g}\rangle\langle\mathrm{e}|$, $\mathbf{d}$ can be written as

$$\mathbf{d} = \langle\mathrm{g}|\mathbf{d}|\mathrm{e}\rangle(\sigma + \sigma^\dagger) \tag{3.4}$$

such that the interaction Hamiltonian becomes

$$H_{\mathrm{I}} = -\langle \mathrm{g}|\mathbf{d}|\mathrm{e}\rangle(\sigma + \sigma^{\dagger}) \cdot \mathbf{E}. \tag{3.5}$$

The electric field can be decomposed into positive- and negative-frequency components $\mathbf{E}(t) = \mathbf{E}_0^{(+)} e^{-i\omega t} + \mathbf{E}_0^{(-)} e^{i\omega t}$. Since the expectation value of σ has the time dependence $e^{-i\omega_0 t}$, Eq. (3.5) will result in terms oscillating as $e^{\pm i(\omega+\omega_0)t}$. In the rotating wave approximation, these rapidly oscillating terms are neglected since they average to zero. The interaction Hamiltonian can then be written as

$$H_{\mathrm{I}} = \frac{\hbar\Omega}{2}(\sigma e^{i\omega t} + \sigma^{\dagger} e^{-i\omega t}) \quad \text{(RWA)}, \tag{3.6}$$

where the Rabi frequency

$$\Omega = -\frac{\langle \mathrm{g}|\hat{\mathbf{e}} \cdot \mathbf{d}|\mathrm{e}\rangle E_0}{\hbar}, \tag{3.7}$$

characterizes the strength of the atom-field coupling, and $\langle \mathrm{g}|\hat{\mathbf{e}}\cdot\mathbf{d}|\mathrm{e}\rangle$ is referred to as the dipole matrix element.

3.2 Rabi Oscillations

The time-dependent populations of the ground and excited states can now be determined using the Schrödinger equation $i\hbar|\psi\rangle = H|\psi\rangle$ by writing the atomic state as

$$|\psi\rangle = c_{\mathrm{g}}\,|\mathrm{g}\rangle + c_{\mathrm{e}}\,|\mathrm{e}\rangle, \tag{3.8}$$

where c_{g} and c_{e} carry all the time dependence of the state. Projecting with $\langle \mathrm{g}|$ and $\langle \mathrm{e}|$, respectively, then yields the coupled differential equations

$$\begin{aligned} \dot{c}_{\mathrm{g}} &= -i\frac{\Omega}{2} c_{\mathrm{e}}\, e^{i\omega t} \\ \dot{c}_{\mathrm{e}} &= -i\omega_0 c_{\mathrm{e}} - i\frac{\Omega}{2} c_{\mathrm{g}}\, e^{-i\omega t}. \end{aligned} \tag{3.9}$$

Transforming into a frame rotating with the laser field, $\tilde{c}_{\mathrm{e}} = c_{\mathrm{e}}\, e^{i\omega t}$, then yields the equations of motion

$$\begin{aligned} \dot{c}_{\mathrm{g}} &= -i\frac{\Omega}{2}\tilde{c}_{\mathrm{e}} \\ \dot{\tilde{c}}_{\mathrm{e}} &= i\Delta\tilde{c}_{\mathrm{e}} - i\frac{\Omega}{2}c_{\mathrm{g}}\,, \end{aligned} \tag{3.10}$$

which can be solved to determine the populations $|c_{\mathrm{g}}|^2$ and $|\tilde{c}_{\mathrm{e}}|^2$ of the ground and excited states. For an atom that is initially in the ground state, $c_{\mathrm{g}}(0) = 1$ and $\tilde{c}_{\mathrm{e}}(0) = 0$, the populations can be calculated to

$$\begin{aligned} P_{\mathrm{g}}(t) &= |c_{\mathrm{g}}(t)|^2 = \frac{\Omega^2}{\tilde{\Omega}^2}\cos^2\left(\frac{1}{2}\tilde{\Omega}t\right), \\ P_{\mathrm{e}}(t) &= |\tilde{c}_{\mathrm{e}}(t)|^2 = \frac{\Omega^2}{\tilde{\Omega}^2}\sin^2\left(\frac{1}{2}\tilde{\Omega}t\right), \end{aligned} \tag{3.11}$$

where $\tilde{\Omega} = \sqrt{\Omega^2 + \Delta^2}$ is the generalized Rabi frequency. Equation 3.11 describes the phenomenon of Rabi flopping, where the population oscillates between the ground and excited state with frequency $\tilde{\Omega}$ when subject to near-resonant radiation. This is shown in Fig. 3.1(a) for different detunings Δ. When $\Delta = 0$ the period of the oscillation is $T = 2\pi/\Omega$, which leads to the following terms for an atom interacting with resonant light: A π-pulse corresponds to a pulse with duration such that $\Omega t = \pi$, which promotes an atom initially in the ground state to the excited state. Likewise a $\pi/2$-pulse transfers the population into a 50:50 superposition of the ground and excited state, and a 2π-pulse results in the system ending back in the ground state after the pulse. If the detuning is non-zero, the Rabi oscillations occur with larger frequency $\tilde{\Omega} > \Omega$ and with a smaller amplitude of $\Omega^2/\tilde{\Omega}^2$. In panel (b) of Fig. 3.1, the excited state population is shown as a function of the detuning for a fixed pulse duration. In terms of Δ, Eq. (3.11) takes the form of a sinc^2-function, which results in the side-lobes seen on the figure.

3.3 Adiabatic Passages

Manipulating the internal states of an atom by exposing it to radiation of a certain duration finds many applications within atomic and quantum physics,

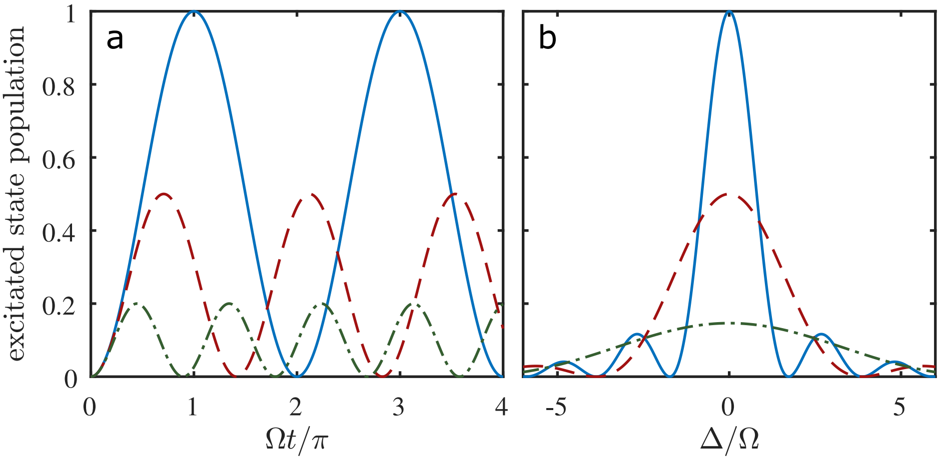

FIGURE 3.1: Excited state population for a two-level atom interacting with an electromagnetic field, where the atom starts in the ground state. (a) The population is shown as a function of time t for $\Delta = 0$ (solid blue), $\Delta = \Omega$ (dashed red), and $\Delta = 2\Omega$ (dash-dotted green). The population undergoes Rabi oscillations with frequency determined by $\tilde{\Omega}$. (b) Excited state population as a function of detuning for fixed interaction times $\Omega t = \pi$ (solid blue), $\Omega t = \pi/2$ (dashed red), and $\Omega t = \pi/4$ (dash-dotted green).

and is e.g. used extensively in interferometry experiments [108]. This method of state preparation is, however, sensitive to amplitude and frequency jitter of the radiation, and for long term stability, the method of rapid adiabatic passages is generally preferred, since it is less sensitive to these instabilities [109].

A rapid adiabatic passage can be understood by considering the atom-light coupling in the dressed state picture and determining the new eigenstates of the Hamiltonian Eq. (3.1) as follows. The equations of motion for the ground and excited state coefficients (Eq. (3.10)) can be written in matrix form

$$\begin{bmatrix} \dot{\tilde{c}}_{\mathrm{e}} \\ \dot{c}_{\mathrm{g}} \end{bmatrix} = -i \begin{bmatrix} -\Delta & \Omega/2 \\ \Omega/2 & 0 \end{bmatrix} \begin{bmatrix} \tilde{c}_{\mathrm{e}} \\ c_{\mathrm{g}} \end{bmatrix} = -\frac{i}{\hbar}\tilde{H} \begin{bmatrix} \tilde{c}_{\mathrm{e}} \\ c_{\mathrm{g}} \end{bmatrix}. \tag{3.12}$$

Diagonalizing the Hamiltonian then yields the energy eigenvalues

$$E_{\pm} = -\frac{\hbar\Delta}{2} \pm \frac{\hbar\tilde{\Omega}}{2}, \tag{3.13}$$

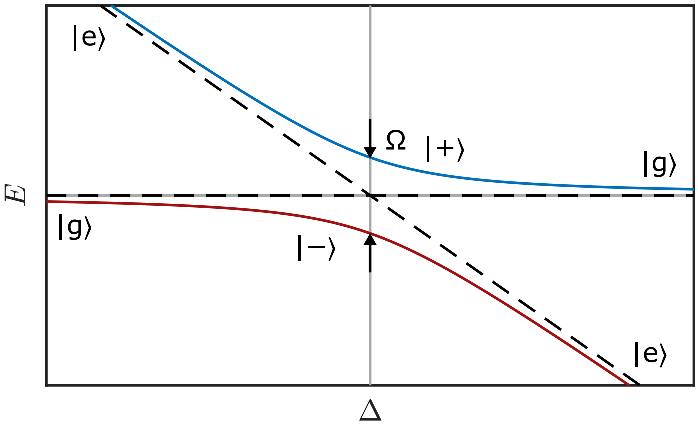

Figure 3.2: Energies of the bare and dressed states of a two-level system coupled to an electromagnetic field. The bare states are shown in dashed black, and the dressed states $|\pm\rangle$ are shown in blue and red, respectively. The coupling lifts the degeneracy at $\Delta = 0$ and causes an energy splitting of Ω.

which has eigenvectors $|\pm\rangle$ corresponding to the dressed states.

In Fig. 3.2, a schematic representation of the relevant energies are shown together with the bare states energies 0 and $-\hbar\Delta$ for the ground and excited states, respectively. The coupling to the electromagnetic field causes an avoided crossing with a splitting given by the coupling strength Ω. An adiabatic passage from the ground to excited state now corresponds to sweeping the frequency of the field sufficiently slowly across the resonance, such that the state is able to follow the $|-\rangle$ state from the left where $|-\rangle \simeq |g\rangle$ to the right where $|-\rangle \simeq |e\rangle$. In a *rapid* adiabatic passage, the speed of the frequency sweep is chosen such that it is fast compared to the relaxation time of the system T_{dec} , but slow enough that the system can follow adiabatically. This criterion can be written as

$$\frac{\Omega}{T_{\text{dec}}} \ll \frac{\partial\omega}{\partial t} \ll \Omega^2, \tag{3.14}$$

where $\omega/2\pi$ is the frequency of the radiation.

3.4 The Bloch Vector and Bloch Sphere

The Bloch vector is a valuable tool when describing coherent interactions between a two-level atom and electromagnetic radiation, since it allows complex state evolutions to be visualized as a vector confined to a sphere of unit radius. Within this work, it is used to describe the interferometric sequence employed in the experiments of Ch. 5. The Bloch vector uses the expectation values of the Pauli operators $\langle \sigma_i \rangle$ as the dynamical coordinates for the atomic evolution. These are given by

$$\begin{aligned} \sigma_x &= \begin{bmatrix} 0 & 1 \\ 1 & 0 \end{bmatrix} = \sigma + \sigma^\dagger, \\ \sigma_y &= \begin{bmatrix} 0 & -i \\ i & 0 \end{bmatrix} = i(\sigma - \sigma^\dagger), \\ \sigma_z &= \begin{bmatrix} 1 & 0 \\ 0 & -1 \end{bmatrix} = |\mathrm{e}\rangle\langle \mathrm{e}| - |\mathrm{g}\rangle\langle \mathrm{g}| = \sigma^\dagger \sigma - \sigma\sigma^\dagger \end{aligned} \tag{3.15}$$

and operate on states with the ordering

$$|\tilde{\psi}\rangle = \begin{bmatrix} \tilde{c}_\mathrm{e} \\ c_\mathrm{g} \end{bmatrix}, \tag{3.16}$$

where $c_\mathrm{g} = \tilde{c}_\mathrm{g}$.

The expectation values of the Pauli operators are related to the density matrix of the state $\rho = |\psi\rangle\langle\psi|$, where $\rho_{\alpha\beta} = c_\alpha c_\beta^*$. For $|\tilde{\psi}\rangle$ they become

$$\begin{aligned} \langle \sigma_x \rangle &= \langle \sigma \rangle + \langle \sigma^\dagger \rangle = \tilde{\rho}_\mathrm{eg} + \tilde{\rho}_\mathrm{ge}, \\ \langle \sigma_y \rangle &= i\langle \sigma \rangle - i\langle \sigma^\dagger \rangle = i(\tilde{\rho}_\mathrm{eg} - \tilde{\rho}_\mathrm{ge}), \\ \langle \sigma_z \rangle &= \rho_\mathrm{ee} - \rho_\mathrm{gg}, \end{aligned} \tag{3.17}$$

where the tildes indicate that the coherences are in the rotating frame. Here $\rho_{\alpha\alpha}$ is the population of the state in component α, and the coherences $\rho_{\alpha\beta} = c_\alpha c_\beta^* e^{i(\phi_\alpha - \phi_\beta)}$ contain information about the relative phase between components α and β. The equations of motion for the density matrix elements can be determined from Eq. (3.10) and from these, the time evolution of the Bloch variables in Eq. (3.17) can be determined to

$$\begin{aligned}\langle\dot{\sigma}_x\rangle &= \Delta\langle\sigma_y\rangle\\ \langle\dot{\sigma}_y\rangle &= -\Delta\langle\sigma_x\rangle - \Omega\langle\sigma_z\rangle\\ \langle\dot{\sigma}_z\rangle &= \Omega\langle\sigma_y\rangle.\end{aligned} \tag{3.18}$$

These equations can now be written in terms of the Bloch vector $\langle\boldsymbol{\sigma}\rangle = \langle\sigma_x\rangle\hat{\mathbf{x}} + \langle\sigma_y\rangle\hat{\mathbf{y}} + \langle\sigma_z\rangle\hat{\mathbf{z}}$ resulting in the torque equation

$$\langle\dot{\boldsymbol{\sigma}}\rangle = \wp \times \langle\boldsymbol{\sigma}\rangle, \tag{3.19}$$

where $\wp = \Omega\hat{\mathbf{x}} - \Delta\hat{\mathbf{z}}$ is the precession vector. From the definition of the cross product, the torque vector $\langle\dot{\boldsymbol{\sigma}}\rangle$ is perpendicular to $\langle\boldsymbol{\sigma}\rangle$ and the change in the Bloch vector is therefore always normal to itself making its lengths a constant of motion[1].

As seen from Eq. (3.17), the z-component of the Bloch vector describes the populations in the two states, where the ground and excited states correspond to the south and north poles of the Bloch sphere, respectively. The x- and y-components contain the coherences $\tilde{\rho}_{\text{eg}}$ and $\tilde{\rho}_{\text{ge}}$ and the azimuthal angle between them represents the relative phase of the ground and excited states.

The evolution of the Bloch vector is shown for different circumstances in Fig. 3.3. Panel (a) shows the effect of a resonant pulse where $\Delta = 0$. In this case, the Bloch vector rotates around $\hat{\mathbf{x}}$ with a rotation frequency set by Ω and traces out the blue circle on the sphere. A π-pulse thus corresponds to a rotation from the south pole to north pole, and a $\pi/2$-pulse causes the Bloch vector to end up at the equator. In panel (b) the light pulse is detuned with respect to the resonance frequency of the two-level system, which makes the Bloch vector rotate around an axis that is titled in the z-direction. Because of this, the trace of the Bloch vector never reaches the north pole corresponding to the detuned Rabi flops of Fig. 3.1(a). Panel (c) shows the effect of turning off the radiation. In this case, the Bloch vector precesses around $\hat{\mathbf{z}}$ with speed set by the detuning. Transforming back to the non-rotating frame

---

[1] This is only the case when excluding dephasing effects such as atomic collisions, which result in shrinking of the Bloch vector in the xy-plane. The effect of spontaneous emission is a rotation towards the south pole corresponding to the ground state.

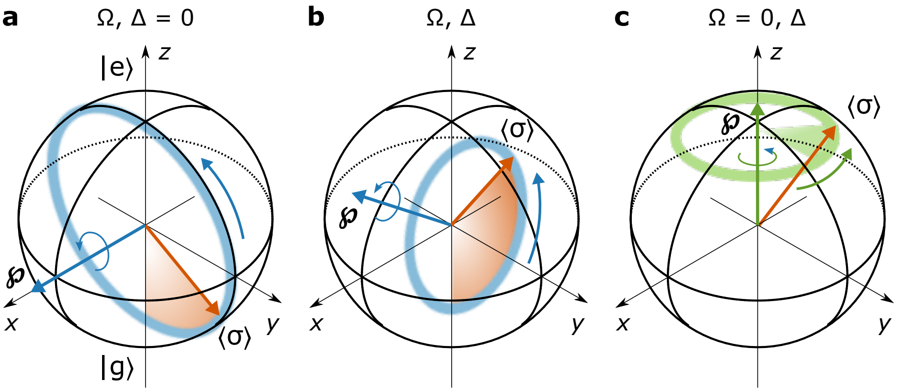

FIGURE 3.3: Evolution of the Bloch vector $\langle\boldsymbol{\sigma}\rangle$ on the Bloch sphere. (a) Effect of a resonant pulse. The Bloch vector (orange) rotates around $\wp$, which is aligned with $\hat{\mathbf{x}}$. (b) Effect of a detuned pulse. The Bloch vector rotates around an axis that is tilted in the z-direction and thus never reaches the north pole, resulting in imperfect transfer. (c) Evolution after turning off the pulses. The Bloch vector precesses around $\hat{\mathbf{z}}$ with speed set by the detuning.

corresponds to adding ω to the precession frequency, and the Bloch vector thus precesses with frequency set by $-\Delta + \omega = \omega_0$. The free evolution thus corresponds to the precession of the excited state phase relative to that of the ground state. In the case of adiabatic passages, the frequency sweep corresponds to continuously changing the direction of $\wp$, and thus the axis about which the Bloch vector rotates [110].

3.5 Ramsey Interferometry

The Bloch sphere picture is a convenient frame in which to describe the concept of Ramsey interferometry [111, 112], which is widely used in the context of atomic clocks [108, 113] and in the experiments of Ch. 5.

A Ramsey sequence consists of three steps. The sequence is initialized by a $\pi/2$-pulse which for $\Delta = 0$ prepares the system in an equal superposition state of $|g\rangle$ and $|e\rangle$. Following this, the system is allowed to evolve for a time T, during which the relative phase between the states causes the Bloch

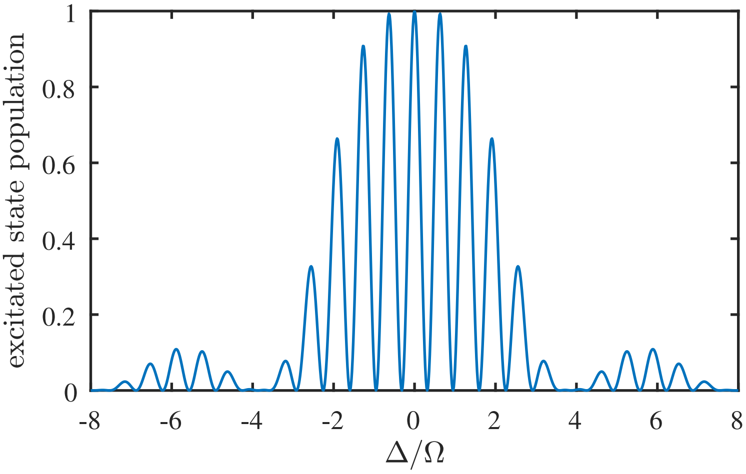

Figure 3.4: Excited state population after a Ramsey interferometry scheme as a function of the detuning Δ. The scheme consists of two $\pi/2$ pulses separated by an evolution time T and results in so-called Ramsey fringes. The width of the central fringe is given by $1/2T$.

vector to precess around the z-axis. Finally, a second $\pi/2$-pulse causes another rotation of the Bloch vector, and its final position is determined by the accumulated phase $\varphi_{\mathrm{C}} = -\Delta \cdot T$ between the pulses. If $\Delta \cdot T$ is an integer multiple of 2π, the second pulse rotates the state in the same direction as the first pulse. Conversely, if $\Delta \cdot T$ is an integer multiple of π, the second pulse rotates the state back towards $|\mathrm{g}\rangle$. As a consequence, the excited state population is sinusoidal in Δ with a period $2\pi/T$, and an example of the resulting Ramsey fringes is shown in Fig. 3.4.

In the context of atomic clocks, the Ramsey scheme allows one to measure an atomic transition frequency very precisely by increasing the free evolution time T, as the width of the central fringe is given by $1/2T$.

In addition to making precise spectroscopic measurements, the Ramsey scheme can also be employed to track the phase evolution of the system by varying the phase of the second pulse φ and thereby the axis around which the state is rotated. This method is used in Ch. 5 to track the dynamical evolution from a population-imbalanced superposition state into polaron quasiparticles.

3.6 Optical Molasses

In addition to manipulating the internal state, the interaction with laser light also leads to mechanical forces on atoms, which can be used to cool and confine atomic gases. Laser cooling was separately proposed in the context of neutral atoms [114] and ions [115], and shortly after, the first experimental realization was demonstrated on Mg^+–ions in 1978 [116]. For neutral atoms, experimental breakthroughs came in the following decade with the realization of a three-dimensional optical molasses [117], the Zeeman slower [118], and the magneto-optical trap [119].

When an atoms absorbs a photon from a laser beam, the photon momentum $\hbar\mathbf{k}$ (wave vector $\mathbf{k}$) is transferred to the atom. As a consequence, the atom experiences an average force due to the radiation pressure of

$$\mathbf{F}_{\mathrm{rad}} = \hbar\mathbf{k}R_{\mathrm{sc}}\,, \tag{3.20}$$

where

$$R_{\mathrm{sc}} = \frac{(\Gamma/2)^3}{\Delta^2 + (\Gamma/2)^2}\frac{I}{I_{\mathrm{sat}}}, \tag{3.21}$$

is the scattering rate, $I_{\mathrm{sat}} = \hbar\omega_0\Gamma/2\sigma_0$ is the saturation intensity, σ_0 is the absorption cross section, and Γ is the linewidth of the transition.

The radiation-pressure force can be used to cool atoms by exposing them to two counter-propagating laser beams with frequency tuned below the atomic resonance. If an atom with velocity v moves against the propagation direction of a laser beam with detuning Δ, the frequency of the laser light will be Doppler-shifted resulting in an effective detuning $\Delta + kv$. As the light is shifted into resonance, the scattering rate increases, which leads to an average force opposite to the propagation direction of the beam. The average force has no contribution from re-emission of photons since the spontaneous emission is symmetric. Re-emission does however cause fluctuations of the force, which cause the *mean square* of the velocity to increase, which leads to heating [120].

Adding the contribution from the two beams yields the radiation-pressure force

$$F_{\mathrm{rad}} = \hbar k\left(\frac{\Gamma}{2}\right)^3\left(\frac{1}{(\Delta - kv)^2 + (\Gamma/2)^2} - \frac{1}{(\Delta + kv)^2 + (\Gamma/2)^2}\right)\frac{I}{I_{\mathrm{sat}}}, \tag{3.22}$$

and in the limit of small velocities, this can be expanded to lowest order in v yielding

$$F_{\mathrm{rad}} = \frac{\hbar k^2 \Gamma^3}{2} \frac{\Delta}{(\Delta^2 + (\Gamma/2)^2)^2} \frac{I}{I_{\mathrm{sat}}} v \tag{3.23}$$

which results in a frictional force for $\Delta < 0$ leading to the term *optical molasses* for the beam configuration.

In addition to the cooling resulting from the frictional force, the atom also experiences heating due to the random nature of the absorption and re-emission events. Each time an atoms absorbs and emits a photon, it experiences two momentum kicks of magnitude $\hbar k$, and the mean square of the atomic velocity thus increases by $2(\hbar k/m)^2$ due to recoil heating.

By balancing the contributions to the change in $\langle v^2 \rangle$ from the optical molasses and recoil heating, the equilibrium kinetic energy can be determined and converted to a temperature via

$$\frac{1}{2} m \langle v^2 \rangle = \frac{3}{2} k_{\mathrm{B}} T. \tag{3.24}$$

This finally yields the *Doppler temperature*

$$k_{\mathrm{B}} T_{\mathrm{D}} = \frac{\hbar \Gamma}{2}, \tag{3.25}$$

which is the lower limit for the achievable temperature in an optical molasses using an optimal detuning $\Delta = -\Gamma/2$. For the experimentally relevant atomic species ^{39}K and ^{87}Rb, the Doppler temperatures are 145 µK [121] and 146 µK [122], respectively.

The limit given by the Doppler temperature was originally thought to be the lowest achievable temperature using laser cooling, with early experiments seemingly in agreement [117, 123]. Soon after, however, temperatures below the Doppler limit were measured in laser cooling experiments [124, 125], which was attributed to polarization gradient cooling [126]. Such schemes are now deliberately employed to cool atomic samples below the Doppler-limit after an initial Doppler cooling stage.

3.7 The Dipole Force

When the electromagnetic radiation is far-detuned from the atomic transition, absorption of photons is unlikely and the main effect of the light field consists of inducing an electric dipole moment in the atom. This leads to a force resulting from the potential of the induced dipole in the average electric field of the light, which was first used to trap neutral atoms by Chu *et al.* [127]. Since then, optical trapping using the dipole force has become an essential tool in the field of ultracold quantum gases, since it enables the confinement of atoms in states that are untrappable using magnetic fields, and enables the magnetic field to be used as for other purposes such as tuning of the interaction strengths [27]. The content of this section is based on a combination of the the notes by Steck [107] and the review by Grimm *et al.* [26].

For a two-level system interacting with a classical radiation field, the dipole force arises directly from the dressed state picture with the energies given by Eq. (3.13). For a constant detuning Δ, the energies of the states $|\pm\rangle$ depend on the generalized Rabi frequency $\tilde{\Omega}$, which in turn scales with the amplitude of the electric field. As a consequence, the energy shifts of the states $|\pm\rangle$ depend on the intensity of the radiation, which is shown in Fig. 3.5 for a laser beam with a Gaussian intensity profile and $\Delta < 0$. The ground and excited states are shifted in opposite directions by the coupling to the light field, and as the energy shift is spatially dependent, it can be interpreted as the relevant potential for the motion of the atoms.

For a large red detuning $\Delta < 0$, $|\Delta| \gg |\Omega|$, the bare ground state is equal to $|-\rangle$ (see Fig. 3.2), and the energy of the ground state can therefore be calculated as

$$\begin{aligned} E_- &= -\frac{\hbar\Delta}{2} - \frac{\hbar\tilde{\Omega}}{2} = -\frac{\hbar\Delta}{2} - \frac{\hbar}{2}|\Delta|\sqrt{1 + \frac{|\Omega|^2}{\Delta^2}} \\ &\simeq -\frac{\hbar\Delta}{2} - \frac{\hbar|\Delta|}{2}\left(1 + \frac{|\Omega|^2}{2\Delta^2}\right) = \frac{\hbar|\Omega|^2}{4\Delta} = \frac{|\langle \mathrm{g}|\hat{\mathbf{e}} \cdot \mathbf{d}|\mathrm{e}\rangle|^2 |E_0|^2}{4\hbar\Delta}. \end{aligned} \tag{3.26}$$

The electric field amplitude can be written in terms of the field intensity $I = c\epsilon_0|E_0|^2/2$, where c is the speed of light in vacuum, and ϵ_0 is the vacuum permittivity. The dipole matrix element can be written in terms of

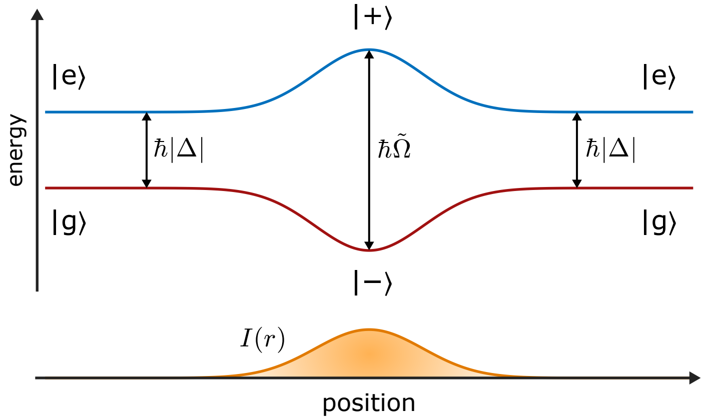

Figure 3.5: Schematic energy diagram for the dressed states $|\pm\rangle$. The energies are shown for a constant detuning $\Delta < 0$ and a Rabi frequency given by the light field with a Gaussian intensity distribution (orange). The energy shift serves as an effective potential for the atomic motion, and for $\Delta < 0$, atoms in the ground state are attracted towards the intensity maximum.

the natural linewidth of the transition $\Gamma = |\langle \mathrm{g}|\hat{\mathbf{e}}\cdot\mathbf{d}|\mathrm{e}\rangle|^2\omega_0^3/3\pi\epsilon_0\hbar c^3$, and the resulting dipole potential can then be determined to

$$U_{\mathrm{dip}}(\mathbf{r}) = \frac{3\pi c^2\Gamma}{2\omega_0^3}\frac{I(\mathbf{r})}{\Delta}. \tag{3.27}$$

Thus, the strength of the dipole force $\mathbf{F}_{\mathrm{dip}}(\mathbf{r}) = -\nabla U_{\mathrm{dip}}(\mathbf{r})$ can be controlled by the light intensity. Furthermore, the sign of the dipole potential is determined by the detuning, such that the potential is attractive for red-detuned light ($\Delta < 0$) and repulsive for blue-detuned light[2] ($\Delta > 0$).

These attributes of the dipole force enables the use of far-detuned laser beams to confine atoms spatially in many different configurations. The simplest relevant example is the potential resulting from a focused Gaussian beam with power P, which has the intensity profile

$$I(r,z) = \frac{2P}{\pi w^2(z)}\exp\left(-2\frac{r^2}{w^2(z)}\right). \tag{3.28}$$

---

[2] For $\Delta > 0$ the bare ground state $|\mathrm{g}\rangle$ equals the $|+\rangle$ state, and one must calculate E_+ to get the result of Eq. (3.27).

Here the $1/e^2$ radius of the beam is given by

$$w(z) = w_0 \sqrt{1 + \left(\frac{z}{z_\mathrm{R}} \right)^2} \tag{3.29}$$

with the Rayleigh length $z_\mathrm{R} = \pi w_0^2/\lambda$ and beam waist w_0. If the potential depth U_0 exceeds the thermal energy of the atomic ensemble, the potential can to a good approximation be considered as a cylindrically symmetric harmonic oscillator

$$U_{\text{dip, focused Gaussian}}(r, z) = -U_0 \left[1 - 2\left(\frac{r}{w_0} \right)^2 - \left(\frac{z}{z_\mathrm{R}} \right)^2 \right]. \tag{3.30}$$

For an atom with mass m, the oscillation frequencies (or trap frequencies) are then $\omega_r = \sqrt{4U_0/m\omega_0^2}$ and $\omega_z = \sqrt{2U_0/mz_\mathrm{R}^2}$ in the radial and axial directions, respectively. In the case of ultracold atoms, the external potential can thus be characterized by the trap frequencies, which can be determined experimentally as described in Sec. 4.4.

For multi-level atoms the dipole potential given in Eq. (3.27) is generally not sufficient, since the ground state energy shift has contributions from several excited states. One therefore has to sum up the energy shifts due to the coupling to all relevant excited states, which for alkali atoms corresponds to including both states of the D line doublet, which is described in Sec. 4.1. The energy shift of state i is thus given by

$$\Delta E_i = \sum_{j \neq i} \frac{|\langle j | H_\mathrm{I} | i \rangle|^2}{\mathcal{E}_i - \mathcal{E}_j}, \tag{3.31}$$

where H_I is the interaction Hamiltonian in the dipole approximation (Eq. (3.2)) and $\mathcal{E}_i$ is the unperturbed energy of state i. For a two-level atom, Eq. (3.31) reduces to Eq. (3.27) for the ground state.

For the alkali atoms considered in this thesis, summing over the D1 and D2 lines and using linearly polarized light results in the dipole potential

$$U = \frac{\pi c^2}{2} \left(\frac{\Gamma_\mathrm{D1}}{\omega_\mathrm{D1}^3 \Delta_\mathrm{D1}} + \frac{2\Gamma_\mathrm{D2}}{\omega_\mathrm{D2}^3 \Delta_\mathrm{D1}} \right) I(\mathbf{r}), \tag{3.32}$$

where ω_i is the angular frequency of transition i, Γ_i is its linewidth, and Δ_i is the detuning of the laser light from the transition.

CHAPTER 4

Production of ^{39}K Bose-Einstein Condensates

The experiments conducted within this thesis are all performed using BECs of ^{39}K, which has a rich Feshbach resonance structure that enables the interactions in the system to be tuned. All presented experiments start from a ^{39}K BEC confined in an optical dipole trap, and this chapter gives an overview of the experimental steps leading to this point. For more details on the specifics parts, the reader is referred to the theses of Nils Winter [128] and Lars J. Wacker [129] which provide a thorough description of the current edition of the apparatus.

The machine was originally constructed in Hannover, Germany [130, 131] before being moved to Aarhus in 2011. Experiments on the original ^{87}Rb apparatus lead to the realization of a gravity compensated atom laser [132], the extension of the coherence time of the ^{87}Rb clock transition by employing spin self-rephasing [133], and recently, data that was recorded just before moving the apparatus has been interpreted as a simulation of an XXZ spin model [134]. After the move to Aarhus, the machine was modified to produce ^{39}K–^{87}Rb and ^{41}K–^{87}Rb mixtures [100]. Since then, it has been used for experiments on few-body physics with both K–Rb mixtures [135] and ^{39}K [136], for the investigation of the phase separation and dynamics of two-component BECs [137], and for the observation of attractive and repulsive polarons in a ^{39}K BEC [48, 138]. Within my time in the research group, the apparatus has been used to investigate the dynamical formation of polarons in a BEC [51, 52] (Ch. 5) and to realize a Lee-Huang-Yang fluid [54] (Ch. 6), where for the latter, an additional laser beam along the vertical direction was added to the optical dipole trap. Most recently, progress has been made towards BEC production at high magnetic fields, which is described in Ch. 7.

The chapter is separated in four parts: First, the relevant properties of ^{39}K and ^{87}Rb that enable BEC production are presented in Sec. 4.1. Following this, an overview of the apparatus is given in Sec. 4.2, where the major steps in the experimental procedure are presented. A detailed description of the optical setup for the vertical trapping beam is then given in Sec. 4.3, and finally the resulting optical dipole trap is characterized in Sec. 4.4.

4.1 Properties of ^{87}Rb and ^{39}K

In order to produce a BEC, the atomic sample must be trapped and cooled below the critical temperature as described in Sec. 2.1. This is generally achieved by manipulating the atoms using electromagnetic radiation and magnetic fields. A detailed understanding of the internal energy structure of the atomics species is therefore required. In this thesis, the experiments are performed using BECs of ^{39}K, which are prepared by sympathetic cooling with ^{87}Rb. The most relevant properties of these species are given in the following section based on Refs. [121, 122], which contain comprehensive information on the different isotopes of Rb and K.

^{87}Rb and ^{39}K are both alkali atoms featuring a single valence electron, and therefore the energetic structure of the electronic states is reasonably simple. The ground states of ^{87}Rb and ^{39}K have primary quantum numbers $n = 5$ and $n = 4$, respectively, and orbital angular momentum quantum number $L = 0$ such that the corresponding term symbol $n^{2S+1}L_J$ for the states can be written $5^2\mathrm{S}_{1/2}$ and $4^2\mathrm{S}_{1/2}$, where S is the spin quantum number and $J = L + S$ is the total electronic angular momentum. The first excited state has orbital angular momentum $L = 1$ and the spin-orbit coupling therefore splits it into two fine structure states with $J = 1/2$ and $J = 3/2$. The transitions from the ground state to the these states are known as the D1 and D2 lines, respectively. Both atomic species have nuclear spins of

$I = 3/2$ making the total angular momentum $F = J + I$ an integer and both are therefore bosons. The coupling to the nuclear spin results in the hyperfine states with $F = 0, 1, \dots, J + I$. For most purposes in the apparatus, only the D2 line is relevant, and the corresponding states are therefore shown in Fig. 4.1, with the respective optical wavelengths in nm and the hyperfine splittings relative to the $n^2\mathrm{S}_{1/2}$ and $n^2\mathrm{P}_{3/2}$ states given in MHz. Throughout the thesis, the levels of the hyperfine ground state manifold are labelled by $|F\rangle$ and those of the $n^2\mathrm{P}_{3/2}$ excited state manifold are labelled by $|F'\rangle$. When the state ket contains two quantum numbers, they refer to the total angular momentum F and its projection m_F unless otherwise specified.

For the optical transitions considered here, the example most similar to a two-level atom are the *cycling transitions* $|2, \pm 2\rangle \rightarrow |3', \pm 3'\rangle$ of the D2 line of ^{87}Rb. These transitions are closed in the sense that the electric dipole selection rules only allow the excited states to decay to the given states with $F = 2$. As a consequence, these transitions are generally used for laser cooling and imaging of ^{87}Rb. For ^{39}K the situation is more complicated since the hyperfine levels of the excited state manifold feature small spacings of $\sim 10\,\mathrm{MHz}$, which is on the order of the natural linewidth of the D2 line $\Gamma/2\pi = 6.035(11)\,\mathrm{MHz}$ [121]. Trying to drive the $|2\rangle \rightarrow |3'\rangle$ transition of ^{39}K thus also populates the $|2'\rangle$ state, which generally makes ^{39}K less well-suited for laser cooling [139–143]. The apparatus presented here remedies this issue by performing much of the cooling of the ^{39}K sample sympathetically with ^{87}Rb.

4.1.1 Response to a Magnetic Field

When an atom interacts with an external magnetic field, the energies of its internal states are shifted according to their magnetic quantum numbers and the magnetic field strength. As a consequence, magnetic fields can be used to trap specific states, to adjust the resonant transition frequencies, and to tune the interaction strength via Feshbach resonances. In this section, the most important results for atoms interacting with magnetic fields are presented based on Refs. [107, 122].

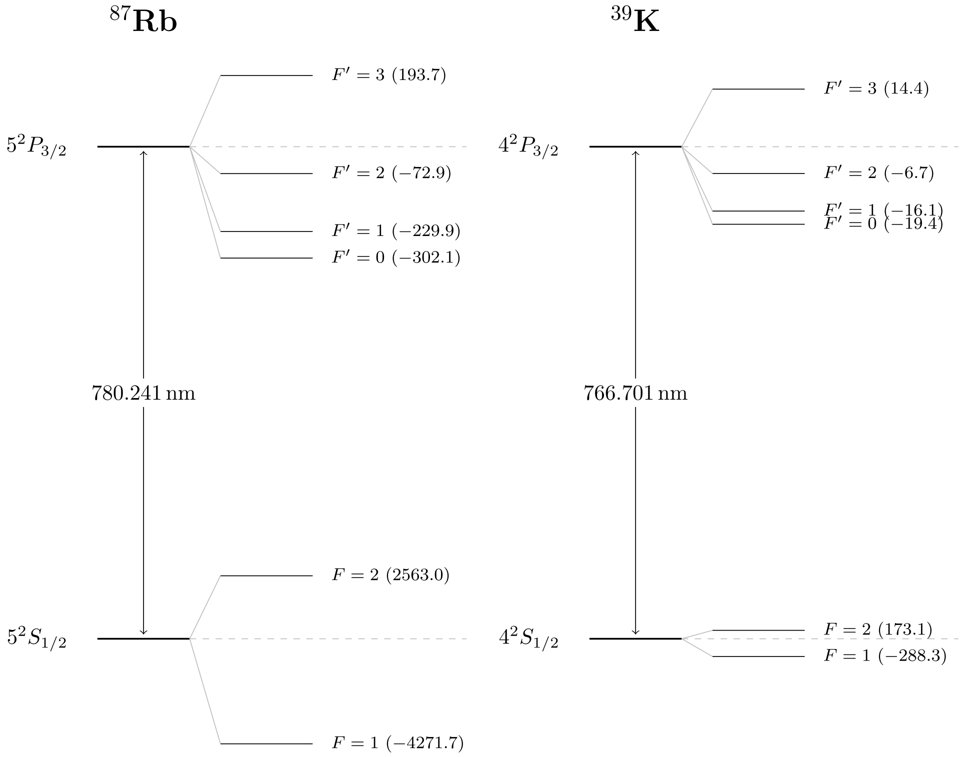

FIGURE 4.1: D2 lines of ^{87}Rb and ^{39}K. The figure is adopted from [128] with data from Refs. [121, 122]. The numbers in parentheses give the shifts in MHz from the unperturbed states.

The Hamiltonian describing the atomic interaction with a magnetic field is given by

$$\begin{aligned} H_B &= \frac{\mu_B}{\hbar}(g_s\mathbf{S} + g_L\mathbf{L} + g_I\mathbf{I}) \cdot \mathbf{B} \\ &= \frac{\mu_B}{\hbar}(g_S S_z + g_L L_z + g_I I_z)B_z, \end{aligned} \tag{4.1}$$

where μ_B is the Bohr magneton, and $\mathbf{B}$ is the magnetic field which is taken to be along the z-direction. $\mathbf{L}$ is the orbital angular momentum of the electron, $\mathbf{S}$ the electron spin, $\mathbf{I}$ the nuclear spin, while g_S, g_L, and g_I are respective g-factors. If the energy shift due to the magnetic field is small compared to the hyperfine splittings, F is a good quantum number and H_B can be seen as a small perturbation to the zero-field eigenstates of the hyperfine Hamiltonian H_{hfs}, $|F, m_F\rangle$. The energy shift to lowest order is then given by

$$\Delta E = m_F g_F \mu_B B_z \tag{4.2}$$

where g_F is the hyperfine Landé g-factor. This low-field dependence is known as the *Zeeman effect*. For the ground state hyperfine manifold, $g_F \simeq -1/2$ for $F = 1$ and $g_F \simeq 1/2$ for $F = 2$, and the magnetically trappable weak-field seeking states are thus $|F = 1, m_F = -1\rangle$ and $|F = 2, m_F = 1, 2\rangle$.

For strong magnetic fields where the energy shift due to the magnetic field is large compared to the hyperfine splitting, F is no longer a good quantum number. In this case, the hyperfine interaction can be seen as a perturbation to the strong-field eigenstates $|J, m_J; I, m_I\rangle$ and to lowest order, the energies can be calculated to

$$\begin{aligned} E_{|J,m_J,I;m_I\rangle} &= A_{\text{hfs}}\, m_I m_J \\ &+ B_{\text{hfs}} \frac{9(m_I m_J)^2 - 3J(J+1)m_I^2 - 3I(I+1)m_J^2 + I(I+1)J(J+1)}{4J(2J-1)I(2I-1)} \\ &+ \mu_B (g_J m_J + g_I m_I) B, \end{aligned} \tag{4.3}$$

where A_{hfs} and B_{hfs} are the magnetic-dipole and electric-quadrupole hyperfine constants. In this regime the coupling between $\mathbf{J}$ and $\mathbf{I}$ has been broken by the external magnetic field, and the resulting linear dependence on the magnetic field strength is known as the hyperfine *Paschen-Back effect*.

In the intermediate regime, the eigenstates are superpositions of the states $|F, m_F\rangle$ and $|J, m_J; I, m_I\rangle$ and one generally has to numerically diagonalize the Hamiltonian $H_{\text{hfs}} + H_B$ in order to find the energy shifts. For the special case of $J = 1/2$ corresponding to e.g. the ground states of ^{87}Rb and ^{39}K, the Hamiltonian can be diagonalized analytically resulting in the *Breit-Rabi formula* for the energies [144]

$$\begin{aligned} E_{F=I\pm 1/2,\, m_F} = &- \frac{\Delta E_{\text{hfs}}}{2(2I+1)} + g_I \mu_B m_F B \\ &\pm \frac{\Delta E_{\text{hfs}}}{2} \left(1 + \frac{4 m_F x}{2I+1} + x^2\right)^{1/2}, \end{aligned} \tag{4.4}$$

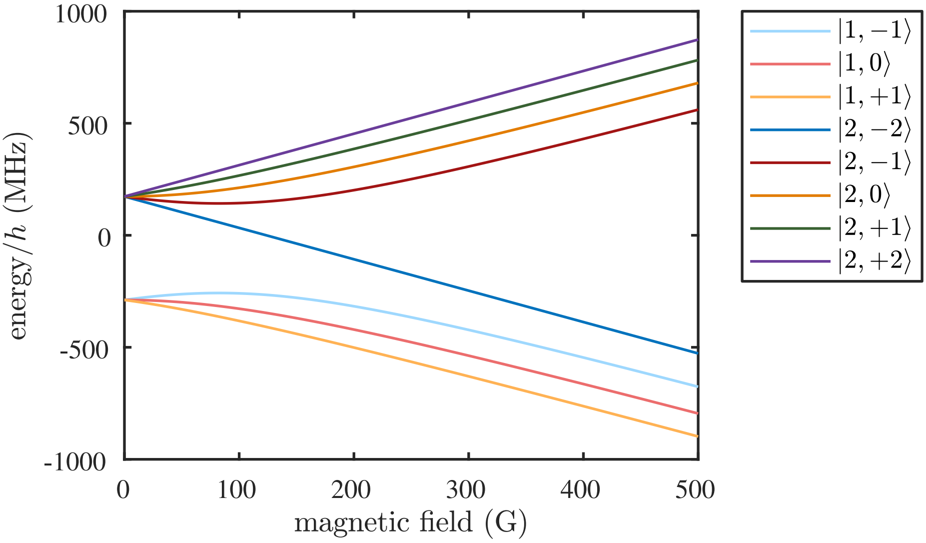

FIGURE 4.2: Energies of the states in the $4^2\mathrm{S}_{1/2}$ manifold of ^{39}K as a function of magnetic field calculated using the Breit-Rabi formula (Eq. (4.4)). Due to the small hyperfine splitting of ^{39}K, the energy levels quickly differ from the linear Zeeman shift given by Eq. (4.2). After the intermediate regime, the states again depend linearly on the magnetic field strength as given by the Paschen-Back effect (Eq. (4.3)). The states are labelled according to their low-field quantum numbers $|F, m_F\rangle$.

where

$$x = \frac{\mu_B(g_J - g_I)B}{\Delta E_{\mathrm{hfs}}}, \tag{4.5}$$

and ΔE_{hfs} is the hyperfine splitting. In Fig. 4.2 the energies of the states in the $4^2\mathrm{S}_{1/2}$ manifold of ^{39}K are shown as a function of magnetic field using the Breit-Rabi formula with the states labelled according to their low-field quantum numbers $|F, m_F\rangle$. The small hyperfine splitting of ^{39}K cause the system to enter the intermediate regime already at small magnetic fields, and for the $F = 1$ states, the linear Zeeman effect thus becomes invalid at $\sim 10\,\mathrm{G}$. For large magnetic fields, the energies once again become linear in the magnetic field as the system enters the Paschen-Back regime.

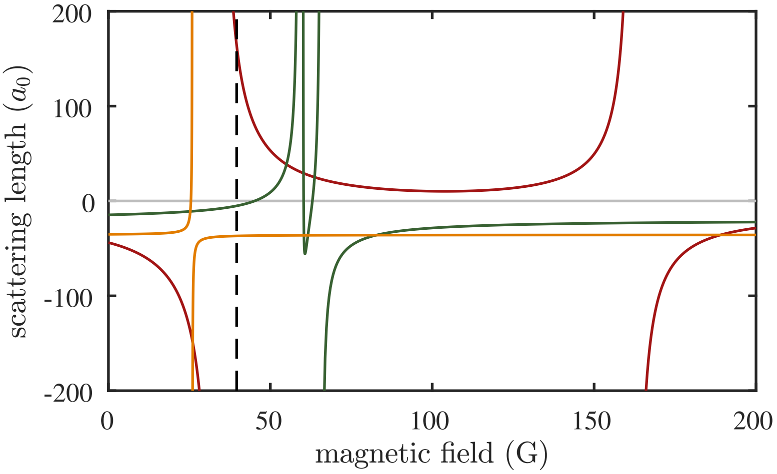

FIGURE 4.3: Feshbach resonance structure for the lowest hyperfine manifold of ^{39}K. The intrastate scattering length as a function of magnetic field is shown in red for atoms in the $|1,-1\rangle$ state [83, 84], in green for atoms in the $|1,0\rangle$ state [85], and in orange for atoms in the $|1,1\rangle$ state [83]. The magnetic field used for BEC production is marked by the dashed black line.

4.1.2 Feshbach Resonance Structure

In order to create a stable BEC, the scattering length must be positive, otherwise the system can collapse in a Bose nova as explained in Sec. 2.3.2. For ^{87}Rb this is not an issue since the species has a constant scattering length of $\sim 100\,a_0$ and only features narrow Feshbach resonances [145]. This, however, makes ^{87}Rb a relatively poor candidate for experiments with tunable interaction strengths. For ^{39}K, the situation is different as it has a negative background scattering length, and production of stable ^{39}K BECs thus *requires* tuning the scattering length via Feshbach resonances. Figure 4.3 shows the Feshbach resonance structure of the three states of the lowest hyperfine manifold of ^{39}K with the scattering lengths of the $|1,-1\rangle$, $|1,0\rangle$, and $|1,1\rangle$ states shown in red, green, and orange, respectively.

Fortunately, the $|1,-1\rangle$ state features two broad resonances at 33.6 and 163 G which produce a $\sim$ 130 G wide window where the scattering length is positive [83, 84, 146]. This enables BEC production, which is typically performed at a magnetic field of 39.6 G where the scattering length is $165\,a_0$

as shown by the dashed black line in Fig. 4.3. The interspecies scattering lengths between different combinations of states in ^{87}Rb and ^{39}K has been investigated in Refs. [147, 148], and the interspecies resonance at 117.56 G [100] was employed in a previous experiment using this apparatus [137]. For the experiments presented here, ^{87}Rb is only used to sympathetically cool the smaller ^{39}K sample, which takes place in the $|2,2\rangle$ state for both species. Here, the interspecies scattering length is $\sim 28\ a_0$ for the relevant magnetic fields [147].

4.2 Overview of the Apparatus

The experimental setup is composed of two optical tables; one for preparing the majority of laser beams used for manipulating the atoms, and one which contains the vacuum chamber. The two tables are referred to as the *laser table* and the *experiment table*, respectively. On the laser table, the light which is used to cool, manipulate, and image the atoms is prepared. In practice, this corresponds to locking the laser frequencies relative to Doppler-free absorption signals, controlling the frequencies using acousto-optical modulators, amplifying the laser powers using tampered amplifiers, and coupling the light into optical fibres, which deliver the light to the experiment table. Since the D2 lines of ^{87}Rb and ^{39}K feature transition wavelengths of 780 nm and 767 nm, the same optical components can be used for both species

The vacuum system on the experiment table is separated in two parts with each end connected to a glass cell allowing good optical access. On one side, the initial trapping and cooling takes place in a magneto-optical trap (MOT) and the glass cell is therefore referred to as the *MOT cell*. Evaporative cooling, Bose-Einstein condensation, and performing the experiments takes place in the second glass cell on the other side, which is referred to as the *science cell*. The two sides of the vacuum system are connected via a differential pumping stage, which enables lower pressures and thus longer lifetimes of the trapped samples in the science cell.

4.2.1 Magneto-Optical Trap

The starting point of the experimental procedure is a MOT, which was first realized for sodium atoms in 1987 [119]. In a MOT, an atomic vapour is simultaneously cooled and confined by the use of counter-propagating laser beams with a frequency that is red-detuned to an atomic transition, and a quadrupole magnetic field, which supplies a magnetic field gradient. The cooling and confinement are caused by the momentum kicks experienced by the atom when absorbing photons from the laser light. Here, the absorption rate depends on the atomic velocity due to the Doppler effect, which shifts the red-detuned light into resonance as described in Sec. 3.6, and on the position due to the magnetic field gradient, which shifts the energy levels via the Zeeman effect.

The employed dual-species MOT is constructed to simultaneously trap and cool both Rb and K. The atoms are loaded from a background vapour which is supplied by commercial dispensers. During the MOT phase, atoms stuck on the glass surfaces are detached by light-induced atom desorption using ultraviolet light emitting diodes [149], which significantly increases the number of captured atoms.

An overview of the MOT region of the apparatus is shown in Fig. 4.4. In order to trap and cool the atoms along all directions, the MOT is composed of six cooling beams intersecting in the centre of two coils in anti-Helmholtz configuration, which supply the quadrupole magnetic field. The cooling light is red-detuned in relation to the $|2\rangle \rightarrow |3'\rangle$ transition, however, since there is a finite probability of driving the $|2\rangle \rightarrow |2'\rangle$ transition, atoms will accumulate in the $|1\rangle$ state as atoms in the $|2'\rangle$ state can decay to both $|1\rangle$ and $|2\rangle$. Additional repumping light working on the $|1\rangle \rightarrow |2'\rangle$ transition is therefore needed to reintroduce the atoms into cooling cycle.

As explained in Sec. 4.1, the hyperfine splittings of ^{39}K are small, and the roles of the cooling and repumping light are therefore not clearly distinguished causing relatively few atoms to be captured in the MOT. Furthermore, dual-species MOTs suffer from losses due to light-assisted collisions, which is especially harmful to the already small ^{39}K samples [150]. To circumvent this issue, the ^{87}Rb MOT is operated in a dark-SPOT configuration, which has previously been used to increase the phase-space density of single-species MOTs [151–154] and to reduce light-assisted collisions in mixtures

[155, 156]. In this configuration, the ^{87}Rb atoms are deliberately made to accumulate in the dark $|1\rangle$ state in the centre of the trap. This is achieved by cutting out the central part of the ^{87}Rb repumping beam, and by supplying additional depumping light tuned to the $|2\rangle \rightarrow |2'\rangle$ transition. The result is an increase in the captured number of ^{39}K atoms by more than a factor 2 compared to loading with a bright ^{87}Rb MOT, and during the 25 second duration of the MOT phase $\sim 1 \times 10^8$ ^{39}K and $\sim 3 \times 10^9$ ^{87}Rb atoms are captured [100].

After the MOT phase, the magnetic field is turned off and the atoms are further cooled below the Doppler limit in an optical molasses. Here, the small hyperfine splittings of ^{39}K again serve as a complication and the ^{39}K molasses is therefore realized using the technique of Landini *et al.* [142], which takes advantage of the small hyperfine splittings causing a natural depumping into the dark $|1\rangle$ state. By ramping the light intensities and the detuning of the cooling light, the fraction of atoms coupled to the cooling light can be controlled to yield an optimal cooling power with minimal reabsorption of spontaneously emitted photons. After the optical molasses the ^{39}K and ^{87}Rb samples have temperatures of 117 µK and 35 µK, respectively [129].

4.2.2 Magnetic Trap and Evaporative Cooling

After the MOT phase, both species are pumped into the magnetically trappable $|2, 2\rangle$ state by applying a homogeneous magnetic field of 15 G while driving the σ_+ transition from $|2\rangle$ to $|2'\rangle$ using circularly polarized light. The current in the MOT coils is then increased in order to realize a quadrupole trap, and the atoms are transferred to the science cell by mechanically moving the MOT coils, which are mounted on a translational stage. Here, the atoms are transferred to another quadrupole trap composed of stationary coils, and the MOT coils are returned to their initial position.

The next cooling step consists of evaporative cooling, where the most energetic atoms are selectively removed from the trap, which lowers the temperature of the remaining atoms as the system rethermalizes. The first part of the evaporative cooling stage is performed in the quadrupole trap since it features large rethermalization rates [157]. In this stage, ^{87}Rb atoms are selectively removed using microwave radiation to transfer atoms from the $|2, 2\rangle$ state to the untrapped $|1, 1\rangle$ state. This is shown schematically in

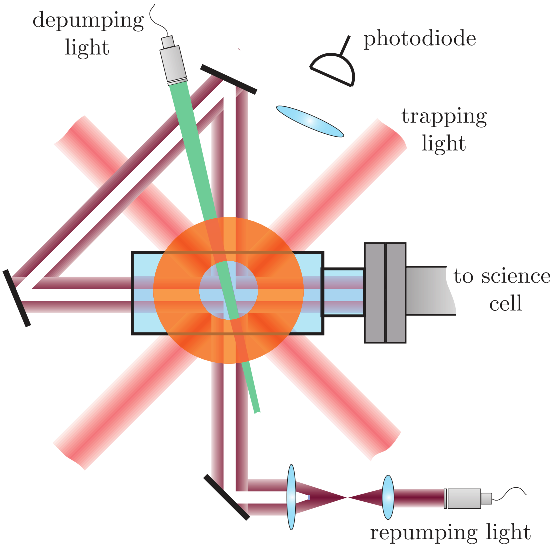

FIGURE 4.4: Schematic overview of the MOT region of the experimental apparatus. In addition to the shown trapping beams (light red), two MOT beams in the perpendicular direction to the figure plane (not shown) provide trapping and cooling along the vertical direction. The MOT beams contain the cooling light for both species and the repumping light for ^{39}K. The central part of the repump beam for ^{87}Rb (dark red) is cut out using an opaque disk and it is therefore supplied separately. Additional depumping light (green) accelerates the accumulation of ^{87}Rb atoms in the dark $|F = 1\rangle$ state. A photodiode is used to measure the fluorescence signal from the atoms in the MOT. The figure is adopted from Ref. [129] and a similar figure was published in Ref. [100].

Fig. 4.5(a) with the energy levels of the m_F states in the $F = 1$ and $F = 2$ manifolds depending on the position due to the Zeeman effect. The atoms in the trappable states are shown in red, and the microwave radiation is shown by the squiggly arrows. During evaporative cooling, the frequency of the radiation is swept to lower values, thus continuously removing the most energetic atoms as shown by the blue arrow. The employed microwave radiation is, however, also resonant with the $|1, 1\rangle \rightarrow |2, 1\rangle$ transition in the outer regions of the trap as shown in green. As a consequence, energetic ^{87}Rb atoms are reintroduced in the trap, leading to heating of the ^{39}K sample

[158, 159]. Furthermore, an additional complication in the quadrupole trap comes from Majorano spin flips at the zero point of the magnetic field, which lead to further losses [160].

In order to avoid both of these issues, the second part of the evaporative cooling is performed in a Quadrupole Ioffe-Pritchard Configuration (QUIC) trap [161], which realizes a harmonic trapping potential without a magnetic field zero as shown in Fig. 4.5(b). In this stage, additional microwave radiation (shown in red) resonant with the $|2,1\rangle \to |1,1\rangle$ transition in the centre of the trap is applied to remove the unwanted ^{87}Rb atoms [139, 140, 159]. At this point, the microwave sweep is continued until all ^{87}Rb atoms have been removed from the trap. Alternatively, the sweep is stopped before this if a ^{39}K–^{87}Rb mixture is desired, and if only ^{87}Rb atoms are loaded during the MOT phase, BECs containing $\sim 2 \times 10^5$ atoms can be realized in the QUIC trap. The total duration of the evaporative cooling stage is about 30 seconds.

4.2.3 Bose-Einstein Condensation in the Optical Dipole Trap

After removing all ^{87}Rb atoms, the ^{39}K sample is transferred to an optical dipole trap (ODT) for the final evaporation. The ODT consists of two crossed 1064 nm laser beams propagating along the horizontal x- and y-directions. This enables the magnetic field to be tunable in order to realize the positive scattering length needed for the production of stable BECs. To this end, the coils used for the quadrupole trap are reconfigured to Helmholtz configuration, which provides a homogenous magnetic field along the vertical z-direction in the centre of the science cell.

After loading the atoms into the ODT, they are transferred to the $|1,-1\rangle$ state using two consecutive rapid adiabatic passages. The first one transfers the atoms from $|2,2\rangle$ to $|2,-2\rangle$ by sweeping a radio frequency, while applying a constant magnetic field. Afterwards, the second transfer from $|2,-2\rangle$ to $|1,-1\rangle$ is performed by sweeping the magnetic field, while irradiating the sample with a constant radio frequency.

The magnetic field is then changed to 39.6 G corresponding to a scattering length of 165 a_0 as shown in Fig. 4.3, and the sample is evaporatively cooled by lowering the powers in the ODT beam in exponential ramps with a duration of $\sim$ 5 seconds depending on the desired final temperature. The

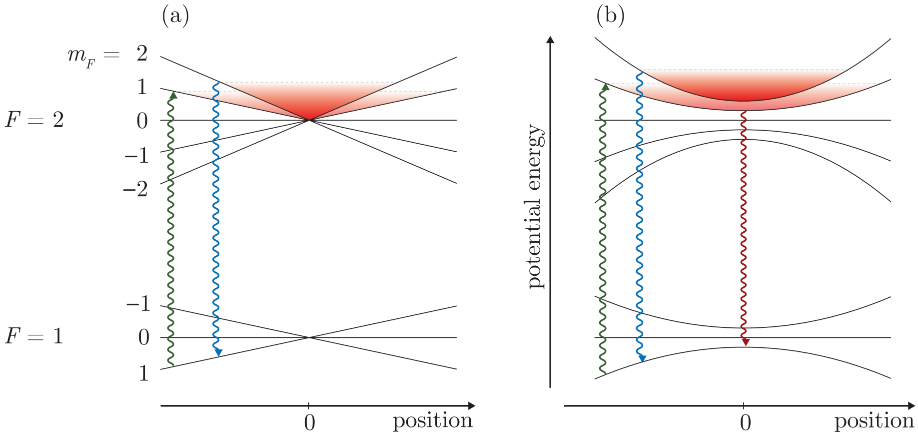

FIGURE 4.5: Schematic of the evaporative cooling in the magnetic trap. The energy levels of the states in the $F = 1$ and $F = 2$ manifolds depend on the position via the Zeeman effect. ^{87}Rb atoms (red) are selectively removed using microwave radiation resonant with the $|2, 2\rangle \rightarrow |1, 1\rangle$ transition (blue). The microwave frequency is swept to lower values, continuously removing the most energetic ^{87}Rb atoms, while the remaining ^{87}Rb and ^{39}K atoms rethermalize to a lower temperature. The same microwave radiation is resonant with the $|1, 1\rangle \rightarrow |2, 1\rangle$ transition at the edge of the trap (green), which reintroduces energetic atoms into the trap. (a) The first part of the evaporative cooling is performed in a quadrupole trap which features large rethermalization rates. (b) The second part of the evaporative cooling is performed in a harmonic QUIC trap, where the energetic atoms in state $|2, 1\rangle$ can be removed by a separate microwave frequency (red). The figure is adopted from [128].

end result is a nearly pure ^{39}K BEC of up to $\sim 1 \times 10^5$ atoms after a total experimental duration of $\sim$ 70 seconds, which serves as the starting point for the experiments described in Chs. 5 and 6.

Detection of the atoms is performed using absorption imaging after time-of-flight (TOF) expansion with a typical duration of 15 to 30 ms. The imaging is typically performed along the x-direction, which serves as the primary imaging axis, but the apparatus can also be configured for imaging along the z-direction, in order to measure the trap frequency along the x-axis.

In a typical imaging sequence, the magnetic field is kept on in the beginning of the TOF, since crossing the Feshbach resonance at 33.6 G, while the atomic density is still large, leads to losses. In order to analyse the state

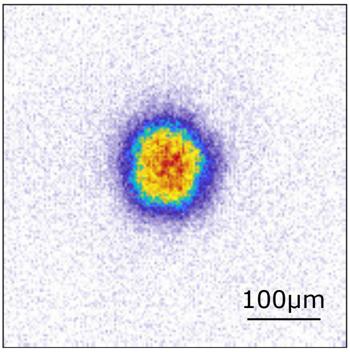

FIGURE 4.6: Typical image of a ^{39}K BEC consisting of $\sim 5 \times 10^4$ atoms after ramping the magnetic field to the vicinity of the Feshbach resonance at 114 G. The BEC is imaged after 28 ms time-of-flight. The figure is adopted from Ref. [163].

composition of the atomic cloud, one of the coils can be used to generate a magnetic field gradient during TOF, fully separating the m_F components such that the respective clouds can be analysed separately. Subsequently, the main magnetic field is turned off and a separate pair of Helmholtz coils surrounding the science cell are applied to realize a homogenous magnetic field of 1 G along the x-direction, which sets the quantization axis during imaging. Since the experiments are performed in the $F = 1$ manifold, linearly polarized repumping light resonant with the $|1\rangle \rightarrow |2'\rangle$ transition is applied along the z-direction 200 µs prior to absorption imaging. The circularly polarized detection light hits the atoms along the x-axis and drives the σ^+ transition $|2\rangle \rightarrow |3'\rangle$. An example of a typical absorption image after processing is shown in Fig. 4.6.

The extraction of atom numbers from the absorption images is calibrated using the method of Reinaudi *et al.* [162], where the saturation intensity I_0^{sat} is corrected by a dimensionless calibration parameter α^*, which accounts for the specific conditions under which the images are taken, such as the polarization of the imaging light and the structure of the involved states. More details on the calibration procedure is given in Ch. 7.

4.2.4 Magnetic Field Stabilization and Calibration

Experiments with ultracold gases generally require precise magnetic field control in order to consistently prepare the system in the same configuration, for reducing the width of spectroscopic measurements and to control the interaction strength via magnetic Feshbach resonances. To this end, several approaches are employed in order to minimize the error on the magnetic field.

After transferring the atoms to the ODT, the current source is switched to a home-built power supply consisting of a set of car batteries. These are decoupled from the 50 Hz AC signal of the power grid, and noise at 50 Hz and higher harmonics is therefore reduced. The influence of the power grid is further minimized by triggering the final parts of the experiment on the 50 Hz signal of the power grid. This is achieved by pausing the experiment until the 50 Hz signal reaches a desired phase in its period, which is measured by a small circuit. The trigger is generally enabled just before the radiofrequency (rf) pulse which typically initializes the experiment. Finally, the background magnetic field is actively stabilized using a large pair of coils surrounding the science cell, which are controlled using a proportional-derivative-integral (PID) controller connected to a magnetometer.

The magnetic field is typically calibrated by performing radiofrequency spectroscopy on the $|1,-1\rangle \rightarrow |1,0\rangle$ transition in ^{39}K using cold thermal clouds prepared by inefficient evaporative cooling in the ODT. The state composition after the rf pulse is analysed by separating the states using a magnetic field gradient as described in Sec. 4.2.3.

A typical spectroscopy signal showing the resulting population in the $|1,0\rangle$ state as a function of the applied radio frequency is shown in Fig. 4.7(a) together with a Gaussian fit to the data. The magnetic field can be extracted from the centre frequency of the spectroscopy signal using the Breit-Rabi formula (Eq. (4.4)). The measurement in panel (a) corresponds to a magnetic field of 116.412(3) G where the error is based the width of the peak. A detailed characterization of the magnetic field precision can be found in the thesis of Nils B. Jørgensen [87], where long probe pulses were used to reduce spectral width of the pulse. These measurements found a lower limit to the obtainable precision of 1 mG caused by long term drifts in the background magnetic field.

Panel (b) shows Rabi flops between the same states recorded at the same magnetic field as panel (a) together with a sinusoidal fit to the data, which yields a Rabi frequency of $\Omega/2\pi = 1.4(6) \times 10^5$ Hz. Detailed measurements of the first flank of the Rabi oscillation signal are typically used in order to determine the population in the $|1,0\rangle$ state as a function of the duration of the rf pulse as shown in Sec. 6.4.

Panels (c-d) show magnetic field calibrations for the regions used in the impurity dynamics (Ch. 5) and LHY fluid (Ch. 6) experiments. The magnetic field calibration of panel (d) has a slope of 9.47(2) G/A and an offset of −0.2(1) G. Calibrations such as those in panels (c-d) are generally made for the magnetic field regime of the specific experiment. However, if precise knowledge of the magnetic field is required, a separate spectroscopy measurement is carried out before or after the experiment.

4.3 Construction of a Spherical Optical Dipole Trap

In Ch. 6, the Lee-Huang-Yang fluid is theoretically investigated in a spherically symmetric harmonic potential, and it is shown how the monopole frequency can be used to characterize the system. As explained in Sec. 4.2.3, the apparatus is able to produce BECs in a typical crossed ODT consisting of two Gaussian beams propagating along the horizontal directions. In this configuration, realizing a spherically symmetric potential is, however, a challenge, since both beams contribute to the potential along the vertical direction making the trap asymmetric. In order to compare with the theoretical predictions and ensure excitation of the monopole mode, the ODT therefore had to be modified in order to realize equal trap frequencies in all directions. To this end, a third trapping beam along the vertical direction was added to the ODT such that two beams contribute to the potential in each direction. In this section, the setup for the additional ODT beam is described in detail.

Fig. 4.8 shows the laser system responsible for preparing the three ODT beams. The 1064 nm light is produced by a narrow bandwidth monolithic ring laser (*Coherent Mephisto*), which is amplified by a fibre amplifier (*Nufern PSFA-1064-50mW-50W-0*). After amplification, the laser light passes through two optical isolators and is split in separate paths using polarizing beam splitter cubes, where the distributions are set by adjusting the preceding half-wave plates. The beam paths labelled ODT1 and ODT2 correspond to the original trapping beams propagating along the x- and y-directions, respectively, and the path labelled ODT3 delivers laser light

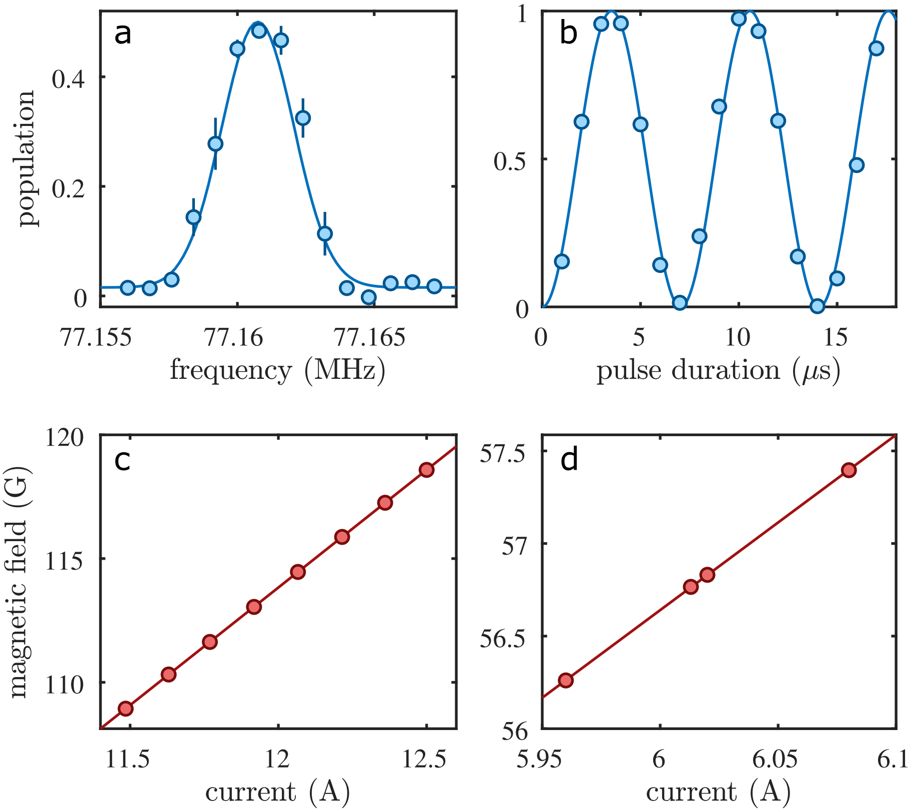

FIGURE 4.7: Typical spectroscopy signal, Rabi oscillations, and magnetic field calibrations. Radiofrequency spectroscopy signal (a) and Rabi flops (b) on the $|1,-1\rangle \rightarrow |1,0\rangle$ transition in ^{39}K. The measurements were performed at current of 12.273 A and the centre of the spectroscopy signal yields a magnetic field of 116.412(3) G based on the Breit-Rabi formula (Eq. (4.4)). The extracted Rabi frequency is $\Omega/2\pi = 1.4(6) \times 10^5$ Hz. (c-d) Magnetic field calibrations in the regions used for the impurity dynamics (c) and LHY fluid (d) experiments. The error bars are smaller than the markers.

for the vertical beam. Each beam is sent through an acousto-optic modulator (AOM), and subsequently to the experiment via polarization maintaining optical fibres. The power in each beam is controlled by adjusting the rf power that is applied to the AOM using PID controllers, which compare the set point to a photodiode signal after the optical fibre.

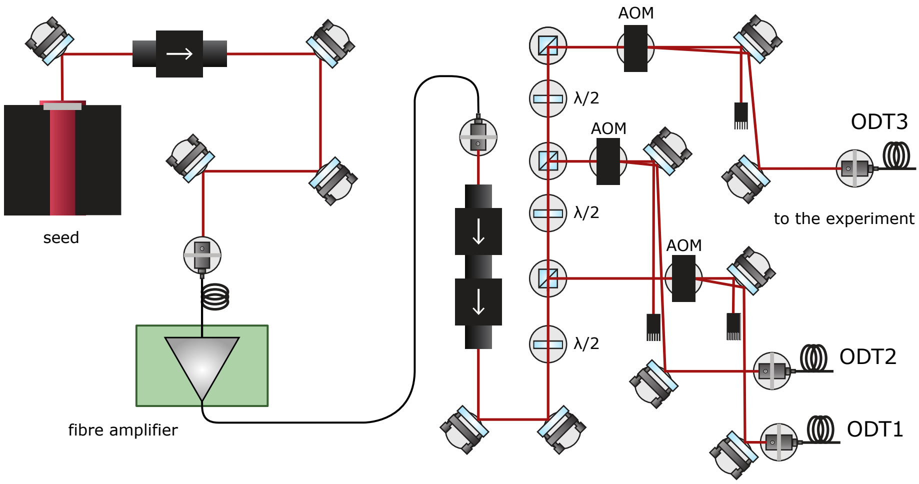

FIGURE 4.8: Schematic of the setup for generating the laser light used in the optical dipole trap. Left: The 1064 nm laser light is generated by a seed laser and amplified by a fibre amplifier. Right: The output from the fibre amplifier is split in three paths, which are sent to three separate AOMs allowing the intensity of each beam to be controlled separately. Subsequently, the three beams are sent to the experiment via optical fibres. The figure is based on earlier versions from Refs. [128, 129].

The optical setup for the ODT3 beam after the optical fibre is shown in Fig. 4.9 with panel (a) showing an overhead view of the optical breadboard above the science cell. The ODT3 light is coupled out using a fibre collimator with an f=60 mm lens, after which a polarizing beam splitter cube fixes the polarization direction. Following this, a fraction of the light is reflected of a glass plate and directed onto a photodiode, which measures the beam power. The output voltage of the photodiode serves as the process variable for the PID controller, which adjusts the laser power via the AOM in Fig. 4.8. The ODT3 beam then passes through an f=700 mm lens, which sets the beam size in the focus. A half-wave plate is used to control the polarization direction, before the beam is overlapped with the vertical imaging beam using a short-pass dichroic mirror. The beam is then directed through a hole in the optical breadboard and sent to the science cell below, which is shown from a sideways view in panel (b). The beam waist in the middle of the science cell was measured to 61 µm by directing the beam onto a camera and

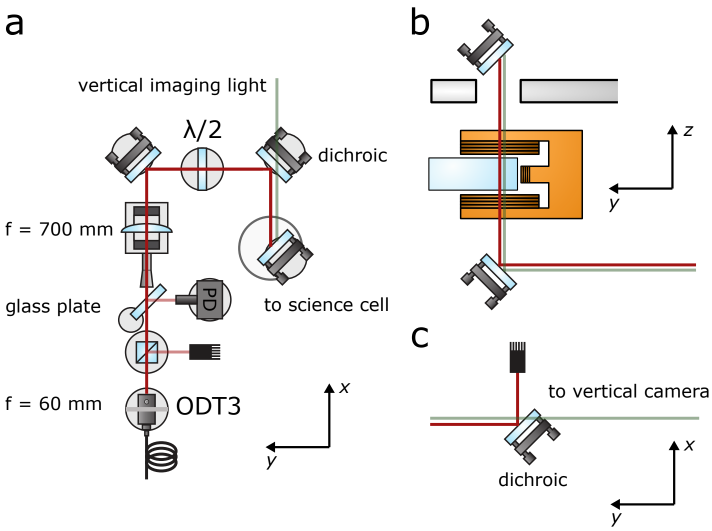

FIGURE 4.9: Schematic of the optical setup for the vertical trapping beam (ODT3). (a) Overhead view of the optical setup above the science cell. The ODT3 light (red) is coupled out from the optical fibre and the polarization is fixed by the polarizing beam splitter cube. A fraction of the light is directed onto a photodiode, which is used to control the power in the beam via a PID controller that regulates the rf power of an AOM before the optical fibre. The light then passes through an f=700 mm lens, which sets the beam size in the focus, and a half-wave plate for polarization control, before it is directed through a hole in the optical breadboard towards the science cell. The vertical imaging light is shown in green. (b) Sideways view of the science cell showing the paths of the ODT3 and imaging beams. (c) After passing through the science cell, the ODT3 beam is directed onto a beam dump via a dichroic mirror, such that it does not hit the camera used for vertical imaging.

fitting a Gaussian function to the recorded beam profile. Panel (c) shows an overhead view of the final part of the ODT3 beam setup after after passing through the science cell. Here, the ODT3 beam is separated from the vertical imaging light by a dichroic mirror, and directed onto a beam dump, such that is does not hit the vertical imaging camera.

4.4 Characterization of the Optical Dipole Trap

With the implementation of the vertical ODT beam, the trap can be made spherically symmetric by adjusting the relative intensities of the three beams. This is done by first calculating the total dipole potential from all three beams using Eq. (3.32). The trap frequencies along the three Cartesian axes are then calculated by Taylor expanding the potential around its minimum, and the beam powers are chosen such that the calculated frequencies are equal. The calculated powers serve as the starting point for a following iterative adjustment of the beam powers until the measured trap frequencies are approximately equal with a relative deviation to the geometric mean on the order of maximally 5 %.

In practice, the trap frequencies are measured by preparing a BEC in the $|1, -1\rangle$ state in the desired trap configuration. The powers in all beams are then abruptly increased by $\sim$ 10 % for 1 ms, after which the powers are once again decreased to the values giving the desired trap potential.

Along the vertical direction, the gravitational potential generally lowers the location of the trap center, such that the atomic cloud is slightly lowered compared to crossing point of the horizontal ODT beams. Increasing the horizontal ODT powers thus raises the location of the trap minimum resulting in vertical dipole oscillations after returning to the desired trap. Along the horizontal directions, the method relies on the vertical ODT beam being slightly misaligned compared to the crossing of the horizontal beams, such that increasing the power of the vertical beam relative to the horizontal beams shifts the trap minimum towards the focus of the vertical beam. In practice, the magnitudes of the relative changes are adjusted such that clear dipole oscillations of the atomic cloud are realized at the lowest possible amplitude to stay within the harmonic part of the Gaussian trap potential.

Following a variable evolution time, the BEC is subsequently released from the trap and imaged after TOF expansion with a duration of 28 ms. To measure the trap frequencies along all Cartesian axes, separate measurements are carried out with absorption imaging along the x- and z-directions.

Due to imperfections in the optical setup, the axes of the trapping potential lie in a frame (x', y', z'), which is rotated with respect to the reference frame (x, y, z) set by the imaging axes. The resulting oscillation data measured in the (x, y, z) frame thus corresponds to a beat signal between the eigenmodes of frequency ω'_i, $i = x, y, z$, in the reference frame of the trap, which can be obtained by implementing a rotation of the coordinate system in the analysis [164–166]. In practice, the centre-of-mass motion in the reference frame of the trap is assumed to be described by

$$\mathbf{r}' = \begin{bmatrix} A_x \sin(\omega'_x t + \phi_x) \\ A_y \sin(\omega'_y t + \phi_y) \\ A_z \sin(\omega'_z t + \phi_z) \end{bmatrix}, \tag{4.6}$$

where A_i, ω'_i, and ϕ_i are the amplitudes, angular frequencies, and phase offsets of the oscillations. In the reference frame defined by the imaging setup, the position of the atomic cloud is then given by

$$\mathbf{r} = \mathbf{R}_z(\theta_z)\mathbf{R}_y(\theta_y)\mathbf{R}_x(\theta_x)\mathbf{r}', \tag{4.7}$$

where $\mathbf{R}_i(\theta_i)$ is the basic rotation matrix which rotates the coordinate system around axis i'. To extract the trap frequencies ω'_i, Eq. (4.7) is simultaneously fitted to the cloud positions measured using the x- and z-imaging systems.

In Fig. 4.10 typical data from a trap frequency measurement is shown together with a fit of Eq. (4.7). Panels (a-b) show data with imaging in the x-direction, and panels (c-d) show the data with imaging in the z-direction. The x-, y- and z-component of the fitted position $\mathbf{r}$ are shown in green, blue, and red, respectively. The experimental sequences are identical except for the difference in imaging directions.

The fit of Eq. (4.7) to the data yields trap frequencies $\omega'_x = 2\pi \times 118.5(1)\,\text{Hz}$, $\omega'_y = 2\pi \times 115.3(2)\,\text{Hz}$, and $\omega'_z = 2\pi \times 108(1)\,\text{Hz}$, and rotation angles $\theta_x = 101(4)^\circ$, $\theta_y = 120(2)^\circ$, and $\theta_z = -125(3)^\circ$, where the large rotation angles are not unexpected due to the small difference between the trap frequencies. The three frequencies are then combined into a geometric mean $\omega_0 = (\omega'_x\omega'_y\omega'_z)^{1/3}$, which results in $\omega_0 = 2\pi \times 113.7(1)\,\text{Hz}$ for the shown data set.

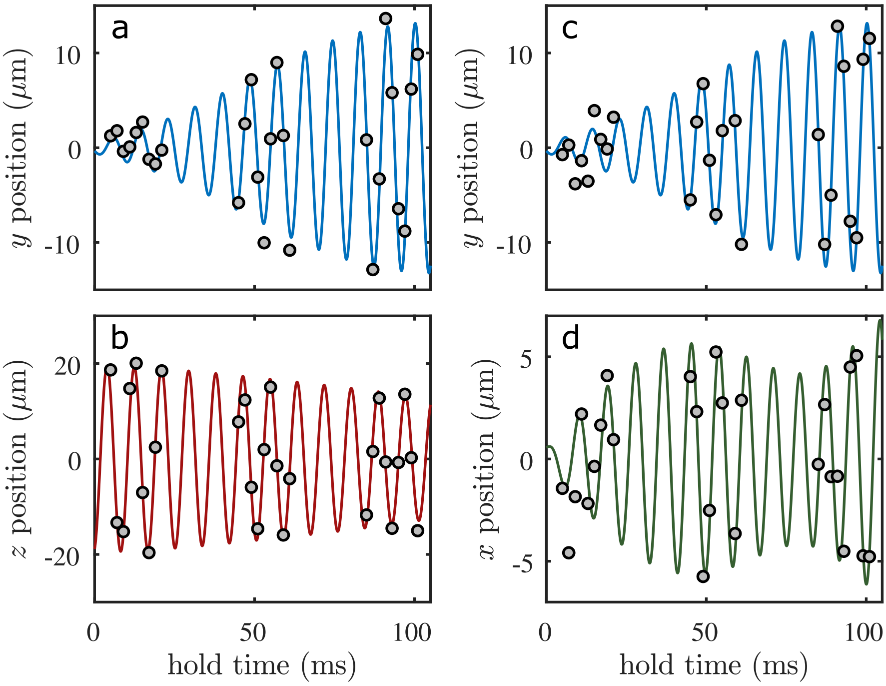

FIGURE 4.10: Typical trap frequency measurement. The cloud positions after time-of-flight expansion are shown for imaging along the x- (a-b) and z-axes (c-d), together with a simultaneous fit of Eq. (4.7) to data from both imaging directions. The x-, y- and z-component of the fitted position $\mathbf{r}$ are shown in green, blue, and red, respectively. The y-positions are different within the two data sets due to the destructive imaging technique. A similar figure was published in Ref. [54].

CHAPTER 5

Impurity Dynamics

The concept of an impurity interacting with a surrounding medium is a general problem in physics and finds application in many fields. The most prominent example is that of electrons interacting with a crystal lattice as considered by Landau and Pekar [34–36], where the electron charge disturbs the crystal lattice leading to a local polarization. As a result, the electron is dressed by the lattice phonons and together, the electron and the surrounding disturbance can be described as a quasiparticle called a polaron as shown schematically in Fig. 5.1(a). Since its first conceptualization, the polaron picture has found application in many contexts and is an important concept when describing many-body systems ranging from ^{3}He-^{4}He mixtures [167], high-temperature superconductors [37, 168], colossal magnetoresistance [169], organic semiconductors [170], and Λ-particles in nuclear matter [38].

Within the last decade, the polaron problem has received significant attention in the ultracold gas community, where the polaron scenario can be realized by introducing a minority component of another state or species in a quantum gas as pictured in Fig. 5.1(b). The high controllability offered in these systems allows systematic studies of the polaron across different interaction strengths and dimensions, and furthermore, the diluteness of ultracold gases results in density-dependent timescales being sufficiently large for time-resolved experiments.

In this chapter, an experiment is presented which makes use of this feature to probe the short-time dynamics of impurities immersed in a BEC. By employing a Ramsey-type interferometry scheme, the characteristic timescales of the dynamical evolution are extracted and the onset of polaron formation is observed. These results have been published in Refs. [51, 52] and was presented in the PhD thesis of Magnus G. Skou [163]. Since publication of Ref. [51] the data has been reanalysed based on an improved calibration of the atom numbers from the absorption images. When comparing the contents of this chapter to that of Ref. [51], minor differences in the data and theoretical results are therefore visible, however, as the data depends only weakly on the atom numbers through the density, the main conclusions are the same as in the publication.

The chapter is structured as follows. First, a general introduction to polarons in ultracold quantum gases is given in Sec. 5.1. Subsequently, the experimental method used to probe the dynamical evolution of impurities in a BEC is presented in Sec. 5.2, and in Sec. 5.3, the relation between the experimental signal and the impurity coherence is presented. In Sec. 5.4, the theoretical predictions for dynamical behaviour of the coherence are presented, which is followed by descriptions of the primary experimental decoherence mechanisms in Sec. 5.5. Following this, the experimental results are presented in Sec. 5.6 and compared to the theoretical predictions. Finally, the chapter is summarized in Sec. 5.7 and possible future research directions are discussed.

My primary contributions in this chapter have been in the designing and conducting the experiments with some involvement in the data analysis, which was mainly carried out by Magnus G. Skou. The theoretical description of the experiment presented in Secs. 5.3 and 5.4 was developed by our collaborators Kristian K. Nielsen and Arturo Camacho-Guardian of the research groups lead by Thomas Pohl and Georg M. Bruun.

5.1 Polarons in Ultracold Quantum Gases

Within the field of ultracold quantum gases, polarons have been investigated in both fermionic and bosonic mediums. In both types of experiments, the impurity picture is fulfilled by immersing a minority component into majority component, which can either be a degenerate Fermi gas or a BEC. The quantum statistics of the impurity component is generally not crucial

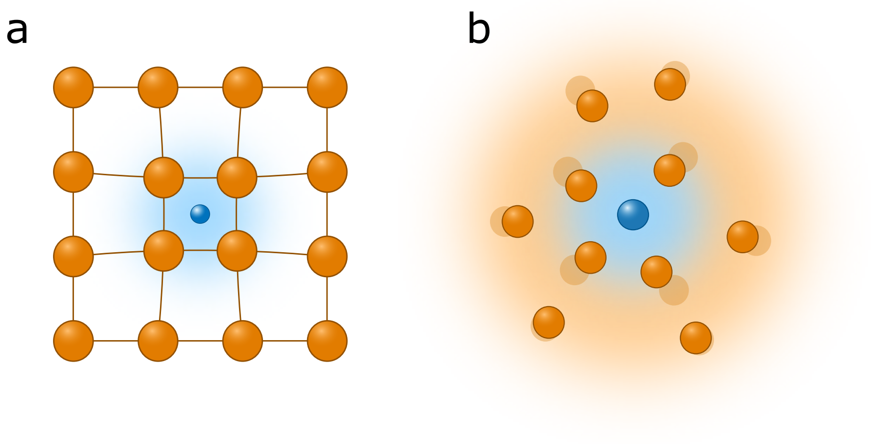

Figure 5.1: Polarons in solid-state physics and quantum gases. (a) An electron (blue) perturbs the crystal lattice (orange) forming a polaron composed of the electron dressed by lattice phonons. (b) An impurity atom (blue) interacts attractively with a surrounding gas of medium atoms (orange) leading to a polaron composed of the impurity atom and the surrounding medium atoms. The figure is adopted from Ref. [163].

since in most cases, impurity-impurity interactions can be neglected due to the low concentration. In the case of a bosonic medium used in this work, the medium atoms are often just labelled as bosons and parameters regarding these are denoted by the subscript B.

The impurity-boson interaction strength is typically characterized by the inverse interaction strength $1/k_n a$, where a is the impurity-boson scattering length and $k_n = (6\pi^2 n_\mathrm{B})^{1/3}$ is the characteristic wavenumber with the condensate density n_B. By employing a Feshbach resonance between the impurity and medium atoms, a can be tuned from $-\infty$ to ∞, and the sign of $1/k_n a$ thus corresponds to attractive (negative) or repulsive (positive) interactions. The interaction strength increases for $1/k_n a \to 0$, which corresponds to the unitary regime of the Feshbach resonance as described in Sec. 2.2.1. The condensate density sets the energy scale $E_n = \hbar^2 k_n^2 / 2m_\mathrm{B}$, where m_B is the mass of the condensate bosons and E_n is independent of the interactions strength.

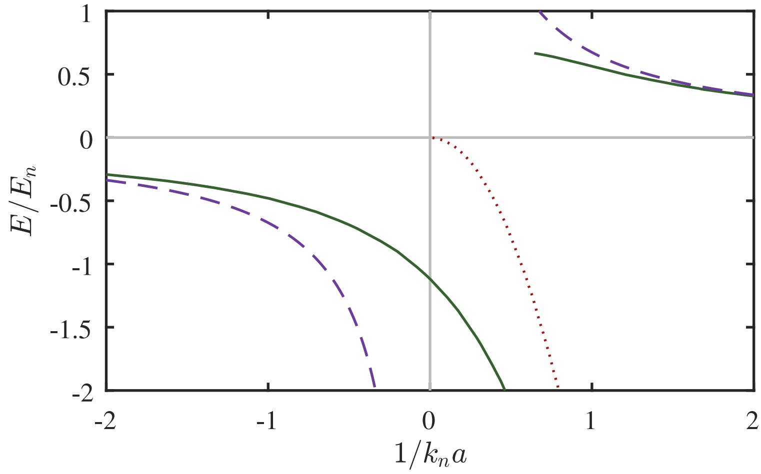

FIGURE 5.2: Energy diagram of the Bose polaron. The energy of the Bose polaron calculated using a diagrammatic approach is shown in green [138], the mean-field energy is shown in dashed purple, and the molecule binding energy is shown in dotted red. The figure is adopted from Ref. [163].

In Fig. 5.2 the energy diagram of the Bose polaron is shown as a function of $1/k_n a$. A diagrammatic prediction for the polaron energy [138] (green) is compared to the mean-field energy $E_{\mathrm{mf}} = 2\pi\hbar^2 n_{\mathrm{B}}\, a/m_{\mathrm{r}}$ (dashed purple), and the binding energy of the molecule associated with the Feshbach resonance $\hbar^2/2m_{\mathrm{r}}\, a^2$ (dotted red), where m_{r} is the reduced mass of the impurity and medium atoms. For attractive interactions ($1/k_n a < 0$) the polaron energy corresponds to the mean-field energy in the weakly-interacting limit, however, for stronger interactions E_{mf} diverges indicating the breakdown of the mean-field picture. In contrast, the energy of the attractive polaron decreases when approaching the resonance and crosses it to approach the molecular energy. This can be understood from the qualitative argument that the extreme case of the attractive polaron is a molecule. On the repulsive side ($1/k_n a > 0$) the polaron energy becomes increasingly damped when approaching the resonance as it can decay into the molecule state and the lower lying attractive polaron state.

In addition to the energy spectrum, the polaron is characterised by its effective mass and the quasiparticle residue Z. The effective mass is modified compared to the bare impurity due to the interactions with the medium, and in the bosonic case, it can be interpreted as the impurity dragging along a cloud of virtual phonons [171]. The quasiparticle residue defined as $\sqrt{Z} = \langle \psi_{\text{non-int}} | \psi_{\text{pol}} \rangle$ describes how much of the non-interacting state $|\psi_{\text{non-int}}\rangle$ is contained in the polaron state $|\psi_{\text{pol}}\rangle$.

5.1.1 Fermi Polarons

The first polaron experiments in ultracold gases were performed using impurities immersed in a Fermi sea [172, 173], and such experiments serve as an important platform for investigating Fermi liquid theory [167], the Anderson orthogonality catastrophe [174] and the Kondo effect [175]. The first observation of polarons in ultracold gases was published in 2009 where rf spectroscopy was used to extract the polaron energy and quasiparticle residue on the attractive side of a Feshbach resonance [39]. Following this, the effective mass of the Fermi polaron was obtained from collective excitations [40] and from measurements of the equation of state [41]. Subsequently, the repulsive Fermi polaron was observed in rf spectroscopy experiments in two [42] and three dimensions [43]. Complementary to the spectroscopic measurements, the Fermi polaron was investigated in time-domain using Ramsey interferometry [44, 45], and further spectroscopic measurements have investigated the Fermi polaron at resonant interactions [176], as a function of temperature [46], and across an orbital Feshbach resonance [47].

5.1.2 Bose Polarons

As shown in Sec. 2.4, the low-energy excitations of a BEC follow a linear dispersion similar to phonons in a crystal, and the analogy to the solid-state polaron is thus generally stronger than for fermions. Seven years after the first observation of Fermi polarons, the generic Bose polaron was observed in parallel spectroscopic measurements of the polaron energy spectrum, which were performed at JILA [49] and by our group [48, 138]. In addition to these experiments, several groups have investigated impurities immersed in a Bose gas in various settings such as fixed impurities [177–179], impurities in an uncondensed medium [180], and in one dimension [181, 182]. Most recently, the temperature dependence of the polaron was measured in spectroscopy experiment on equilibrated ground state polarons [50]. Since the first experimental observations of the Bose polaron, there has been great theoretical interest in its formation dynamics [183–187], which, as in the fermionic case [44, 45, 188], can be tracked by measuring the coherence of the system using an interferometric sequence [44, 45, 178, 179, 189]. In the following sections, an experiment is presented, where a modified Ramsey interferometry scheme is employed to track the dynamical evolution of the system from a coherent superposition state with a minority component into polaronic quasiparticles.

5.2 Experimental Method

The experiment starts with a ^{39}K BEC in the $|F = 1, m_F = -1\rangle \equiv |1\rangle$ state prepared in an optical dipole trap as described in Ch. 4. The employed trap has a geometric mean of the trap frequencies $\sim 2\pi \times 65\,\mathrm{Hz}$ resulting in an average condensate density $n_\mathrm{B} \simeq 1 \times 10^{14}\,\mathrm{cm}^{-3}$, which sets the corresponding timescale $t_n = \hbar/E_n \simeq 4\,\mu\mathrm{s}$. In order to realize the Bose polaron, the same method as in Ref. [48] is employed, where a small fraction of the population is transferred to the $|F = 1, m_F = 0\rangle \equiv |2\rangle$ state, which acts as impurities in a medium composed of the initial BEC in the $|1\rangle$ state.

The impurity-boson scattering length a is tuned via a Feshbach resonance at 113.8 G [48, 86, 146], where conveniently, the boson-boson scattering length is approximately constant at $a_\mathrm{B} \simeq 9\,a_0$. The Feshbach resonance structure of the relevant states is shown in Fig. 5.3 with the experimentally investigated regime shown in grey shading. Within this regime, the impurity-impurity scattering length is constant and negative at $\sim -20a_0$, however since the population in the impurity state is small, impurity-impurity interactions can be neglected. For the experiments presented here, a is generally restricted to negative values and the unitary limit ($a \to \pm\infty$), since the energy spectrum of the polaron is simpler on the attractive side of the Feshbach resonance as shown in Fig. 5.2.

In order to study the dynamical evolution leading to polaron formation, the experimental sequence has to first prepare, and then probe the system after a given evolution time. In practice, this is done by employing a modified Ramsey scheme, shown schematically in Fig. 5.4 using the collective spin

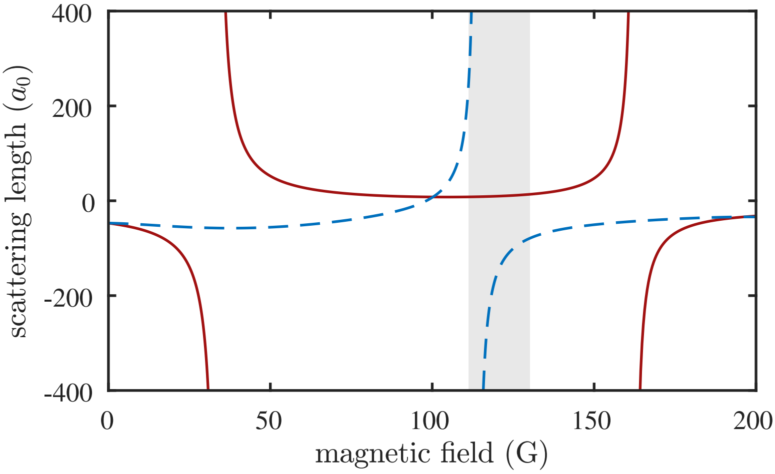

FIGURE 5.3: Relevant Feshbach resonances for the impurity dynamics experiment. The scattering length between atoms in state $|1\rangle$ is shown in red [84], and between atoms in states $|1\rangle$ and $|2\rangle$ is shown in dashed blue [86]. The grey area shows the magnetic field regime, where the experiments are performed.

on the Bloch sphere [190]. Instead of the usual Ramsey scheme discussed in Sec. 3.5, the orientation of the Bloch vector is kept close to the initial one, which ensures a low population in the impurity state. In practice, the interferometric sequence is initialized by a 0.5 µs radiofrequency (rf) pulse tuned to the atomic resonance frequency between states $|1\rangle$ and $|2\rangle$, which prepares the system in a superposition state with $\sim 5\,\%$ of the population in the impurity state (panel (a)). Subsequently, the system is allowed to evolve for a time t with phase evolution and decoherence determined by the interactions between the impurity state and the surrounding BEC (panel (b)). Finally, the interferometric sequence is closed by a second rf pulse with variable phase φ (panel (c)). After the interferometric sequence, the system is held in the ODT for a duration of 2 ms, where three-body loses remove the remaining population in the impurity state. The result of the interferometric sequence is a sinusoidal dependence of the final number of atoms in the $|1\rangle$ state on the probe phase

$$N(\varphi, t) = N_0 - \mathcal{A}(t) \cos\left(\varphi - \varphi_C(t)\right), \tag{5.1}$$

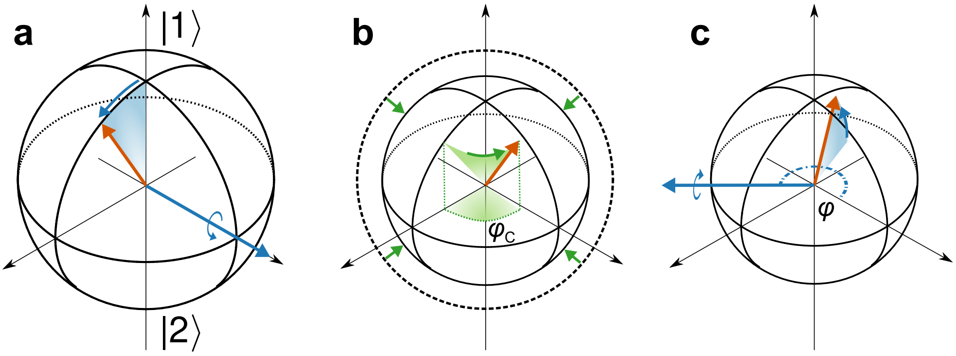

Figure 5.4: Schematic of the interferometric sequence illustrated using the collective spin on the Bloch sphere. The north pole represents the initial state $|1\rangle$ of the BEC and the south pole represents the impurity state $|2\rangle$. (a) A short radiofrequency pulse prepares the system in a population imbalanced collective superposition state. (b) The subsequent evolution due to interactions between the impurity state and the bosonic environment results in a phase evolution φ_C and a contraction of the Bloch sphere. (c) A second pulse with variable phase φ rotates the Bloch vector again. A similar figure was published in Ref. [51]

where N_0 is the average number of atoms after the sequence, and $\mathcal{A}(t)$ and $\varphi_C(t)$ are the amplitude and phase of the oscillations, respectively. The final number of atoms in $|1\rangle$ after the interferometry sequence is measured using absorption imaging after 28 ms of TOF expansion, and Eq. (5.1) is fitted to the data. Example interference signals are shown for $1/k_n a = -1.8$ in Fig. 5.5 and as seen, the measured amplitude and phase depend on the time between the interferometry pulses. In following sections, it is shown how the amplitude and phase of the interferometry signal are directly related to the impurity coherence, which has a temporal evolution determined by the interactions between the impurity and medium state.

5.3 Theoretical Model of the Pulse Sequence

As mentioned, the experimentally measured interference signal is directly related to the impurity coherence. This connection follows from a theoretical model of the pulse sequence, which is outlined in this section. A more

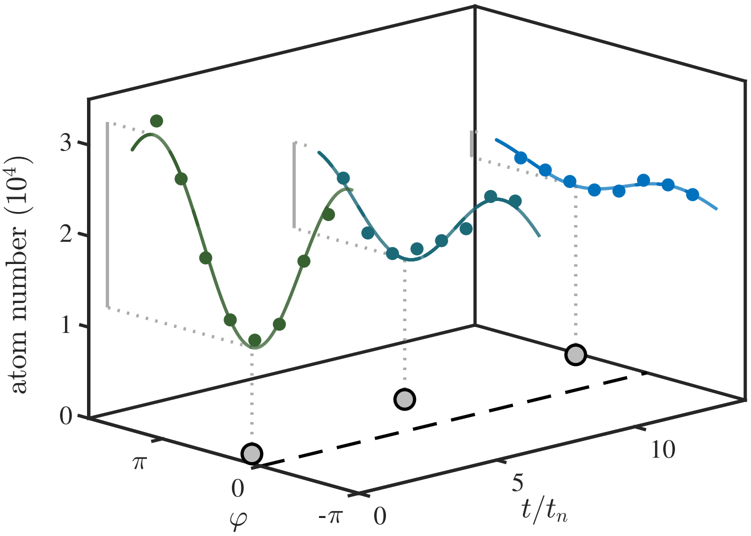

FIGURE 5.5: Interference signal recorded at different evolution times for $1/k_n a = -1.8$. The final atom number is shown as a function of the probe phase and evolution time, and the solid lines are fits of Eq. (5.1) to the data. The grey lines and open circles show the extracted amplitude and phase, respectively. A similar figure was published in Ref. [51].

detailed description can be found in the supplemental information of Ref. [51].

The experimental sequence can be modelled theoretically by considering the combined effect of the three steps shown in Fig. 5.4. Initially the system is in the condensed state $|\mathrm{BEC}\rangle$ with no impurities present. The experiment is then initialized by a rf pulse with phase $\varphi = 0$, duration δt, and where Ω is the Rabi frequency. The Hamiltonian for the rf transfer can be written in the rotating frame as

$$H_{\mathrm{rf}}(\varphi) = \hbar\Omega \sum_{\mathbf{k}} \left[e^{+i\varphi} c_{\mathbf{k}}^{\dagger} b_{\mathbf{k}} + e^{-i\phi} b_{\mathbf{k}}^{\dagger} c_{\mathbf{k}}\right], \tag{5.2}$$

where the operators $b_{\mathbf{k}}^{\dagger}$ and $c_{\mathbf{k}}^{\dagger}$ create an atom with momentum $\mathbf{k}$ in the medium and impurity states, respectively. Following the pulse, the system is allowed to evolve for duration t under the system Hamiltonian

$$H = \sum_{\mathbf{k}} \epsilon_{\mathbf{k}} \left(c^\dagger_{\mathbf{k}} c_{\mathbf{k}} + b^\dagger_{\mathbf{k}} b_{\mathbf{k}} \right) + \frac{\mathcal{T}_\mathrm{B}}{2\mathcal{V}} \sum_{\mathbf{k},\mathbf{q},\mathbf{p}} b^\dagger_{\mathbf{k}+\mathbf{p}} b^\dagger_{\mathbf{q}-\mathbf{p}} b_{\mathbf{q}} b_{\mathbf{k}} + \frac{\mathcal{T}}{\mathcal{V}} \sum_{\mathbf{k},\mathbf{q},\mathbf{p}} b^\dagger_{\mathbf{k}+\mathbf{p}} c^\dagger_{\mathbf{q}-\mathbf{p}} c_{\mathbf{q}} b_{\mathbf{k}}, \tag{5.3}$$

where impurity-impurity interactions have been neglected, $\epsilon_{\mathbf{k}} = \hbar^2 \mathbf{k}^2/2m$, m is the mass of ^{39}K, and $\mathcal{V}$ is the system volume. Here $\mathcal{T} = 4\pi\hbar^2 a/m, \mathcal{T}_\mathrm{B} = 4\pi\hbar^2 a_\mathrm{B}/m$ are the zero energy scattering matrices for the impurity-boson and boson-boson interactions, respectively. Finally the rf evolution operator is applied again with a variable phase φ. Since the durations of the rf pulses in the experiment are shorter than the subsequent dynamics, the time evolution operator can be split in three parts

$$\mathcal{U}_\mathrm{tot}(t) = \mathcal{U}_\mathrm{rf}(\varphi, \delta t) \mathcal{U} \mathcal{U}_\mathrm{rf}(0, \delta t), \tag{5.4}$$

where $\mathcal{U}_\mathrm{rf}(\varphi, \delta t) = e^{-iH_\mathrm{rf}(\varphi)\delta t}$ and $\mathcal{U} = e^{-iHt}$. By requiring that $\Omega\delta t \ll 1$ to stay in the single impurity limit, the rf evolution operator can be expanded to second order in $\Omega\delta t$,

$$\mathcal{U}_\mathrm{rf}(\varphi, \delta t) \simeq 1 - iH_\mathrm{rf}(\varphi)\delta t - \frac{(H_\mathrm{rf}(\varphi)\delta t)^2}{2}. \tag{5.5}$$

The mean number of atoms in the impurity state after the two pulses can then be determined to

$$\begin{aligned} N_\mathrm{c}(t) &= \langle \mathrm{BEC} | \mathcal{U}^\dagger_\mathrm{tot}(t) \sum_{\mathbf{k}} c^\dagger_{\mathbf{k}} c_{\mathbf{k}} \mathcal{U}_\mathrm{tot}(t) | \mathrm{BEC} \rangle \\ &= N_\mathrm{B}\, 2(\Omega\delta t)^2 \mathrm{Re} \left[1 + e^{-i\varphi} i G_\mathrm{bc}(t) \right], \end{aligned} \tag{5.6}$$

where N_B is the initial number of atoms in the condensate and

$$G_\mathrm{bc}(t) = -\frac{i}{N_\mathrm{B}} \sum_{\mathbf{k},\mathbf{q}} \langle \mathrm{BEC} | b^\dagger_{\mathbf{k}}(t) c_{\mathbf{k}}(t) c^\dagger_{\mathbf{q}}(0) b_{\mathbf{q}}(0) | \mathrm{BEC} \rangle \tag{5.7}$$

is the impurity-boson Green's function with $c_{\mathbf{k}}(t) = \mathcal{U}^\dagger(t) c_{\mathbf{k}}(0) \mathcal{U}(t)$ the time-evolved annihilation operator for the impurity, and likewise for $b_{\mathbf{k}}(t)$.

Since the medium atoms are condensed in the zero-momentum mode, the dominant contribution to G_{bc} comes from $k = q = 0$ such that

$$G_{\mathrm{bc}}(t) \simeq -i\langle \mathrm{BEC}|c_0(t)c_0^\dagger(0)|\mathrm{BEC}\rangle = G_0(t), \tag{5.8}$$

using $b_0|\mathrm{BEC}\rangle \simeq \sqrt{N_{\mathrm{B}}}\,|\mathrm{BEC}\rangle$ and $\langle \mathrm{BEC}|b_0^\dagger(t) \simeq \langle \mathrm{BEC}|b_0^\dagger(0) \simeq \sqrt{N_{\mathrm{B}}}\,\langle \mathrm{BEC}|$ under the assumption that the impurity dynamics has negligible effect on the BEC. The impurity-boson Green's function is related to the normalized impurity coherence through $iG_0(t) = C(t)/C(0)$ [184]. By setting $C(0) = 1$ and dividing out the system volume $\mathcal{V}$, the impurity density after the two rf pulses becomes

$$n_{\mathrm{c}}(t) = n_{\mathrm{B}}\, 2(\Omega\delta t)^2 \mathrm{Re}\left[1 + e^{-i\varphi}C(t)\right], \tag{5.9}$$

where $n_{\mathrm{B}} = N_{\mathrm{B}}/\mathcal{V}$ is the initial density.

Since the experiment is performed in a harmonic trap, the atomic density is spatially dependent. This can be taken into account by performing a local density approximation $n_{\mathrm{c}}(\mathbf{r},t) = n_{\mathrm{B}}(\mathbf{r})2(\Omega\delta t)^2\mathrm{Re}\left[1 + e^{-i\varphi}C(\mathbf{r},t)\right]$ with $C(\mathbf{r},t)$ being the local coherence. The number of impurities after the two rf pulses then becomes

$$N_{\mathrm{c}} = \int \mathrm{d}^3r\, n_{\mathrm{c}}(\mathbf{r},t) = N_{\mathrm{B}}\, 2(\Omega\delta t)^2 \mathrm{Re}\left[1 + e^{-i\varphi}C(t)\right], \tag{5.10}$$

where $C(t) = \int \mathrm{d}^3r\, n(\mathbf{r})C(\mathbf{r},t)/N_{\mathrm{B}}$ is now the trap averaged coherence. Three-body recombination after the pulse sequence results in the two medium atoms being removed for every impurity and the final remaining number of atoms is then

$$\begin{aligned} N &= N_{\mathrm{B}} - 3N_c = N_{\mathrm{B}}\left(1 - 6(\Omega\delta t)^2\mathrm{Re}\left[1 + e^{-i\varphi}C(t)\right]\right) \\ &= N_0 - 6N_{\mathrm{B}}(\Omega\delta t)^2|C(t)|\cos(\varphi - \varphi_{\mathrm{C}}(t)), \end{aligned} \tag{5.11}$$

where $N_0 = N_{\mathrm{B}}(1 - 6(\Omega\delta t)^2)$ and the coherence has been expressed in terms of its amplitude and phase $C(t) = |C(t)|e^{i\varphi_{\mathrm{C}}(t)}$. It can now be seen that the final atom number has the same form as Eq. (5.1) which is fitted to the interference signal, and the normalized coherence amplitude $|C(t)| = |\mathcal{A}(t)/\mathcal{A}(0)|$ and phase $\varphi_{\mathrm{C}}(t)$ can be extracted from fits of Eq. (5.1) to the data.

5.4 Theoretical Description of Impurity Dynamics

With the connection between the experimental signal and the impurity coherence established, the theoretical prediction for the temporal evolution of the coherence is now considered. The impurity coherence is in general equal to the Fourier transform of the impurity spectral function $A(\omega)$ at zero momentum

$$C(t) = \frac{1}{2\pi}\int_{-\infty}^{+\infty} \mathrm{d}\omega\, A(\omega) e^{-i\omega t}, \tag{5.12}$$

where $A(\omega)$ describes the probability that a particle with momentum $\mathbf{k}$ (here zero) has energy $\hbar\omega$ and is thus related to the experimental spectra obtained in spectroscopy measurements [39, 42, 43, 46, 47, 49, 50, 176]. Since there is no exact expression for the spectral function for arbitrary interaction strengths, the theoretical predictions for the coherence depends on the regime of validity for the model of $A(\omega)$ used in Eq. (5.12).

5.4.1 Short-Time Behaviour of the Coherence

The short-time behaviour of the coherence is determined by the high-energy part of the spectral function. In this limit, the spectral function is determined by two-body physics and an exact expression for $A(\omega)$ can be determined [191]

$$\lim_{\omega\to\infty} A(\omega) = \frac{1}{2\pi}\frac{C_2}{N_\mathrm{B}}\sqrt{\frac{\hbar}{m}}\frac{\left(a/a_\mathrm{B} - 1\right)^2}{1 + ma^2\,\omega/\hbar}\cdot\frac{1}{\omega^{3/2}} = \frac{K}{1+\omega t_a}\cdot\frac{1}{\omega^{3/2}}. \tag{5.13}$$

Here $C_2 = 8\pi m {a_\mathrm{B}}^2/\hbar^2 \cdot \mathrm{d}E_\mathrm{BEC}/\mathrm{d}a_\mathrm{B}$ is the two-body contact of the BEC, $K = (4/3\pi)\cdot(1 - a_\mathrm{B}/a)^2 (k_n|a|)^3/\sqrt{t_a}$, and $t_a = ma^2/\hbar$. By Fourier transforming Eq. (5.13), the following expression for the coherence can be obtained

$$C(t) \simeq 1 - i\frac{E_\mathrm{mf}\, t}{\hbar} + \frac{2}{3\pi}(k_n|a|)^3\left[1 - \frac{2}{\sqrt{\pi}} e^{it/t_a}\Gamma\left(\frac{3}{2}, i\frac{t}{t_a}\right)\right], \tag{5.14}$$

where $E_\mathrm{mf} = 4\pi\hbar^2 n_\mathrm{B}\, a/m$ is the mean-field energy due to impurity state interactions with the BEC and Γ is the incomplete gamma function. Since

Eq. (5.13) is valid for high energies, Eq. (5.14) describes the coherence in the short-time limit. Equation (5.14) has the limiting forms

$$C(t) = \begin{cases} 1 - (1-i)\frac{16}{9\pi^{3/2}}\left(\frac{t}{t_n}\right)^{3/2} & t \ll t_a \\ 1 + \frac{2}{3\pi}(k_n|a|)^3 - iE_{\mathrm{mf}}\,t/\hbar - (1+i)\left(\frac{t}{t_{\mathrm{w}}}\right)^{1/2} & t \gg t_a. \end{cases} \tag{5.15}$$

That is, for short times $t \ll t_a$ the coherence evolves universally with a power-law exponent of 3/2 and timescale t_n which is independent of interaction strength. Conversely, for $t \gg t_a$ the dynamics is governed by the mean-field phase evolution $E_{\mathrm{mf}}\,t/\hbar$ and the coherence decays with a power-law exponent of 1/2 on the interaction strength dependent timescale $t_{\mathrm{w}} = m/32\pi\hbar n_{\mathrm{B}}{}^2 a^4$. Note, that the limiting cases of Eq. (5.15) are still only valid in the short-time regime.

The origin of the power laws in Eq. (5.15) can be traced back to the cross section $\sigma(k) = 4\pi a^2/(1+(ka)^2)$ for s-wave scattering between the impurity and a boson from the condensate with wavenumber k. At time t the characteristic collision energy is given by $E \sim \hbar/t$ such that $k = \sqrt{2mE}/\hbar \sim \sqrt{m/\hbar t}$ and the typical velocity of the collision partners is $v \sim \sqrt{\hbar/mt}$. For short times $t \ll t_a$, the collision energies are high such that $ka \gg 1$. The cross section then becomes $\sigma \sim 1/k^2 = \hbar t/m$. Assuming that the decoherence is caused by collisions, the coherence changes by $\dot{C}(t) = -n_{\mathrm{B}}\,\sigma v$. Integrating while setting $C(0) = 1$ then yields the $(t/t_n)^{3/2}$ power law of Eq. (5.15). The same arguments can be used for $t \gg t_a$ which yields the $(t/t_{\mathrm{w}})^{1/2}$ power law. The time t_a thus marks the crossover from high-energy unitarity limited scattering with a cross section independent of a, to the weak coupling regime with a cross section $\sim a^2$.

5.4.2 Many-Body Dynamics

Beyond the regime of two-body scattering described by Eqs. (5.14) and (5.15), the dynamics of the system is governed by many-body physics. To describe this regime, a diagrammatic theory [138, 192] can be used to obtain the zero-temperature spectral function

$$A(\omega) = Z2\pi\delta(\omega - \omega_P) + 8\pi\frac{\hbar^{3/2}n_{\mathrm{B}}}{m^{3/2}\omega^{5/2}} \cdot \frac{\Theta(\omega)}{1 + \frac{\hbar}{ma^2\omega}\left(1 - \frac{4\pi\hbar n_{\mathrm{B}}a}{m\omega}\right)^2}. \tag{5.16}$$

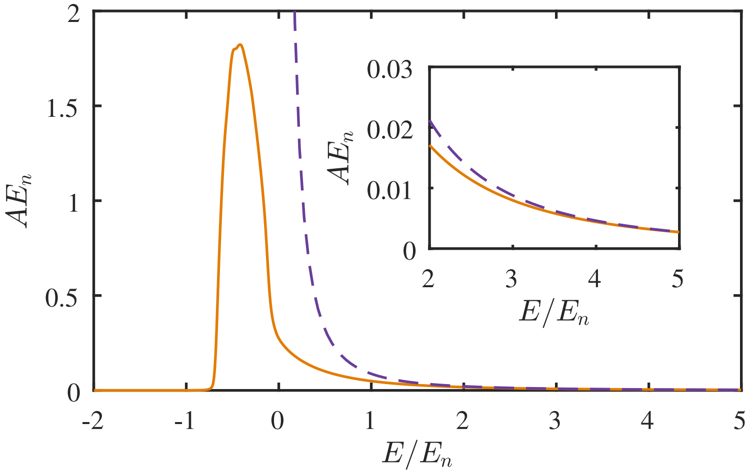

FIGURE 5.6: Comparison between the diagrammatically calculated spectral function and the high-energy limit for $1/k_n a = -0.76$. The diagrammatic result is shown as an orange solid line, and the high-energy limit is shown in dashed purple. The inset shows a zoom on the high energy tail, where the theories coincide. The figure is adopted from Ref. [163].

Here $\delta(x)$ is the Dirac delta function, $\Theta(\omega)$ is the Heaviside step function, $\hbar\omega_P$ is the polaron energy and Z is the quasiparticle residue. Equation (5.16) contains a delta-function at the polaron peak as well as a continuum of high-momentum impurity states and Bogoliubov excitations. In Fig. 5.6 the spectral function of Eq. (5.16) is compared to the high-energy limit of Eq. (5.13). Evidently, the diagrammatic results of Eq. (5.16) recovers the exact result of Eq. (5.13) in the limit of large ω, and furthermore describes the low-energy behaviour governed by polaron peak and the many-body continuum. By averaging Eq. (5.16) over the density distribution in the harmonic trap and performing a Fourier transformation, the coherence can thus be calculated at arbitrary times and interaction strengths, and compared to the experiment.

5.4.3 Dynamical Regimes

Since Eq. (5.16) describes the whole energy spectrum and therefore the full temporal evolution of the coherence, it can be used to extract the borderlines between the different regimes of impurity dynamics, being the strong and weak coupling dynamics contained in Eq. (5.15) and the many-body regime, respectively. The borderlines between the different regimes are shown in Fig. 5.7, where they are drawn as sharp lines even though the transitions are smooth. The borderlines in Fig. 5.7 can be extracted by considering the relevant parts of the second term in the spectral function Eq. (5.16)

$$m^{3/2}\omega^{5/2}\left[1+\frac{\hbar}{ma^2\omega}\left(1-\frac{E_{\mathrm{mf}}}{\hbar\omega}\right)^2\right] \tag{5.17}$$

where the second term of the parenthesis is written in terms of E_{mf}. In the limit of large ω the dynamical behaviour is governed by high-energy two-body scattering and the second term in the square brackets can be neglected. The spectral function thus goes as $\omega^{-5/2}$ resulting in the $t^{3/2}$ dynamics of Eq. (5.15). For lower energies, corresponding to longer times, the term becomes relevant as $\omega < \hbar/ma^2$ corresponding to $t > t_a$, which thus marks the crossover from strong coupling to weak coupling dynamics, where the spectral function goes as $\omega^{-3/2}$ resulting in $t^{1/2}$ dynamics. Finally, by considering the content of the inner parenthesis, the transition to many-body dynamics can be found to occur when $\omega > E_{\mathrm{mf}}/\hbar$ corresponding to $t > t_{\mathrm{mf}} = \hbar/E_{\mathrm{mf}}$.

The transition from weak coupling to many-body dynamics can only occur for interaction strengths where t_a remains the shortest timescale of the system. This ceases to be the case for strong interactions when $t_a = t_{\mathrm{mf}}$ or $E_{\mathrm{mf}} \geq \hbar^2/ma^2$ corresponding to $1/(k_n|a|) = (2/3\pi)^{1/3} \simeq 0.60$. Beyond this interaction strength, the many-body regime emerges directly from the strong coupling dynamics at the transition time $t_{\mathrm{mb}} = m/((16\pi^2)^{1/3}\hbar n_{\mathrm{B}}^{2/3}) \simeq 1.4t_n$, which can be found from the condition $1/(k_n|a|) \simeq 0.60$. Note that the borderlines in Fig. 5.7 assumes a homogeneous density and that they should not be understood as sharp boundaries, but as smooth transitions.

5.5 Experimental Sources of Decoherence

In addition to the decoherence caused by the dynamical scattering of impurities, there are three experimental sources of decoherence that influence

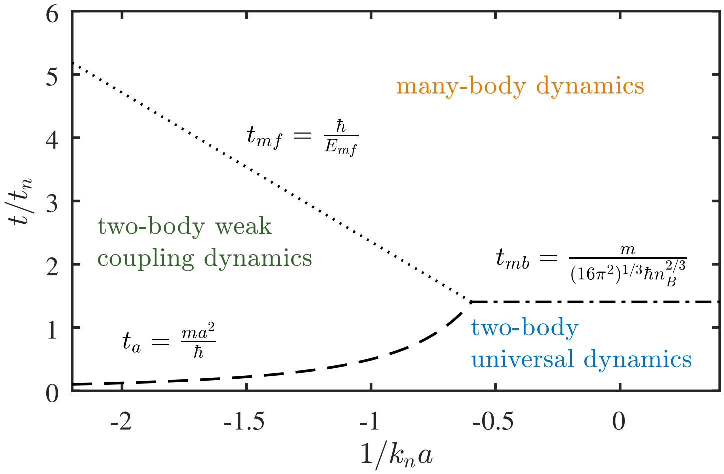

FIGURE 5.7: Dynamical regimes of impurity dynamics. The dashed line shows the transition from two-body universal to weak coupling dynamics, the dotted line shows the transition from weak coupling to many-body dynamics, and the dash-dotted line shows the two-body universal to many-body transition. A similar figure was shown in Ref. [51].

the interference signal, namely dephasing from the inhomogeneous density distribution of the harmonic trap, the finite lifetime of atoms in the impurity state, and shot-to-shot magnetic field fluctuations. These must all be taken into account in order to compare the theoretically predicted behaviour of the coherence to the experimental data.

Dephasing from Harmonic Trap

Within the harmonic potential provided by the ODT, the density distribution of the BEC follows the Thomas-Fermi profile described in Sec. 2.3. Consequently, the density dependent terms in the model for the coherence evolve differently across the trap with the fastest evolution in the central region. In the collective spin picture of Fig. 5.4, the state thus becomes broadened during the phase evolution between the two interferometry pulses. The density distribution can be included in the theoretical predictions for the coherence by performing a local density approximation as described in Sec. 5.3, which in the short-time limits of Eqs. (5.14) and (5.15) corresponds

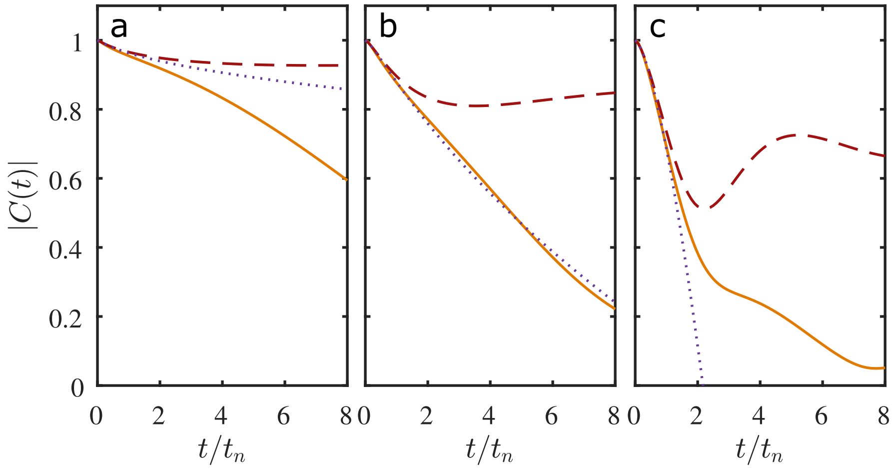

FIGURE 5.8: Influence of the harmonic trap potential on the coherence. The coherence amplitude is shown for (a) $1/k_n a = -2.0$, (b) $1/k_n a = -0.76$, and (c) $1/k_n a = 0.01$. The diagrammatic prediction of Eq. (5.16) is shown with and without trap dephasing in solid orange and dashed red, respectively. The general short-time prediction in Eq. (5.14) is shown in dotted purple. None of the other experimental decoherence mechanisms are included in the plot. A similar figure was shown in Ref. [51].

to replacing the density by its average value, since all terms are linear in density. The effect of the density distribution on the coherence is shown in Fig. 5.8, where the predicted coherence from the diagrammatic theory is shown with (solid orange) and without (dashed red) including the density distribution. When excluding the density distribution, the coherence decays slowly and for weak interactions it is predicted to settle at the quasiparticle residue Z [184]. For stronger interactions, the coherence can display oscillations due to interference between different parts of the spectral function. This has been observed for the Fermi polaron in experiments employing an approximately homogenous medium [44, 45]. For the experiments considered here, the additional decoherence from the density distribution averages out the oscillations, and eventually results in a complete loss of coherence preventing the extraction of Z.

Impurity Lifetime

In order to vary the strength of the impurity-medium interactions, the experiments are performed near a Feshbach resonance. As explained in Sec. 2.2.2, the three-body loss coefficient scales as a^4 and has an increasing influence on the experimental signal as the scattering length diverges when approaching the centre of the Feshbach resonance. The effect on the signal is a loss of contrast as impurity atoms are lost between the two pulses of the interferometry sequence. To measure the lifetime of the impurity atoms, the following method is employed: A BEC in the $|1\rangle$ state is prepareed under similar conditions to those of the interferometry experiments, and $10\,\%$ of the population is then transferred to the $|2\rangle$ state in order to initialize the loss measurement. The sample is then held for a variable time under which three-body recombination takes place, removing two medium atoms for every impurity atom. Subsequently, any remaining population in the $|2\rangle$ state is transferred to the $|F = 1, m_F = 1\rangle \equiv |3\rangle$ state, which undergoes rapid two-body spin changing collision with atoms in the $|1\rangle$ state. As a result, the atoms that are transferred to the $|3\rangle$ state are still lost, however, in this case only one atom in the $|1\rangle$ state is lost for each impurity atom. Finally the remaining number of atoms in the $|1\rangle$ state is determined by absorption imaging after TOF expansion. The experiment is repeated for different values of $1/k_n a$, and the loss rate Γ is extracted by performing an exponential fit $\sim \exp(-\Gamma t)$ to the remaining atom number. Figure 5.9 shows the extracted loss rate as a function of $1/k_n a$ together with an empirical fit $\beta_1 + \beta_2 \exp(\beta_3/k_n a)$, and the inset shows example loss measurements. As seen, the loss rate increases by an order of magnitude when approaching the resonance centre at $1/k_n a = 0$. Note, that in reality the loss coefficient reduces again on the positive side of the resonance, however, since the experiments are only performed using attractive interactions and at unitarity, the empirical fit is valid, and the losses are included in the theoretically predicted coherence as $C(t) \to C(t)\exp(-\Gamma t)$.

Magnetic Field Fluctuations

The third experimental decoherence mechanism comes from shot-to-shot fluctuations in the magnetic field, which introduces an additional varying detuning Δ between the rf pulse and the bare atomic transition. For each

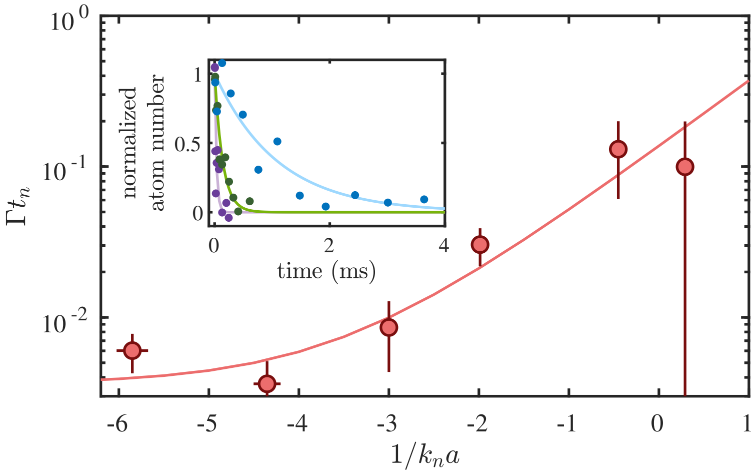

FIGURE 5.9: Loss rate of the impurity state under the employed experimental conditions. The measured loss rates are shown as a function of inverse interaction strength together with an empirical fit $\beta_1 + \beta_2 \exp(\beta_3/k_n a)$. Inset: Example loss measurements for $1/k_n a = -4.4$ (blue), $1/k_n a = -2.0$ (green,) and $1/k_n a = -0.45$ (purple). The atom numbers have been scaled with the initial and final atom numbers, and error bars have been omitted for clarity. A similar figure was shown in Ref. [51].

experimental sequence, this detuning results in an additional phase shift of $2\pi\Delta \cdot t$ which leads to decoherence when averaging multiple experimental runs. To include this effect, it is assumed that Δ follows a normal distribution $\exp\left(-\phi^2/2\sigma^2_{\text{noise}}(t)\right)/\sqrt{2\pi\sigma^2_{\text{noise}}(t)}$, where $\sigma_{\text{noise}}(t) = 2\pi\Delta_{\text{noise}}\, t$ and ϕ is the additional phase. Since the experimental data is collected over many experimental sequences, the magnetic field fluctuations are included in the coherence by integrating over the phase distribution

$$C(t) \rightarrow C(t)\frac{1}{\sqrt{2\pi\sigma^2_{\text{noise}}(t)}}\int_{-\infty}^{\infty} \mathrm{d}\phi\, \exp(-i\phi)\exp\left(-\phi^2/2\sigma^2_{\text{noise}}(t)\right). \quad (5.18)$$

The magnitude of Δ_{noise} is obtained by performing the interferometric measurement at $1/k_n a = -4.8$, where interactions are sufficiently weak that decoherence from higher-order impurity dynamics can be neglected. Instead

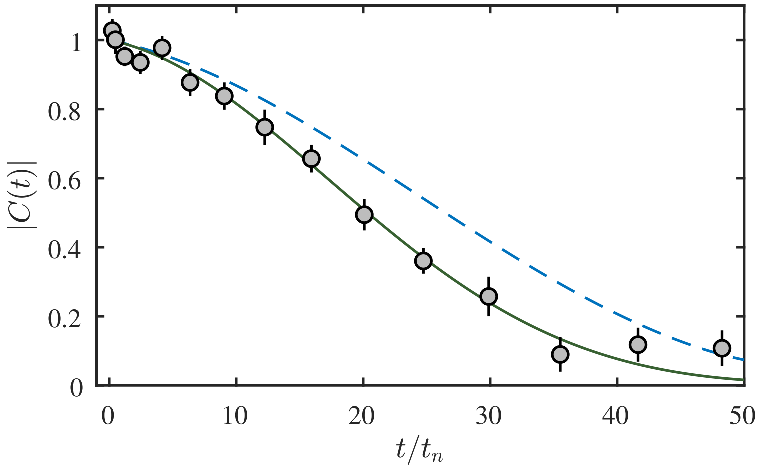

Figure 5.10: Decoherence due to shot-to-shot fluctuations in the magnetic field. The measured coherence amplitude is shown for $1/k_n a = -4.8$. The mean-field coherence amplitude including the effects of the finite impurity lifetime and inhomogeneous density distribution is shown in dashed blue. A fit of Eq. (5.18) to the data is shown in solid green and is used to determine the additional detuning originating from shot-to-shot fluctuations of the magnetic field. A similar figure was shown in Ref. [51].

the temporal evolution of the coherence is given by the mean-field energy distributed over the harmonic trap $\int d^3r \, \exp(-iE_{\mathrm{mf}}(r)t/\hbar)n(r)$, the impurity lifetime, and the shot-to-shot magnetic field fluctuations. The observed coherence amplitude is shown in Fig. 5.10 together with the mean-field decoherence (dashed blue) and a fit of Eq. (5.18) with Δ_{noise} as a fitting parameter (solid green). The extracted detuning is given by $\Delta_{\mathrm{noise}} = 1.4(1)\,\mathrm{kHz}$ which corresponds to $\sim 3\,\mathrm{mG}$ (the relative Zeeman splitting between the $|1\rangle$ and $|2\rangle$ states is $0.5\,\mathrm{kHz/mG}$ at the relevant magnetic fields). In practice, decoherence from shot-to-shot fluctuations in the magnetic field primarily affects experiments at weak interaction strengths, since for strong interactions the impurity lifetime is the primary experimental decoherence source.

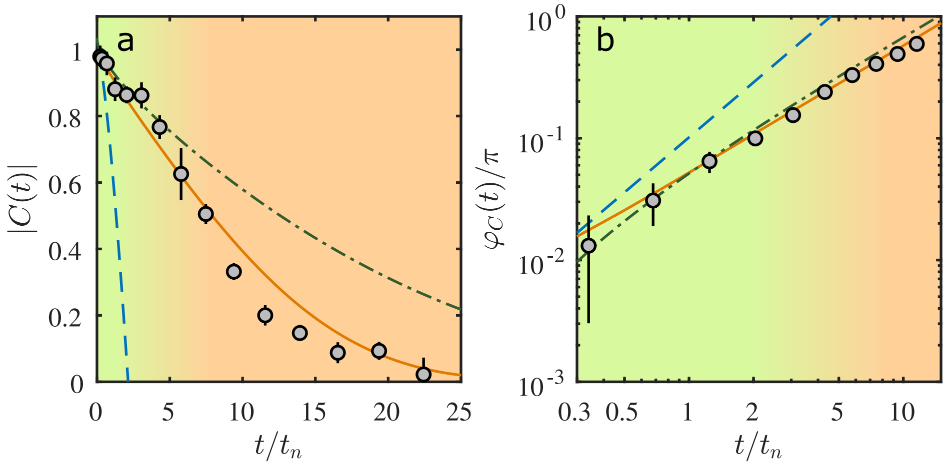

FIGURE 5.11: Impurity dynamics for weak interactions. The measured coherence amplitude (a) and phase (b) are shown for $1/k_n a = -1.8$. The diagrammatic prediction is shown in solid orange, and the two-body universal and weak coupling limits are shown in dashed blue and dash-dotted green, respectively. The smooth transitions between the two-body weak coupling (green), and many-body regimes (orange) is indicated by the colour gradient. A similar figure was shown in Ref. [51].

5.6 Experimental Results

With models for the experimental decoherence sources, the data can now be compared to the theoretical predictions for the coherence. The experiment is performed at different values of $1/k_n a$ ranging from weakly attractive to unitary interactions, and experimental values for the coherence amplitude and phase are extracted from fits of Eq. (5.1) to the interferometry signal, which yields the amplitude of the Ramsey signal $\mathcal{A}(t)$ and the coherence phase $\varphi_C(t)$. As explained in Sec. 5.3, the normalized coherence amplitude can then be determined as $|C(t)| = |\mathcal{A}(t)/\mathcal{A}(0)|$. For each data set, $\mathcal{A}(0)$ is determined from a fit of the general short-time prediction (Eq. (5.14)) with an overall amplitude to the data within t_n. The theoretical predictions for the coherence amplitude all include the experimental decoherence effects described in Sec. 5.5.

Experimental results for weak interactions ($1/k_n a = -1.8$) are shown in Fig. 5.11 with the coherence amplitude and phase in panels (a) and (b), respectively. The phase data is shown for a shorter time than the amplitude, since the extracted phase becomes unreliable for longer evolution times. The experimental data is compared to the theoretical short-time limits of Eq. (5.15) with the two-body universal and weak coupling limits shown in dashed blue and dash-dotted green, respectively. The diagrammatic prediction is shown in solid orange, and the transition from weak coupling (green) to many body dynamics (orange) is indicated by the colour gradient. For the weak interactions considered here, the transition time from two-body universal dynamics $t_a = 0.2t_n$ is so short that it is unobservable within the experimental resolution. As a consequence, both the amplitude and phase data immediately follows the $t^{1/2}$ evolution of the two-body weak coupling regime until $t \sim t_{\mathrm{mf}}$, where it deviates from the two-body prediction. From here the data continues to agree with the diagrammatic theory, which includes many-body dynamics, across the investigated range. The dynamical evolution of the impurity coherence thus shows how the system is initially governed by two-body collisions before entering a regime where a many-body description is necessary.

Figure 5.12 shows the experimental results for an intermediate interaction strength of $1/k_n a = -0.67$ together with the two-body universal coupling and diagrammatic predictions, following the same line styles as Fig. 5.11. The $t^{1/2}$ behaviour of the two-body weak coupling is not observable since $t \gg t_a$ is not reached before the smooth transition to many-body dynamics and it is therefore not shown. The coherence amplitude is shown for the full data range in panel (a) and panel (b) provides a zoom of the initial data for the time span where the phase (panel (c)) can be reliably extracted. Here the two-body universal regime is within the data resolution and is indicated by the blue colouring. For this interaction strength, the data initially follows the two-body universal $t^{3/2}$ behaviour before transitioning into the many-body regime at $t \sim t_{\mathrm{mf}}$. The data again shows good agreement with the diagrammatic prediction for all evolution times.

In Fig. 5.13(a), the evolution of the coherence is shown for unitary interactions ($1/k_n a = 0.01$) with the coherence phase shown in the inset. For this interaction strength, the many-body dynamics emerge directly from the two-body universal coupling regime, and the theoretical predictions are therefore only shown for these cases. The line styles and colour gradients have the same meanings as for the previous cases. For the coherence amplitude, the

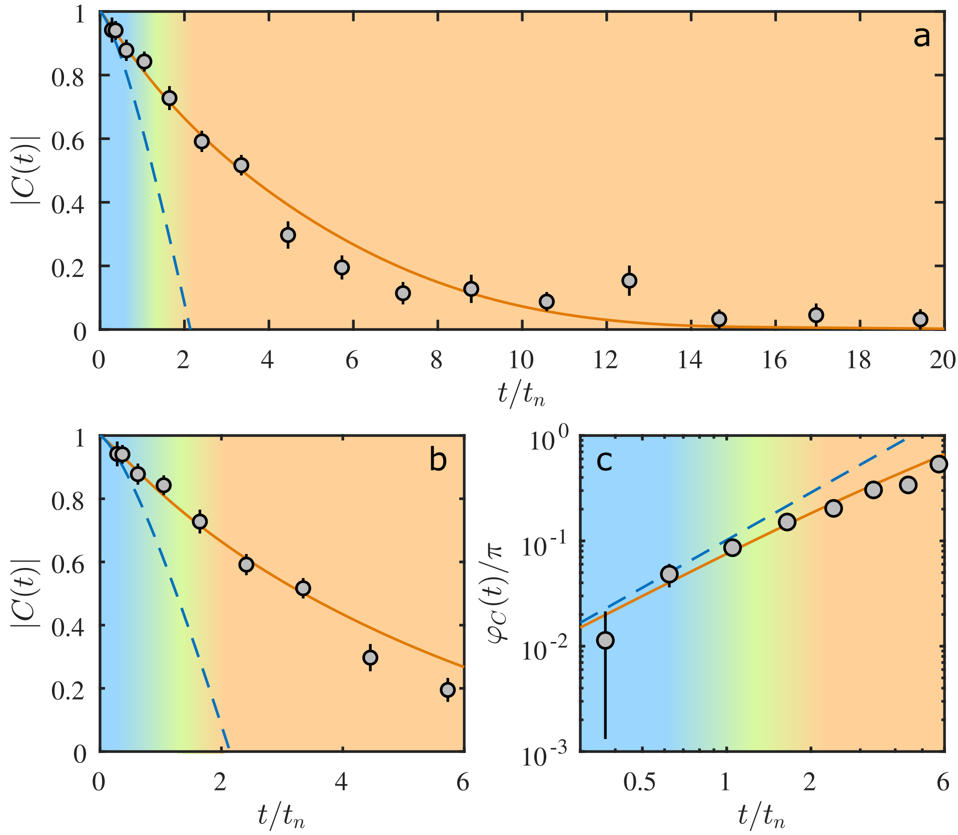

Figure 5.12: Impurity dynamics for intermediate interaction strength. The measured coherence amplitude (a-b) and phase (c) are shown for $1/k_n a = -0.67$. Panel (a) shows the coherence amplitude for the full data range, and panel (b) provides a zoom of the initial data corresponding to the range where the extraction of the phase is reliable. The diagrammatic prediction is shown in solid orange, and the two-body universal limit is shown in dashed blue. The smooth transitions between the two-body universal (blue), two-body weak coupling (green), and many-body regimes (orange) are indicated by the colour gradients. A similar figure was shown in Ref. [51].

data initially follows the two-body universal prediction very well before deviating and connecting with the diagrammatic many-body prediction at longer times. For the coherence phase, the data shows excellent agreement with both theoretical predictions within the duration where the phase can be reliably extracted.

For long times the phase evolution $\varphi_{\mathrm{C}}(t) \to -E_{\mathrm{p}} t/\hbar$ is governed by the polaron energy E_{p}. By differentiating the phase evolution to obtain the instantaneous energy $E(t) = -\hbar \mathrm{d}\varphi_{\mathrm{C}}/\mathrm{d}t$, the dynamical emergence of the polaron can therefore be observed. In Fig. 5.13(b), the instantaneous energy is shown for unitarity interactions, where the experimental values have been determined by piecewise linear fitting to the data. The instantaneous energy extracted from the phase evolution of the diagrammatic prediction and the equilibrated polaron energy [138] are shown in solid and dashed lines, respectively. The data again follows the theoretical prediction well and the measurement thus show the dynamical emergence of the Bose polaron as the system equilibrates.

5.6.1 Dynamical Regimes

The dynamical evolution of the impurity coherence is governed by the underlying collision processes as explained in Sec. 5.4.3, where the transition times between the different regimes were determined by investigating the spectral function (Eq. (5.16)). Here, these transition times are determined experimentally by comparing the measured coherence amplitude to the theoretical predictions.

The two-body universal to two-body weak coupling transition is given by t_a, which enters in the general prediction for the short-time behaviour of the coherence in Eq. (5.14). In order to extract t_a, a simultaneous fit of Eq. (5.14) to the initial coherence amplitude and phase data is therefore performed. Since the interferometry pulses have duration $0.5\,\mu\mathrm{s} \sim 0.1 t_n$, it is not immediately clear that t_a which is on the same order of magnitude can be extracted from the data. The specific value of t_a however affects the functional shape of the coherence amplitude and phase for times much longer than itself, and it can thus be extracted as explained in detail in Ref. [52].

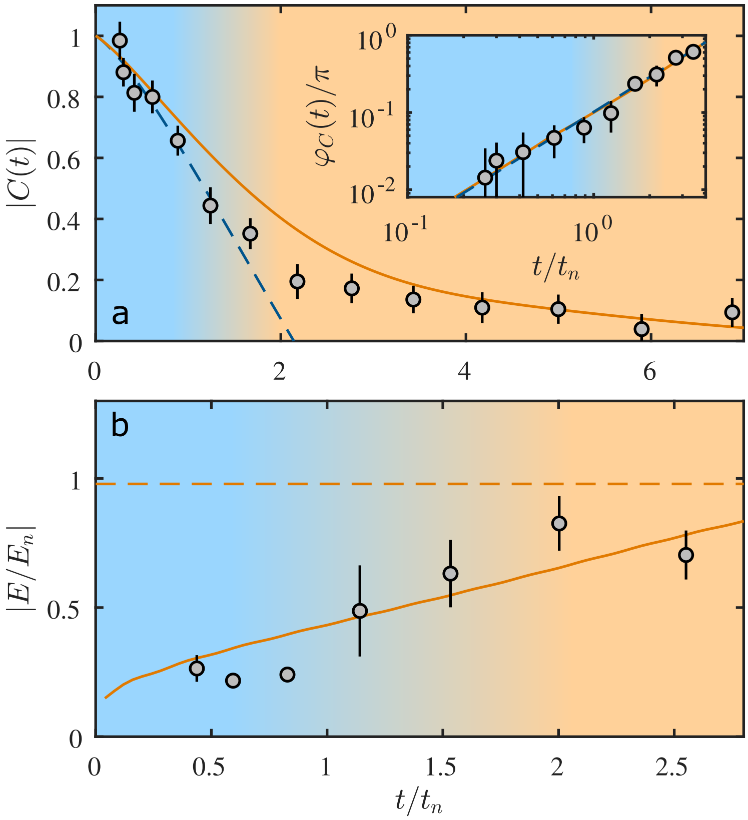

FIGURE 5.13: Impurity dynamics at unitary interactions, $1/k_n a = 0.01$. (a) Measured coherence amplitude and phase (inset). The diagrammatic prediction is shown in solid orange, and the two-body universal limit is shown in dashed blue. (b) Instantaneous energy obtained from the time derivative of the coherence phase. The diagrammatic prediction is shown in solid orange and the equilibrium polaron energy is shown in dashed orange [138]. The smooth transition between the two-body universal coupling and many-body regimes is indicated by the colour gradient. A similar figure was shown in Ref. [51].

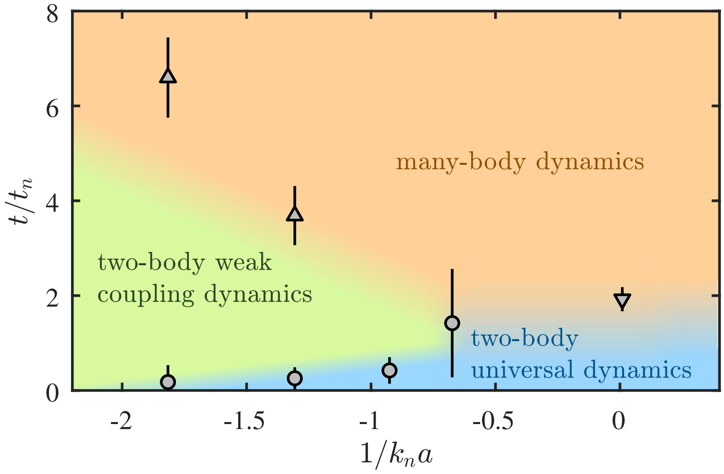

FIGURE 5.14: Transition times between the dynamical regimes of impurity dynamics as a function of the inverse interaction strength $1/k_n a$. The theoretically predicted regimes are shown using different background colours, and the smooth transitions between them are are indicated by the gradients. The fitted values of of the two-body universal to two-body weak coupling transition time t_a are shown as circles, and the experimental transition times from the two-body weak coupling and two-body universal regimes to many-body dynamics are shown as a upwards and downwards pointing triangles, respectively. A similar figure was shown in Ref. [51].

For the transition to many-body dynamics, no simple expression is available which can be used to determine the transition time, and a simple comparison between the experimentally measured coherence amplitude and the theoretical prediction is therefore performed: The data point at the shortest time, which is more than two standard errors away from the general short-time prediction Eq. (5.14) is identified and the time halfway between this and the previous data point then gives the experimental value for the onset of many-body dynamics, with the error given by the data resolution.

This method works in the limits of weak and strong interactions, however, for intermediate interaction strengths dephasing from the inhomogeneous density distribution causes the diagrammatic result to coincide with the short-time prediction for longer times as shown in Fig. 5.8(b), and no clear transition can be identified.

The dynamical regimes are shown in Fig. 5.14, where the theoretical transition times determined for a homogenous system are shown by the colour gradients, indicating that the transitions are smooth. The experimentally determined values of t_a are shown as circles, and the experimental transitions from two-body weak coupling and universal dynamics to the many-body regime, are shown as upwards and downwards pointing triangles, respectively.

The experimental values for t_a increase with stronger interactions showing excellent agreement with the theoretically predicted transition time. This highlights how the short-time behaviour of the coherence is determined by the average density as explained in Sec. 5.5, since the theoretical transition time is determined for a homogenous system.

For the many-body transitions, good agreement with the theoretical transition time is found for unitary and intermediate interaction strengths, whereas for weak interactions, the agreement is qualitative. Note, however, that the employed method for extracting the many-body transitions relies heavily on the quality of single data points. Moreover, for longer times the density must be included by integrating over the its distribution, making the comparison to the homogenous system less applicable. Together, the extracted transition times nonetheless grant a complete picture of impurity dynamics, showing how the system evolves from a regime governed by few-body processes to one with emerging many-body correlations, which signal the onset of polaron formation.

5.7 Summary and Outlook

In this chapter, the dynamical evolution of impurities in a BEC was investigated using an interferometric method. The experiments yielded measurements of the impurity coherence and enabled tracking the evolution of the system from a coherent superposition state into polaronic quasiparticles.

Three distinct regime of impurity dynamics were identified theoretically and measured experimentally from weakly attractive to unitary interactions. At short times, a universal $t^{3/2}$ decay of the coherence was observed, originating in high-energy two-body scattering independent of the coupling strength between the impurities and the bosonic medium. For weak interactions, an intermediate dynamical regime was identified with the coherence displaying a $t^{1/2}$ decay originating in low-energy two-body collisions, before transitioning into a regime governed by many-body physics. For strong interactions, the many-body dynamics was found to emerge directly from the two-body universal coupling regime. Across the investigated interaction strengths, good agreement was found between the experimental results and theoretical predictions, which shows that the polaron phenomenon is well-understood in the time domain. Together with the spectroscopic measurements in the frequency domain [48–50], the results presented here contribute to a combined description of the polaron.

The method employed here enables investigation of bosonic analogues to Anderson's orthogonality catastrophy [193] and transport processes [194, 195] in the time domain. Similar experiments performed at repulsive interactions will be able to explore the combined effect of the two polaron branches, and to investigate the multi-phonon bound states predicted for repulsive interactions [183]. By increasing the population in the impurity state, effective interactions between polarons could be investigated, which are predicted to influence the transport properties in condensed matter systems [171]. Additionally, an increased impurity concentration could allow for the spectroscopic observation of bipolarons, which are bound states of two polarons [196]. Furthermore, the polaron energy at unitarity has been predicted to be a universal function of $|a_-|n^{1/3}$, where a_- is the scattering length at which the first Efimov trimer appears [197], and this dependence could be observed by spectroscopic measurements at unitarity with varying density.

Currently, both interferometric and spectroscopic experiments are complicated by the inhomogeneous density distribution due to the harmonic trapping potential. In interferometric measurements, the inhomogeneous density contributes with an additional dephasing mechanism, while spectroscopic signal are broadened due to the density dependence of the polaron energy. Both types of experiments could thus be improved by performing them in a so-called box trap, where a uniform density distribution can be realized [198]. Initial considerations for realizing such a trap can be found in Ch. 8.

Chapter 6

Lee-Huang-Yang Fluid

In many contexts, mean-field theory as exemplified by the GP equation (Eq. (2.36)) provides a very good description of BECs. For large interaction strengths one must, however, go beyond the mean-field picture of interactions in order to accurately describe the system. The first beyond-mean-field correction to the energy of a Bose gas is the LHY correction which includes the zero-point energy of the Bogoliubov modes presented in Sec. 2.4.3. In most cases, it results in a small correction to the dominant mean-field energy, however, recently there has been great scientific interest in systems where beyond-mean-field effects have a large influence. A striking example is the LHY fluid proposed by our research group in 2018 [53], where by tuning the atom numbers and scattering lengths of a Bose-Bose mixture, one can realize a system where the interactions are *entirely* governed by quantum fluctuations. In this chapter, the experimental realization of the LHY fluid is presented, which was published as Editor's Suggestion in Physical Review Letters [54].

Prior to this work, the influence of the LHY correction has been observed experimentally using several methods. The first observation used fermionic ^{6}Li, where on the BEC side of the BEC-BCS crossover an up-shift of the collective oscillation frequencies was measured in agreement with quantum Monte Carlo simulations [164]. Following this, the LHY correction has been observed in measurements of the equation of state for ^{6}Li [41, 199] and

^{7}Li [200], and in Bragg spectroscopy measurements of ^{85}Rb near a Feshbach resonance [201]. In 2015, the LHY correction became a hot research topic based on the proposal of Petrov [56], who showed that the repulsive energy contribution from the LHY correction can be used to stabilize a quantum mixture, which would otherwise collapse under attractive mean-field forces. The resulting quantum droplets were subsequently observed experimentally in both homo- [57–60] and heteronuclear [61] bosonic mixtures. Simultaneously, the LHY correction was also employed in the context of dipolar quantum gases, where tuning the relative strengths of contact interactions, dipole-dipole interactions, and quantum fluctuations lead to the formation of dipolar quantum droplets [62–65]. More recently, this has culminated in the observation of supersolid behaviour in these systems [66–68].

The chapter is structured as follows: First, the theoretical description of a LHY fluid is presented in Sec. 6.1 based on Ref. [53]. Sec. 6.2 then describes the experimental method used for realizing a LHY fluid in ^{39}K. Following this, the numerical simulations used to model the experimental system are described in Sec. 6.3. Finally, in Sec. 6.4 the experimental results are compared to simulations, and in Sec. 6.5 an outlook is given.

Within the work of this chapter, I have been involved in all aspects besides the theoretical description in Sec. 6.1, which was developed by Nils B. Jørgensen. The experiments were designed and conducted in cooperation with the rest of the research group, while the simulations and data analysis were performed by me.

6.1 Theoretical Description of a LHY Fluid

The starting point for the theoretical description of a LHY fluid is a two-component BEC at zero temperature. Excluding the LHY correction, it is described by the mean-field energy functional

$$E_{\mathrm{MF}} = \int d\mathbf{r} \left(\sum_i \left[\frac{\hbar^2 |\nabla \psi_i|^2}{2m_i} + V_i n_i \right] + \frac{1}{2} \sum_{ij} g_{ij} n_i n_j \right), \tag{6.1}$$

where $\psi_i(\mathbf{r}) = \sqrt{N_i}\phi(\mathbf{r})$ is the condensate wave function with atom number N_i and single-particle wave function $\phi_i(\mathbf{r})$, and $n_i(\mathbf{r}) = |\psi_i(\mathbf{r})|^2$ is the density of component i. Furthermore, the coupling strengths $g_{ij} = 2\pi\hbar^2 a_{ij}/m_{ij}$ are the same as in Sec. 2.3.4, the two components have equal masses $m = m_1 = m_2$, and the external potential is a spherically symmetric harmonic oscillator, $V_i(\mathbf{r}) = V_1(\mathbf{r}) = V_2(\mathbf{r}) = m\omega_0^2 r^2/2$. For a specific choice of interaction strengths and relative densities $g_{12} = -\sqrt{g_{11}g_{22}}$, corresponding to $\delta a = a_{12} + \sqrt{a_{11}a_{22}} = 0$, and $n_2 = \sqrt{g_{11}/g_{22}}n_1$, all mean-field terms in Eq. (6.1) cancel and the system becomes non-interacting at the mean-field level. In this case, the interactions are governed by the next-order LHY correction. For a two-component Bose gas, it is given by [56, 202]

$$\frac{E_{\mathrm{LHY}}}{\mathcal{V}} = \frac{8}{15\pi^2} m_1^{3/2} (g_{11}n_1)^{5/2} f\left(\frac{m_2}{m_1}, \frac{g_{12}^2}{g_{11}g_{22}}, \frac{g_{22}n_2}{g_{11}n_1}\right), \tag{6.2}$$

where $f > 0$ is a dimensionless number. For the homonuclear case, f is given by [56]

$$f(1, x, y) = \frac{1}{4\sqrt{2}} \sum_{\pm} (1 + y \pm \sqrt{(1 - y^2) + 4xy})^{5/2}, \tag{6.3}$$

whereas for the heteronuclear case, an effective expression for Eq. (6.2) has been derived recently [203]. Using Eq. (6.3), the LHY energy functional Eq. (6.2) can be written in terms of the scattering lengths

$$\frac{E_{\mathrm{LHY}}}{\mathcal{V}} = \frac{32\sqrt{2\pi}}{15} \frac{\hbar^2}{m} \sum_{\pm} (a_{11}n_{11} + a_{22}n_2 \pm \kappa)^{5/2}, \tag{6.4}$$

where $\kappa = [(a_{11}n_1 - a_{22}n_2)^2 + 4a_{12}n_1n_2]^{1/2}$. For $\delta a = a_{12} + \sqrt{a_{11}a_{22}} = 0$ and $n_2 = \sqrt{g_{11}/g_{22}}n_1$ Eq. (6.2) thus becomes

$$\frac{E_{\mathrm{LHY}}}{\mathcal{V}} = \frac{256\sqrt{\pi}\hbar^2}{15m} (n|a_{12}|)^{5/2}, \tag{6.5}$$

where $n = n_1 + n_2$. Including this term in the energy functional and defining $|\psi|^2 = |\psi_1|^2 + |\psi_2|^2$ with $\psi_2 = \psi_1 (g_{11}/g_{22})^{1/4}$ then yields the single-component energy functional

$$E = \int \mathrm{d}\mathbf{r} \left[\frac{\hbar^2 |\nabla\psi|^2}{2m} + V|\psi|^2 + \frac{256\sqrt{\pi}\hbar^2}{15m} (|a_{12}|)^{5/2} |\psi|^5\right], \tag{6.6}$$

and this system is denoted a LHY fluid. The corresponding GP equation is

$$\mu\psi = \left[-\frac{\hbar^2}{2m}\nabla^2 + V(\mathbf{r}) + \frac{128\sqrt{\pi}\hbar^2}{3m}|a_{12}|^{5/2}|\psi|^3\right]\psi, \tag{6.7}$$

with the chemical potential μ. Equation (6.7) is analogous to Eq. (2.36) for a single-component BEC, but with a $|\psi|^3$ term instead of usual the $|\psi|^2$ term from mean-field interactions. The LHY fluid thus has promising applications in the context of quantum simulation, since it allows the simulation of systems with a quartic nonlinearity in the wave function. Similar to a single-component BEC, the strength of the LHY interaction can be characterised by the ratio of the interaction energy to the kinetic energy. For the LHY fluid, this is given by the dimensionless parameter $U = N^{3/2}|a_{12}/a_{\mathrm{ho}}|^{5/2}$, which is used to characterise the LHY interaction strength in the following sections.

6.1.1 Monopole Oscillation Frequency of a LHY Fluid

Measurements of collective excitations serve as a powerful probe of the underlying interactions in ultracold gases. Indeed, some of the first BEC experiments [204–207] confirmed the theoretical predictions [208–210] for the oscillation frequencies of a BEC in an asymmetric trap by employing a quick step in magnetic field gradient, modulating the curvature of the magnetic field, or shining in a far-detuned laser beam. Since then, collective excitation measurements have continued to find applications in the field of ultracold gases. In particular, they are sensitive to beyond mean-field effects as evident from the first measurement of the LHY correction [164], in the context of dipolar supersolids [211, 212], and as a probe of the three-body scattering hypervolume [71]. Thus, the monopole oscillation frequency can serve as a probe of the LHY interactions and can be used to confirm the realization of a LHY fluid.

By inserting a trial wave function into Eq. (6.6) and expanding the resulting effective potential around equilibrium, the monopole oscillation frequency of a LHY fluid can be determined to [53]

$$\omega_{\mathrm{LHY}} = \omega_0\left(4 + \frac{45}{8}\frac{E_{\mathrm{LHY}}}{E_{\mathrm{pot}}}\right)^{1/2}, \tag{6.8}$$

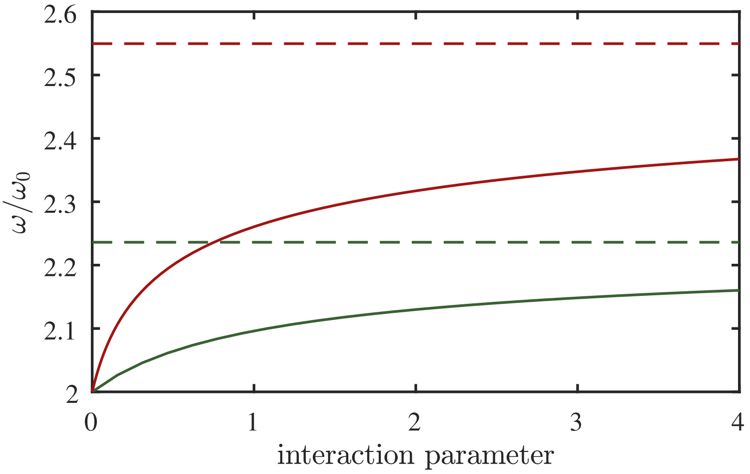

FIGURE 6.1: Comparison of the monopole oscillation frequencies of a LHY fluid (red) and a single-component BEC (green) in a spherically symmetric trap. The oscillation frequencies are shown as a function of the corresponding dimensionless parameters for the interaction strength ($N^{3/2}|a_{12}/a_{\mathrm{ho}}|^{5/2}$ for the LHY fluid and Na/a_{ho} for the BEC), and the Thomas-Fermi limits for both cases are shown as dashed lines.

where E_{LHY} and E_{pot} are obtained by evaluating the LHY and potential energy terms from Eq. (6.6). As seen from Eq. (6.8), the monopole frequency of the atomic cloud constitutes a direct probe of the LHY interaction energy. In the non-interacting limit, E_{LHY} can be neglected and Eq. (6.8) yields $\omega_{\text{non-int}}/\omega_0 = 2$, which is the usual result for non-interacting particles confined in a harmonic oscillator potential. In the Thomas-Fermi limit, where the LHY energy dominates the zero-point kinetic energy $\omega_{\mathrm{LHY,\,TF}}/\omega_0 = \sqrt{13/2} \simeq 2.55$. For comparison, applying the same method to a single-component BEC yields [12]

$$\omega_{\mathrm{BEC}} = \omega_0 \left(4 + \frac{3E_{\mathrm{MF}}}{2E_{\mathrm{pot}}}\right)^{1/2}, \tag{6.9}$$

which has the same non-interacting limit of $\omega_{\text{non-int}}/\omega_0 = 2$ as the LHY fluid, but a lower frequency in the strongly interacting limit $\omega_{\mathrm{BEC,\,TF}}/\omega_0 = \sqrt{5} \simeq 2.24$. The monopole frequency of the LHY fluid thus experiences a bigger shift for increasing interactions than a single-component BEC. In Fig. 6.1, the monopole oscillation frequencies of a LHY fluid and a single-component BEC are shown as a function of their respective dimensionless parameters for the interaction strength. The monopole frequency of the system can thus serve as a probe of the LHY interactions.

6.2 Experimental Method

In order to realize a LHY fluid experimentally, the two employed states must feature a favourable Feshbach resonance structure for realizing $\delta a = 0$. This is the case for the $|F = 1, m_F = -1\rangle \equiv |1\rangle$ and $|F = 1, m_F = 0\rangle \equiv |2\rangle$ states of ^{39}K, which were also used in experiments on homonuclear quantum droplets [57–60] and in the polaron experiments of Ch. 5. The Feshbach resonance structure for the two states is shown in Fig. 6.2 with the scattering lengths for collisions between atoms in state $|1\rangle$ shown in red, between atoms in state $|2\rangle$ shown in green, and the scattering length between the two states shown in dashed blue.

Based on models for the Feshbach resonances presented in Refs. [59, 84, 86] the system is found to fulfil $\delta a = 0.0(3)\, a_0$ at 56.83 G with $a_{11} = 33.3(3)\, a_0$, $a_{22} = 84.2(3)\, a_0$, and $a_{12} = -52.97(1)\, a_0$. This magnetic field is shown as a dotted black line in Fig. 6.2, and with these scattering lengths, the requirement for the relative densities is $n_2/n_1 = 0.629(3)$ corresponding to 40 % of the total atom number in state $|2\rangle$.

The experiment starts from an almost pure BEC in the $|1\rangle$ state prepared at a homogeneous magnetic field of 39.6 G in an ODT composed of beams along the two horizontal axes as described in Ch. 4. From here, the magnetic field is linearly ramped to the target field in the vicinity of $\delta a = 0$ over 10 ms. Following the magnetic field ramp, the vertical ODT beam is turned on and the three ODT beam intensities are linearly ramped over 0.3 seconds to the desired intensities for realizing a symmetric trapping potential. Subsequently, a rf pulse of variable duration tuned to the bare atomic transition transfers part of the atoms to the $|2\rangle$ state, thus realizing the desired atom number ratio. Due to the sudden change in interaction strengths resulting from the rf transfer, the system starts to contract and strong monopole oscillations are initialized directly by the preparation method. A schematic representation of

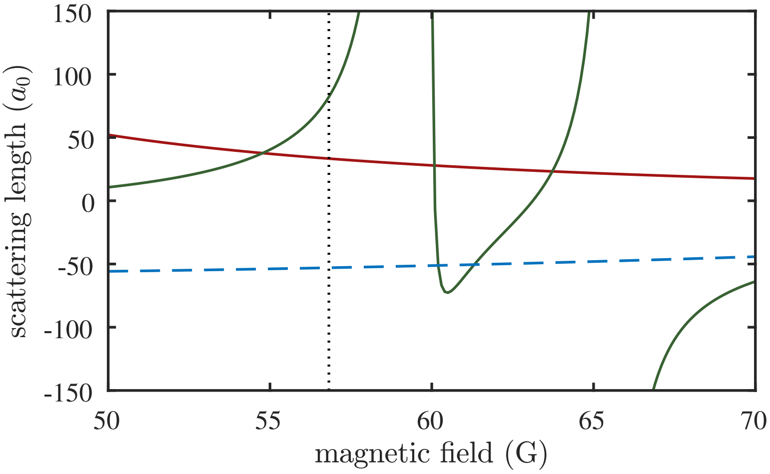

FIGURE 6.2: Feshbach resonance structure in the vicinity of $\delta a = 0$. The scattering lengths for collision between atoms in state $|1\rangle$ is shown in red [84], between atoms in state $|2\rangle$ is shown in green, and the scattering length between the two states is shown in dashed blue [86]. The magnetic field where $\delta a = 0$ is shown as a dotted black line. The green curve for collisions between atoms in state $|2\rangle$ is provided by the group of S. Kokkelmans and is based on the K–K potentials of Ref. [213].

the experiment is shown in Fig. 6.3(a) which displays a LHY fluid undergoing monopole oscillations in an ODT composed of three beams.

After the transfer, the system is held for a variable hold time before being released from the trap. During 28 ms of TOF expansion, a magnetic field gradient of 3 ms duration is applied to separate the two states before absorption imaging, as shown in the typical absorption image displayed in Fig. 6.3(b).

The two clouds are analysed separately and the cloud radii along the y- and z-directions are extracted by fitting a Thomas-Fermi profile to the images for each evolution time. Figure 6.3 shows a typical measurement at $\delta a = 0$, where the atom number ratio was tuned to the required value for LHY fluid. The radii along the y- and z-directions after 28 ms of TOF are shown as blue dots and red triangles, respectively, and the grey lines are fits of a model function to the mean radius. The evolution of the $|1\rangle$ and $|2\rangle$ states are shown in panels (a) and (b), respectively. The temporal evolution in the

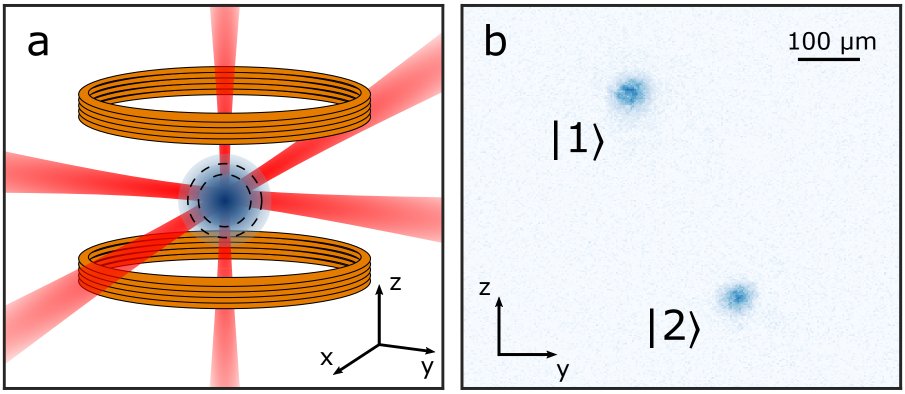

FIGURE 6.3: (a) Schematic representation of the experiment showing a LHY fluid undergoing monopole oscillations in a spherical potential composed of three red-detuned laser beams. (b) Typical absorption image after time-of-flight expansion during which atoms in states $|1\rangle$ and $|2\rangle$ are separated by a magnetic field gradient. A similar figure was published in Ref. [54].

radii feature large amplitude oscillations due to the experimental preparation method. For both states, the different radii oscillate in phase confirming that the oscillations are monopolar. Furthermore, the two states initially oscillate jointly, however with increasing time, inelastic losses in the $|2\rangle$ state [57–60] result in a small phase difference and a deviation from regular sinusoidal behaviour.

6.3 Numerical Simulations

Since the system is initialized out of equilibrium and features large amplitude oscillations and inelastic losses, a direct comparison to the theoretical prediction of Sec. 6.1 is not possible. In particular, the asymmetric inelastic losses result in a deviation from the ideal density ratio for a LHY fluid, which render the single-component framework of Eq. (6.7) invalid with increasing evolution time. In order to model the experiment, detailed simulations of the full two-component system including the LHY contributions and inelastic losses are therefore performed using extended GP equations. These can be

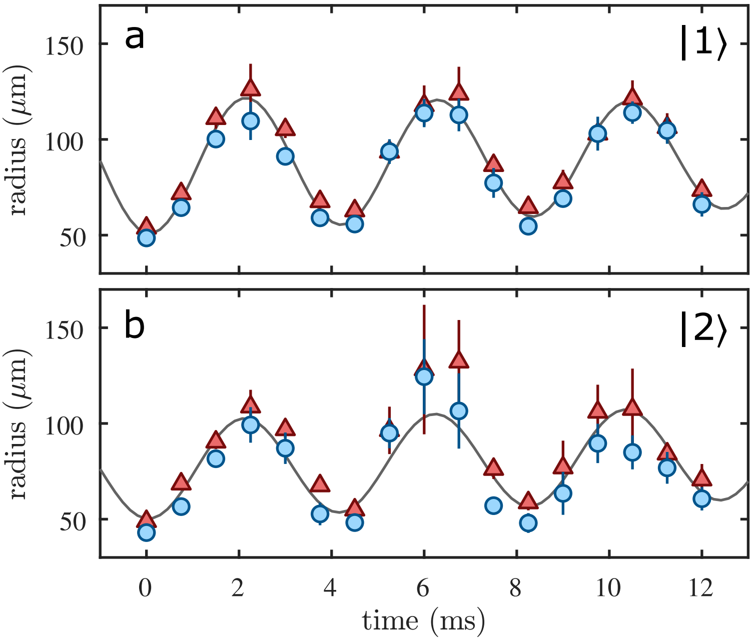

FIGURE 6.4: Extracted BEC radii of atoms in states $|1\rangle$ (a) and $|2\rangle$ (b) after 28 ms time of flight as a function of evolution time. The radii along the y- and z-directions are shown as blue circles and red triangles, respectively, and the grey lines are fits of Eq. (6.15) to the mean radius. The data was recorded for $\omega_0 = 2\pi \times 113.1(6)$ Hz and $N = 2.3(3) \times 10^4$ corresponding to $U = 0.5(1)$. A similar figure was published in Ref. [54].

written as

$$\mu_i \psi_i = \left(-\frac{\hbar^2}{2m_i} \nabla^2 + V + \mu_{\mathrm{MF}}^{(i)} + \mu_{\mathrm{LHY}}^{(i)} \right) \psi_i, \tag{6.10}$$

where μ_i is the chemical potential, $V(\mathbf{r}) = m\omega_0^2 \mathbf{r}^2/2$ is the spherically symmetric potential, and contributions from both mean-field interactions $\mu_{\mathrm{MF}}^{(i)}$ and quantum fluctuations $\mu_{\mathrm{LHY}}^{(i)}$ are included. For equal masses, the mean-field contributions are given by

$$\mu_{\mathrm{MF}}^{(i)} = \frac{4\pi\hbar^2}{m} \left(a_{ii} n_i + a_{ij} n_j \right), \tag{6.11}$$

and based on Eq. (6.4), the contribution from quantum fluctuations can be written as

$$\mu_{\mathrm{LHY}}^{(i)} = \frac{16\sqrt{2\pi}}{3}\frac{\hbar^2}{m}\sum_{\pm}\left[\left(a_{ii} \pm \frac{a_{ii}^2 n_i - a_{ii}a_{jj}n_j + 2a_{ij}^2 n_j}{\sqrt{(a_{ii}n_i - a_{jj}n_j)^2 + 4a_{ij}^2 n_i n_j}}\right)\right.$$
$$\left.\times\left(a_{ii}n_i + a_{jj}n_j \pm \sqrt{(a_{ii}n_i - a_{jj}n_j)^2 + 4a_{ij}^2 n_i n_j}\right)^{3/2}\right],$$

where the chemical potentials have been determined via the usual relation $\mu_i = \partial E/\partial N_i$. Note that for cases where $\delta a < 0$, $\mu_{\mathrm{LHY}}^{(i)}$ acquires a small imaginary component, however, as pointed out in Ref. [56], the LHY energy is insensitive to small variations in δa, and in particular its sign. This has justified setting $\delta a = 0$ explicitly in previous work on self-bound droplets [56, 58, 214]. Here, only the real part of $\mu_{\mathrm{LHY}}^{(i)}$ is included in the numerical simulations. Note that a consistent theory which avoids this issue was recently developed [215].

To include inelastic losses in the dynamical simulations, empirical loss terms are added to the right hand side of the time-dependent generalization of Eq. (6.10) as described in Sec. 2.3.3 and previously employed in Refs. [58, 60, 61, 97]. For each component i the loss terms take the form

$$-\frac{i\hbar}{2}\left(K_{iii}|\psi_i|^4 + \frac{2}{3}K_{iij}|\psi_i|^2|\psi_j|^2 + \frac{1}{3}K_{ijj}|\psi_j|^4\right)\psi_i, \tag{6.12}$$

where, K_{ijk} denotes the three-body loss coefficients and the factors in front of each term take into account how many atoms are lost by the given loss process. The three-body loss coefficients are given by

$$K_{iii} = \frac{1}{3!}K_{iii}^{\mathrm{th}}\left[1 + \frac{6}{n_i^2}\frac{\partial(E_{\mathrm{LHY}}/\mathcal{V})}{\partial g_{ii}}\right], \tag{6.13}$$

and

$$K_{iij} = \frac{1}{2!}K_{iij}^{\mathrm{th}}\left[1 + \frac{2}{n_i^2}\frac{\partial(E_{\mathrm{LHY}}/\mathcal{V})}{\partial g_{ii}} + \frac{2}{n_i n_j}\frac{\partial(E_{\mathrm{LHY}}/\mathcal{V})}{\partial g_{ij}}\right], \tag{6.14}$$

where K_{ijk}^{th} denote the thermal three-body loss coefficients, the factors $1/2!$ and $1/3!$ are due to the indistinguishability of bosonic atoms [98, 99], and the terms involving the energy density $E_{\mathrm{LHY}}/\mathcal{V}$ given in Eq. (6.4) include beyond mean-field corrections to the three-body correlation functions of the mixture [59].

6.3.1 Modelling the Experiment

Based on the equations describing the physical system given above, the experimental procedure can be modelled, which is done using the two-component framework of the numerical toolbox GPELab [101, 102]. The system is described as two interacting BECs and thermal atoms are therefore neglected in the analysis. As evident from Fig. 6.4, the dynamics of the system occurs on a millisecond time scale, and since the experiment is initialized by a rf pulse of microsecond duration, the transfer is modelled as follows: First the ground state of a ^{39}K BEC of $N_1 = N$ atoms in the $|1\rangle$ state is calculated using the single-component GP equation (Eq. (2.36)) extended to include the LHY correction (Eq. (2.57)). The BEC is confined in a the spherical trap potential and the scattering length $a_{11}(B)$ is chosen to correspond to the experimental value set by the magnetic field B. Subsequently, the mixture is initialized by copying the calculated wave function and adjusting the atom numbers N_1 and N_2 to the desired ratio. Since the wave function of state $|2\rangle$ is copied from the calculated wave function of state $|1\rangle$, adjusting the relative atom numbers directly translates into the density ratio. The scattering lengths a_{12} and a_{22} are likewise chosen according to the magnetic field. Note that this model for the transfer assumes that the initially created superposition state decoheres fast enough that it can be considered a mixture from the beginning. The dynamical evolution of the two wave functions is then calculated using the extended GP equations described above. The loss coefficients involving atoms in the $|1\rangle$ state have previously been measured to be compatible with the ^{39}K background value of $7.74 \times 10^{-29}\,\mathrm{cm^6 s^{-1}}$ [59, 89, 216], and this value is therefore used for K_{111}^{th}, K_{112}^{th}, and K_{122}^{th}. The loss coefficient for the channel involving three $|2\rangle$ atoms is set to $K_{222}^{\mathrm{th}} = 5.4 \times 10^{-27}\,\mathrm{cm^6 s^{-1}}$ based on Ref. [58], which is compatible with measurements in Ref. [59].

Similar to the experiment, the system is initialized out of equilibrium and the wave functions evolve dynamically as a response to the transfer without any adjustment of the confining potential. Figure 6.5 shows results of the dynamical two-component simulations for $\delta a = 0$ and $n_2/n_1 = \sqrt{a_{11}/a_{22}}$ such

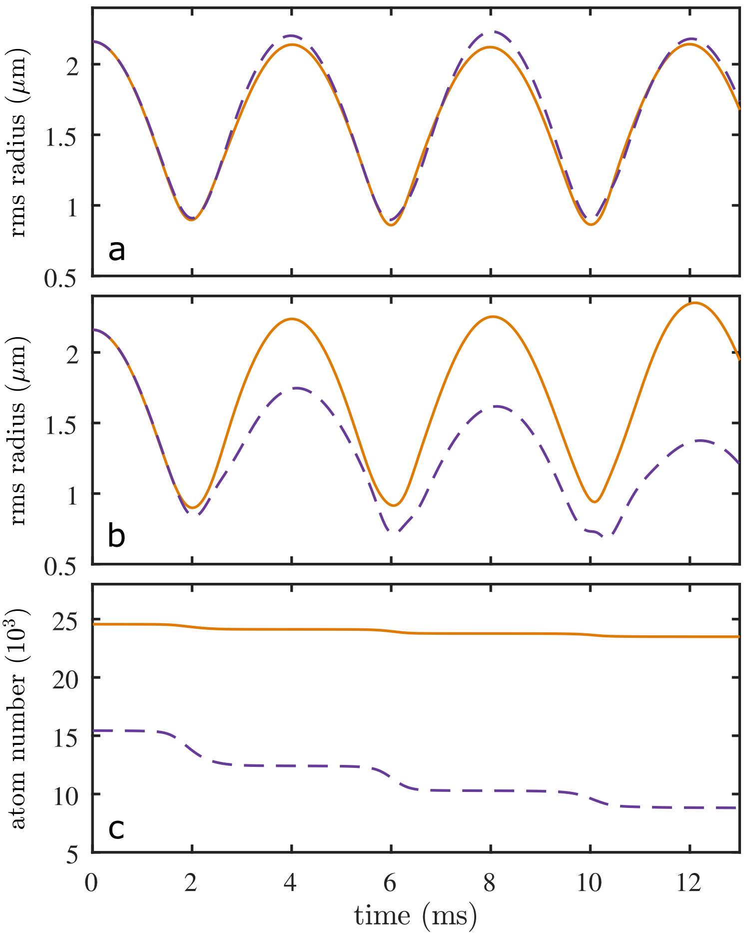

FIGURE 6.5: Typical results of the dynamical two-component simulations. (a) Simulated radii for a LHY fluid without including losses. (b-c) Simulated radii (b) and atom numbers (c) for a LHY fluid including inelastic losses. Results for atoms in states $|1\rangle$ and $|2\rangle$ are shown as solid orange and dashed purple lines, respectively. The simulations were performed using a spherical trap with trap frequency $\omega_0 = 2\pi \times 113.6\,\text{Hz}$ and atom number $N = 4 \times 10^4$ corresponding to $U = 1.2$. Panels (b) and (c) were published in a similar figure in Ref. [54].

that the system is initialized as a LHY fluid. The simulations were performed using a spherical trap with $\omega_0 = 2\pi \times 113.6\,\text{Hz}$ and atom number

$N = 4 \times 10^4$ corresponding to $U = 1.2$. Panel (a) shows the simulated root-mean-square radii of the wave functions for the $|1\rangle$ (solid orange) and $|2\rangle$ (dashed purple) states as a function of time without including inelastic losses. Similar to the experiment, the transfer initializes large amplitude oscillations as the system contracts towards its new equilibrium radius. When excluding losses, the wave functions of the two states oscillate jointly throughout the simulation duration with only minor differences appearing in the numerically calculated radii.

Panels (b-c) show the corresponding simulation results when including inelastic losses. The simulated radii are shown in panel (b), and the corresponding atom numbers are shown in panel (c). As the clouds contract, the density increases which results in increased inelastic losses coinciding with the minima in the radii. As expected, this severely influences the atom number in state $|2\rangle$, leading to a decay in the oscillations. Since the losses primarily affect atoms in state $|2\rangle$, the density ratio starts to deviate from $n_2/n_1 = \sqrt{a_{11}/a_{22}}$ resulting in increasing mean-field interactions. As a results, the atoms in state $|1\rangle$ feel an additional repulsion, which explains the increasing offset and amplitude visible in their cloud radius. The oscillation frequency is therefore determined both by the initial evolution governed by the dominant LHY interactions, as well as the further evolution, where the mean-field interactions become increasingly relevant.

The evolution of the simulated radii r as a function of time t is fitted using the function

$$r(t) = r_0 + st + A\sin(\omega t + \phi)\exp(-t/\tau), \tag{6.15}$$

where r_0 is an offset radius, s is a slope, A is the oscillation amplitude, ω is the angular frequency, ϕ is a phase offset, and τ is the time constant describing the growth or decay of the oscillations. Note that this function does not include the frequency chirp arising from the increasing mean-field interactions, and it therefore extracts the average oscillation frequency within the considered evolution time. As a consequence, it is essential that the same time span is considered when comparing the extracted frequency from simulation and experiment.

In practice, a duration of 13 ms is chosen in order to cover $\sim$ 3 oscillation periods, while a sizeable fraction of atoms remain in the $|2\rangle$ state. Due to the

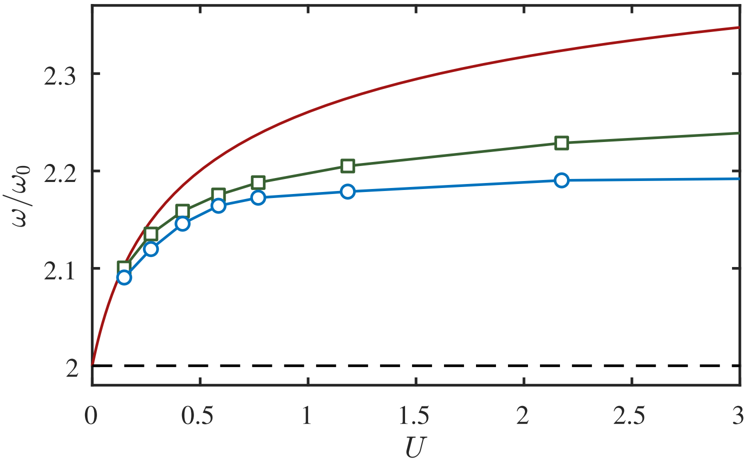

FIGURE 6.6: Simulated oscillation frequencies of atoms in the $|1\rangle$ state as a function of LHY interaction strength. Results with and without inelastic losses are shown as blue circles and green squares, respectively. The low-amplitude limit is shown as a red line and the non-interacting limit is shown as a dashed black line. A similar figure was published in Ref. [54].

strong losses of atoms in state $|2\rangle$, the experimental data quality is generally much better for state $|1\rangle$, and the oscillation frequency is therefore extracted from this state when comparing the simulated oscillations to experiment.

In Fig. 6.6 the simulated monopole oscillation frequency of the $|1\rangle$ state is shown as a function of the LHY interaction strength for a spherical trap with $\omega_0 = 2\pi \times 113.6\,\text{Hz}$ based on the typical experimental values. Separate simulations have confirmed that varying the trap frequency in the range 111-118 Hz has negligible influence on the extracted frequency. The simulation results with and without including losses are shown as blue circles and green squares, respectively. For comparison, the theoretical predictions for an ideal LHY fluid in the low-amplitude limit (Eq. (6.8)) is shown in red, and the non-interacting limit is shown in dashed black. For small U all results that include the LHY correction show an upward trend, however with increasing U, the simulated large-amplitude oscillations feature a pronounced reduction in frequency compared to the low-amplitude case. Including inelastic losses result in a further reduction of extracted frequency, which settles at $\omega/\omega_0 \sim 2.18$ for the investigated trap.

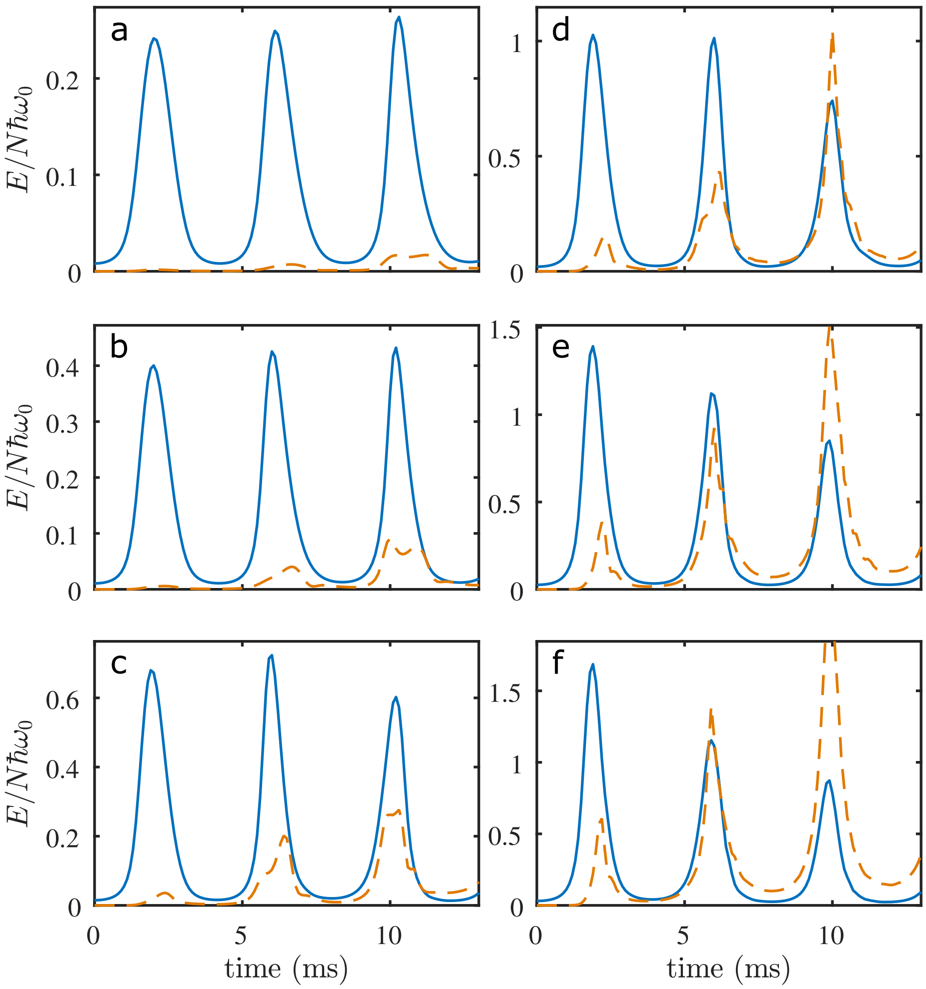

FIGURE 6.7: Simulated energy contributions from interactions throughout the experimental duration. The LHY and mean-field energies per particle are shown in solid blue and dashed orange, respectively, for $U = 0.15$ (a), $U = 0.27$ (b), $U = 0.58$ (c), $U = 1.2$ (d), $U = 2.2$ (e), and $U = 5.0$ (f). A similar figure was published in Ref. [54].

6.3.2 Energy Evolution

The inelastic losses result in a violation of $n_2/n_1 = \sqrt{a_{11}/a_{22}}$, and it is therefore natural to consider to which extent the realized system can be considered a LHY fluid. In order to evaluation this question quantitatively, the evolution of the LHY and mean-field energies throughout the simulation duration are considered. In practice this corresponds to evaluating the mean-field and LHY contributions to the energy by numerically integrating the corresponding energy density over all space using the calculated wave functions. In Fig. 6.7 the LHY (blue) and mean-field (dashed orange) energies per particle are shown for selected values of U. The energies evolve dynamically showing peaks as a consequence of the increased density as the system contracts. For small U corresponding to panels (a-c), the LHY energy dominates the mean-field energy throughout the data range and the system can safely be labelled a LHY fluid within the first three oscillations. For larger U the mean-field energy, however, becomes comparable to the LHY energy at the second contraction as exemplified in panels (d-f) and the system can only initially be considered a LHY fluid. Nonetheless, the initially dominant LHY interactions has a large influence on the evaluated oscillation frequency as evident from Fig. 6.6 when comparing the simulation results to the non-interacting limit of $\omega/\omega_0 = 2$.

Importantly, the deviation from an ideal LHY fluid is as a consequence of the experimental preparation method, which results in enhanced losses due to the strong contraction, and its lifetime could potentially be increased by preparing the system using another method.

6.4 Experimental Results

Based on the detailed theoretical description, a comparison with experimental data is now possible. In the following, all experiments are initialized as described in Sec. 6.2. A BEC in the $|1\rangle$ state is prepared in a spherical trap at the target magnetic field, and the experiment is initialized by transferring a fraction of the population to the $|2\rangle$ state using a rf pulse. The duration of the rf pulse is chosen based on a measurement of Rabi oscillations between the $|1\rangle$ and $|2\rangle$ states using thermal clouds, performed at a magnetic field of 56.831(2) G corresponding to $\delta a = 0$. The state composition was analysed by applying a magnetic field gradient during TOF expansion, and in Fig. 6.8 the population in the $|2\rangle$ state is shown as a function of pulse duration. The line shows a parabolic fit to the data, which is used to extract the initial population in a given experiment from the applied pulse length.

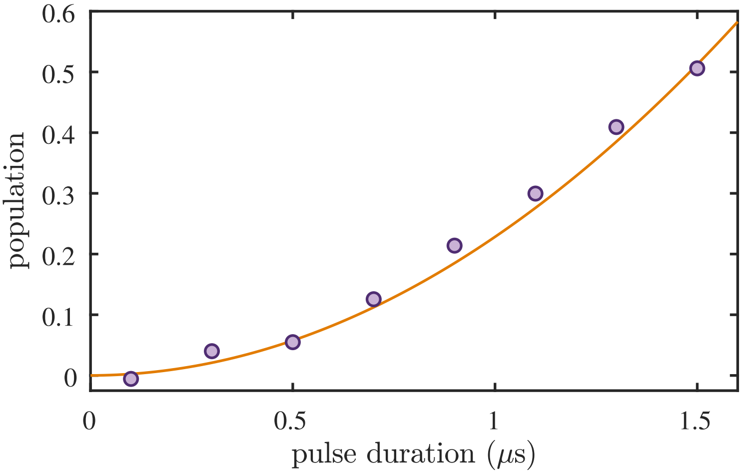

FIGURE 6.8: Population in the $|2\rangle$ state as a function of the duration of the rf pulse. The measurement was performed using thermal clouds at the magnetic field of 56.831(2) G corresponding to $\delta a = 0$. The line shows a quadratic fit to the data, which is used to determine the population from the pulse length in the different experiments. The error bars are smaller than the markers.

The resulting oscillation data after performing the rf transfer has the form shown in Fig. 6.4. In order to ensure that the oscillations are monopolar, Eq. (6.15) is first fitted separately to the radii along the y and z directions to extract the oscillation frequencies ω_i and the corresponding fit errors. The frequency difference $\delta\omega = |\omega_y - \omega_z|$ is then evaluated and data where $\delta\omega = 0$ does not lie within a 2σ confidence limit is discarded. For data where the criterion is fulfilled, another fit of Eq. (6.15) to the mean radii $r = (r_y + r_z)/2$ is performed in order to determine the monopole oscillation frequency ω.

The atom number for each experiment is determined from the number of atoms in the $|1\rangle$ state before the rf pulse. This method is employed because the severe inelastic losses of state $|2\rangle$ reduce the atom number in the beginning of the TOF when the density is still large. The trap frequencies are measured using the method described in Sec. 4.4, and the values for the employed traps are given in Appendix A.1 along with the deviations from the geometric mean along the individual axes.

6.4.1 Interaction Strength

In a first experiment, the monopole oscillation frequency was investigated as a function of the LHY interaction strength by preparing the system at $\delta a = 0$ and employing a rf pulse of 1.3 µs duration to realize the density ratio $n_2/n_1 = \sqrt{a_{11}/a_{22}}$. The LHY interaction strength U was varied by adjusting the total number of BEC atoms in the $|1\rangle$ state before the rf pulse through the loading time of ^{39}K in the dual-species MOT, and the trap frequency was kept in the range of 111-116 Hz[1].

The experimental data is shown in Fig. 6.9 where the different markers correspond to measurements using different trap frequencies as given in the caption. The vertical error bars are dominated by the uncertainty on the trap frequency ω_0, and the horizontal errors are dominated by the uncertainty on the atom number. The solid blue line shows the simulated oscillation frequencies calculated for $\omega_0 = 2\pi \times 113.6\,\mathrm{Hz}$ including inelastic losses, and the dotted blue line shows simulation results without losses. These curves were also shown in Fig. 6.6. The loss coefficient involving three atoms in the $|2\rangle$ state K_{222}^{th} is two orders of magnitude larger than the other coefficients, and it therefore contributes with the largest source of error on the numerical simulations. In the droplet experiments of Refs. [58, 59] an uncertainty on the value of K_{222}^{th} of a factor 2 is given, which is therefore used as an upper bound for the loss coefficient. Simulation results where K_{222}^{th} has been multiplied by a factor 2, while keeping the other loss coefficients constant, are therefore shown as a dash-dotted blue line. For comparison, the low-amplitude limit of the LHY fluid is shown in red and the non-interacting limit is shown in dashed black.

The experimental data follows the simulated results including losses very well, showing an initial increase in oscillation frequency until $U \simeq 1.5$, before settling on a value determined by the influence of the large amplitude oscillations and losses. The measured oscillation frequencies are thus consistent with the theoretical prediction for a LHY fluid undergoing large amplitude oscillations and decaying via losses of the $|2\rangle$ state. Additionally, the experimental data differs strongly from the non-interacting limit highlighting the large influence of the LHY correction on the oscillation frequency, even for large U where the LHY energy only dominates initially as shown in Fig. 6.7.

---

[1] Changes in ω_0 from day to day are inevitable because of drifts in the optical setup

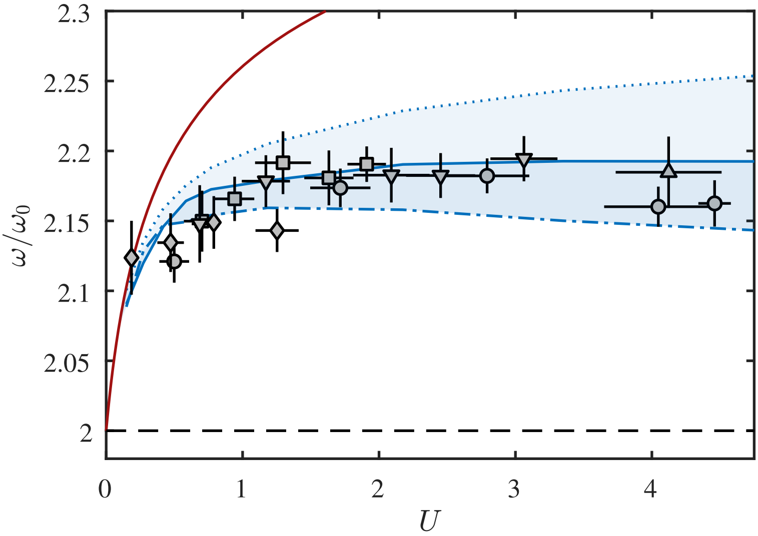

FIGURE 6.9: Observed monopole oscillation frequency as a function of the interaction strength of the LHY fluid for spherical traps with $\omega_0 = 2\pi \times 113.1(6)$ Hz (circles), 113.7(1) Hz (squares), 115.3(4) Hz (diamonds), 111.1(3) Hz (downwards triangles), and 110.9(5) Hz (upwards triangles). Simulated results calculated for $\omega_0 = 2\pi \times 113.6$ Hz including inelastic losses are shown as a solid blue line. The dotted and dash-dotted lines correspond to simulations without losses and a doubled loss coefficient for the channel involving three atoms in the $|2\rangle$ state, respectively. The red line shows the monopole frequency of an ideal LHY fluid in the low-amplitude limit and the dashed black line shows the non-interacting limit. A similar figure was published in Ref. [54].

6.4.2 Magnetic Field Strength

In a second set of experiments, the monopole oscillation frequency was investigated as a function of magnetic field around the optimal value corresponding to $\delta a = 0$. The experiment was performed using a spherical trap with $\omega_0 = 2\pi \times 110.9(5)$ Hz and atom number $N = 9.4(6) \times 10^4$. This corresponds to $U = 4.1(4)$ for $\delta a = 0$ and is thus in the limit of relatively large interaction strengths. As shown in Sec. 6.3.2, this means that the LHY and mean-field contributions to the energy are similar in magnitude after the first contraction. It is therefore interesting to investigate how the competition between the large LHY interactions and the strong losses, which pull the system towards a mean-field description, influence the measured oscillation frequency. The duration of the rf pulse was kept constant throughout the measurement, and the ideal density ratio $n_2/n_1 = \sqrt{a_{11}/a_{22}}$ was thus only fulfilled initially for the data point corresponding to $\delta a = 0$. Within the range of employed magnetic fields, this corresponds to a relative deviation of $\pm 10\,\%$, which is included in the simulations.

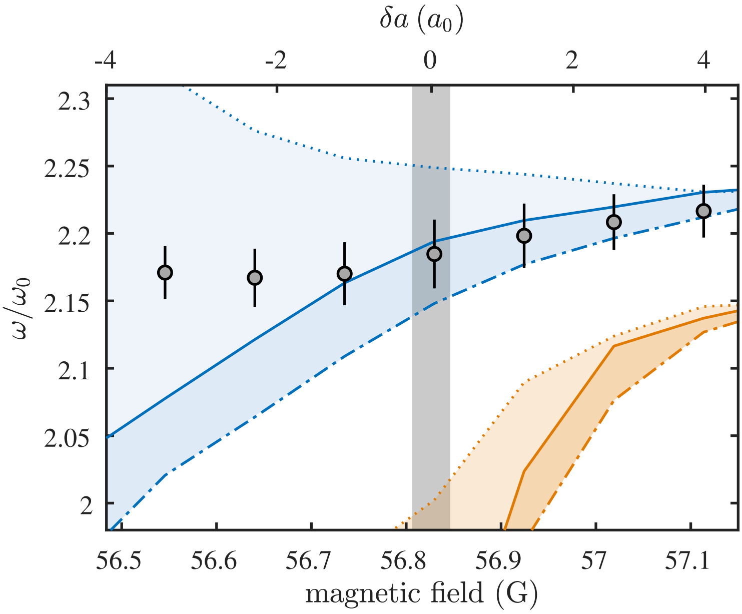

Figure 6.10: Monopole frequency of the spin mixture depending on magnetic field and δa. Experimental results for $\omega_0 = 2\pi \times 110.9(5)$ Hz and $N = 9.4(6) \times 10^4$ corresponding to $U = 4.1(4)$ are shown as grey points. Simulated results using the same parameters with and without including the LHY correction are shown in blue and orange, respectively. Here, the solid lines correspond to the best values for the loss coefficients, the dash-dotted lines feature a doubled loss coefficient for the channel involving three atoms in the $|2\rangle$ state, and the dotted lines neglect losses. The shaded region indicates the uncertainty on the calculated value of δa at the optimal magnetic field of 56.83 G. The horizontal errors on the experimental results are smaller than the markers. A similar figure was published in Ref. [54].

The experimentally extracted oscillation frequencies are shown in Fig. 6.10 as a function of magnetic field and δa. As evident from Fig. 6.2, a_{11} and a_{12}

are approximately constant within the investigated magnetic field regime and δa is therefore primarily determined by a_{22}. The grey shading corresponds to the uncertainty on δa at the optical magnetic field of 56.83 G, which is calculated by propagating the uncertainties on the individual scattering lengths into δa. Simulation results including the LHY terms in the extended GP equations are shown using the same line styles as in Fig. 6.9, and simulation results excluding the LHY terms are shown in orange[2]. Without the repulsive LHY contribution, the inelastic losses of atoms in state $|2\rangle$ are further enhanced, and for $\delta a \lesssim 0$ the simulated radii therefore feature a pronounced kink after the first contraction where most of the atoms in the $|2\rangle$ state are lost. This results in bad fits of Eq. (6.15) and the orange lines therefore only resemble the qualitative behaviour of the monopole oscillation frequency. A comparison of the simulated oscillations with and without including the LHY correction is shown in Appendix A.2, where the effect of neglecting the LHY correction is discussed. For magnetic field corresponding to $\delta a < 0$ the relative density ratio starts below the optimal value $n_2/n_1 < \sqrt{a_{11}/a_{22}}$ due to the constant duration of the rf pulse. With increasing hold time in the trap, the losses of atoms in state $|2\rangle$ result in a further decrease of n_2/n_1, and droplet formation is thus not allowed. Nonetheless, the simulation results without losses show an increase in frequency for increasingly negative δa, which agrees qualitatively with the prediction for quantum droplets [56, 217, 218].

For $\delta a \gtrsim 0$ the experimental data follows the simulation results including the LHY terms and the best value for the loss coefficients very well. For $\delta a < 0$ the agreement is less good which can be attributed to the large dependence on the exact values of the loss coefficients in this regime. The large influence of the LHY interactions on the measured oscillation frequency is clearly seen when comparing to the simulation results excluding the LHY terms. Here the oscillation frequency drops steeply towards the non-interacting limit of $\omega/\omega_0 = 2$ when approaching $\delta a = 0$ from the positive side and for $\delta a < 0$ the system collapses due to the attractive mean-field interactions. Similar to the experiments on quantum droplets, the repulsive interaction from quantum fluctuations thus prevents the mixture from collapsing, and the experimentally determined oscillation frequency is stable against variations

---

[2] For the simulations excluding LHY terms in the extended GP equations, the terms involving $E_{\text{LHY}}/\mathcal{V}$ in Equation (6.14) have also been neglected.

in the magnetic field. This agrees with the theoretical prediction of [53], which showed that the monopole frequency of the LHY fluid is stable in a window around the ideal scattering lengths for the lossless case.

6.4.3 Atom Number Ratio

In the final set of experiments, the monopole oscillation frequency was investigated as a function of the initial atom number ratio set by the duration of the rf pulse. The magnetic field was kept constant at the value corresponding to $\delta a = 0$, and the experiments were performed for $U = 4.1(4)$, similar to the experiment of the magnetic field dependence. The results are shown in Fig. 6.11 as a function of the atom number ratio N_2/N_1 and rf pulse duration together with simulation results using the same line styles as in Fig. 6.9. The grey shading corresponds to the optimal ratio $N_2/N_1 = n_2/n_1 = \sqrt{a_{11}/a_{22}} = 0.629(3)$ calculated at a magnetic field of 56.83 G, with the uncertainty determined by propagating the errors on the scattering lengths.

The simulated frequencies generally follow an increasing trend with larger values of N_2/N_1 until approaching an equal mixture. In this regime, the simulations results without losses become irregular for the $|1\rangle$ state resulting in a bad fit of Eq. (6.15), which causes the apparent decrease in oscillation frequency. This is not seen for the simulations including losses as the atom number ratio is pulled to lower values by the inelastic losses. A figure comparing these cases is shown in Appendix A.3.

The experimental data does not display a strong dependence on the initial atom number ratio in the vicinity of the ideal density ratio. This was also predicted in Ref. [53], where it was explained that adding an atom to either component at the point where $\delta a = 0$ and $N_2/N_1 = \sqrt{a_{11}/a_{22}}$ results in a negligible energy contribution due to the mean-field terms being cancelled. For $N_2/N_1 \gtrsim \sqrt{a_{11}/a_{22}}$, the data follows the simulation results with the best values for the loss coefficient very well, whereas for $N_2/N_1 < \sqrt{a_{11}/a_{22}}$ the experimentally extracted oscillation frequencies are systematically higher than the simulation results. This could indicate that the system is not well described by assuming a two-component mixture in the imbalanced case, or that the excellent agreement for $N_2/N_1 \gtrsim \sqrt{a_{11}/a_{22}}$ is coincidental, considering the general spread of the data. The simulation results nonetheless captures the general magnitude of the oscillation frequency, when compared to the non-interacting limit of $\omega/\omega_0 = 2$.

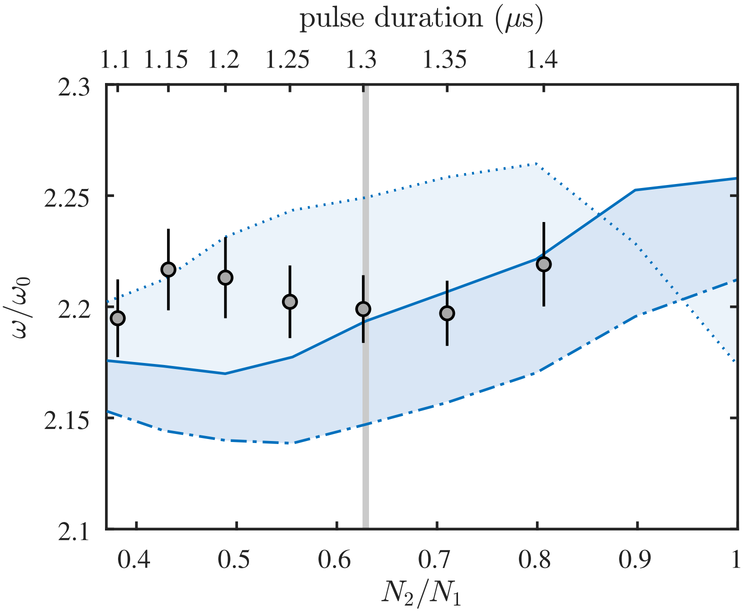

FIGURE 6.11: Monopole frequency of the spin mixture as a function of the initial relative atom number and rf pulse duration. Experimental results for $\omega_0 = 2\pi \times 110.9(5)$ Hz and $N = 9.4(6) \times 10^4$ corresponding to $U = 4.1(4)$ are shown as grey points, and simulated results using the same parameters are shown in blue. The solid line correspond to the best values for the loss coefficients, the dash-dotted line features a doubled loss coefficient for the channel involving three atoms in the $|2\rangle$ state, and the dotted line neglects losses entirely. The grey shading indicates the error on the optimal ratio $N_2/N_1 = \sqrt{a_{11}/a_{22}}$ for the magnetic field where $\delta a = 0$.

6.5 Summary and Outlook

In this chapter, the experimental observation of a LHY fluid was presented. Based on measurements of the collective oscillation frequency and detailed numerical simulations, it was possible to verify the creation of a system where the interactions are initially governed by quantum fluctuations. The monopole oscillation frequency of the system was investigated as a function of the LHY interaction strength and showed excellent agreement with the theoretical predictions. Moreover, the oscillation frequency was found to be stable against variations around the ideal magnetic field and initial atom number ratio, showing that the quantum fluctuations dominate the interactions in a regime around the ideal values.

Further experiments using the current setup could consist of measuring the LHY energy using a Ramsey interferometry scheme, similar to the one employed in Ch. 5, in order to track the relative phase evolution of the states. Thus, the decoherence time of the system could simultaneously be measured and used to verify the assumption of a decohered mixture used in the simulations.

The realization of a LHY fluid in ^{39}K could be improved based on the recent work of Ref. [219], which measured the effect of the LHY correction on a Rabi coupled ^{39}K BEC using the same states as in this work. Here the authors employed an adiabatic passage to prepare the system, where the shape and duration of the rf pulse was chosen such that is was adiabatic with respect to both the internal-state dynamics and the radial evolution of the wave function. This preparation method thus avoids the strong contraction and corresponding enhancement of losses which limited the lifetime of the LHY fluid in this work. Lavoine *et al.* [219] furthermore showed that during the Rabi coupling, the losses of state $|1\rangle$ and $|2\rangle$ are symmetric which simplifies the preparation method. Asymmetric losses after the adiabatic passage would however still limit the lifetime, and a system with less severe losses is preferable for further experiments.

Building on the results of Minardi *et al.* [203], a promising candidate could therefore be the ^{41}K–^{87}Rb mixture, which was recently found to support the existence of long-lived quantum droplets [61]. The apparatus used for this work has previously been employed in the production of dual-species ^{41}K–^{87}Rb condensates [129], however, because of the different masses, the two components have a differential gravitational sag, which must be compensated to realize the requirement $n_2/n_1 = \sqrt{a_{11}/a_{22}}$ for a LHY fluid. This could be achieved using a magnetic field gradient by exploiting the different magnetic moments of the species [61] or by an additional ODT beam with a "magic wavelength" [137, 220]. This would allow further investigations of the LHY dominated regime with interesting research directions including higher-order collective modes and different trap geometries. The LHY fluid furthermore provides a promising platform for observing even higher-order effects such as the next-order correction to the energy of a Bose gas, E_{WHPS} [221, 222], and on a broader scale, its realization enables new quantum simulation experiments utilizing the quartic non-linearity governing the interactions of the system.

CHAPTER 7

Progress on Hypervolume Experiments

In the limit where the s-wave scattering length a vanishes, the properties of the system are still determined by few-body scattering processes. In particular, for $a = 0$ the interactions in the system are governed by three-body interactions, characterized by the *three-body scattering hypervolume* D [69, 70], which has units of length to the fourth power.

In Ref. [71], D is calculated for different interaction potentials, and it is shown how three-body interactions can be used to stabilize quantum droplets. Furthermore, the dependence of the collective mode frequencies on D is calculated, showing that the monopole mode in a symmetric harmonic potential features the strongest dependence on its magnitude. By measuring the monopole frequency at $a = 0$, it is thus possible to infer the size of D.

Given that our apparatus has the capability to produce spherically symmetric potentials, working towards a measurement of D is a natural continuation of the research presented in Ch. 6, which also investigated a system with vanishing mean-field interactions.

The regime around $a = 0$ has been investigated previously in several contexts. An initial experiment prepared a ^{85}Rb BEC at $a = 0$ before initiating a collapse by changing a to negative values [94]. Following this, the expansion dynamics of a ^{7}Li BEC at $a = 0$ was investigated in a waveguide potential in the context of soliton formation [223]. The expansion of BECs at $a = 0$ was also investigated in free space using ^{133}Cs [224, 225] and ^{39}K [226], which showed that the expansion energy was minimized for a vanishing s-wave scattering length. In the context of atom interferometry, experiments with ^{39}K [227] and ^{133}Cs [228] in optical lattices showed that tuning a to zero lead to an increased coherence time of Bloch oscillations. Other experiments investigated the region where $a = 0$ in the context of the magnetic dipole interaction, where strong dipolar effects were observed in ^{52}Cr by reducing a relative to the magnetic dipole interaction [229], and evidence of a weak anisotropic magnetic dipole interaction for small a was observed in ^{7}Li [230].

In this chapter, our recent progress towards a measurement of D is presented. In Sec. 7.1, the relevant results of Ref. [71] are reviewed and their results are compared with numerical simulations of the system. Following this, the experimental feasibility of measuring the three-body scattering hypervolume using ^{39}K is discussed in Sec. 7.2, where further simulations of the experimental signal are presented. Section 7.3 describes the experimental procedure for production of ^{39}K BECs in the specific state and magnetic field regime, where the measurement of D is to be performed. Finally in Sec. 7.4, initial experiments towards the determination of the magnetic field where $a = 0$ and measurements of the loss coefficient are presented.

Within this chapter, all simulations and the data analysis was performed by me. The experimental efforts were lead by me and performed in collaboration with the newest PhD student of the team Andreas M. Morgen.

7.1 Bose-Einstein Condensates at Vanishing s-wave Scattering Lengths

The energy-density of a uniform BEC at $a = 0$ is given by [69]

$$\mathcal{E}(n) = \frac{\hbar^2 D n^3}{6m} + \dots, \tag{7.1}$$

where n is the number density, m is the atomic mass, and the dots indicate smaller terms of higher power in n. The extended Gross-Pitaevskii equation including the three-body scattering hypervolume is thus [71]

$$i\hbar\dot{\psi} = -\frac{\hbar^2}{2m}\nabla^2\psi + V\psi + \frac{4\pi\hbar^2 a}{m}|\psi|^2\psi + \frac{\hbar^2 D}{2m}|\psi|^4\psi, \tag{7.2}$$

where $\psi(\mathbf{r},t) = \sqrt{N}\phi(\mathbf{r},t)$ is the condensate wave function with atom number N and single-particle wave function $\phi(\mathbf{r},t)$, while the external potential $V(\mathbf{r}) = m\omega_0^2\mathbf{r}^2/2$ is assumed to be a spherically symmetric harmonic oscillator with trap frequency ω_0. The LHY term which scales with $a^{5/2}n^{3/2}$ has been neglected, since $a \simeq 0$ in the following calculations.

In general, D is a complex number with the real and imaginary parts corresponding to elastic and inelastic scattering, respectively. The imaginary part is proportional to the three-body recombination rate [231, 232] via

$$L_3 = -\mathrm{Im}(D)\hbar/m, \tag{7.3}$$

where L_3 is the three-body loss coefficient. Inelastic losses due to three-body recombination can thus readily be included in Eq. (7.2) by allowing D to have an imaginary part.

In Ref. [71], Mestrom *et al.* solves the three-body problem for different two-body interaction models that all contain the long-range atomic van der Waals attraction. The authors find that the real part of D is universally fixed by the van der Waals range $r_{\mathrm{vdW}} = (mC_6/\hbar^2)^{1/4}/2$, where C_6 is the coefficient describing the long-range behaviour of the interaction. In the vicinity of $a = 0$, D is thus determined by a and r_{vdW}, with its real part $\mathrm{Re}(D)$ ranging from $\sim$ 100 to 200 r_{vdW}^4 in the range $a = -0.1\ r_{\mathrm{vdW}}$ to $a = 0.1\ r_{\mathrm{vdW}}$.

As explained in Sec. 6.1, measurements of the collective excitations in quantum gases serve as a powerful probe of the interatomic interactions. In Ref. [71], a time-dependent Gaussian trial wave function is used to investigate how the collective mode frequencies ω at $a = 0$ depend on the following parameter for the interaction strength

$$K = \frac{2DN^2}{9\sqrt{3}\pi^3 a_{\mathrm{ho}}^4}, \tag{7.4}$$

where a_{ho} is the harmonic oscillator length, and D is assumed to be a real number. The frequencies of the different modes are compared for different symmetries of the external potential, and the monopole mode in a isotropic geometry turns is found to experience the biggest shift in oscillation frequency with a Thomas-Fermi limit of $\omega_{3\text{bd, TF}} = 2\sqrt{2}\omega_0$.

The frequency of the monopole mode can also be determined by simulating the system in GPELab by implementing Eq. (7.2). In a first simulation, the system is considered for $a = 0$ and D is considered to be a real number, thus neglecting losses. The ground state of the system is first determined, after which oscillations are initialized by rescaling the simulation grid by a factor $1/1.001$ and renormalizing the wave function. This makes the wave function slightly narrower than the calculated ground state, and it therefore undergoes monopole oscillations when subsequently calculating dynamical evolution in the harmonic potential. The factor of $1/1.001$ was chosen to ensure a small oscillation amplitude. The dynamical simulation outputs the root-mean-square radius of the wave function as a function of time, and the oscillation frequency ω can thus be determined by fitting a sinusoidal function to simulation data.

In practice, the system is assumed to consist of ^{39}K atoms with a van der Waals range of $\sim 65\ a_0$ [233–235], and the value of $\text{Re}(D)$ is extracted from the results of Ref. [71], which calculated D as a function of a for different two-body interaction potentials. For the Lennard-Jones type potential $\text{Re}(D) = 144 r_{\text{vdW}}^4$ at $a = 0$, and this value is used in the simulation. The trap frequency is held constant at a value of $\omega_0 = 2\pi \times 300\,\text{Hz}$, and K is varied through the atom number N.

The monopole oscillation frequency at $a = 0$ is shown as a function of K in Fig. 7.1 with a logarithmic x-axis. The result of Mestrom *et al.* [71] using a Gaussian trial wave function is shown in solid green, the simulation result is shown in dashed orange, and the Thomas-Fermi limit is given in dotted black. The inset shows a zoom around small values of K with a linear axis with the Thomas-Fermi limit of a mean-field BEC shown in dash-dotted black.

Both the analytical and simulation results connect with the non-interacting limit of $\omega = 2\omega_0$ for vanishing K, while for large K, both results approach the Thomas-Fermi limit of $\omega_{3\text{bd, TF}} = 2\sqrt{2}\omega_0$. In the intermediate regime, the result using a Gaussian trial wave function features a steeper increase than the simulated result. This is not surprising since the Gaussian ansatz features a higher central density than the actual ground state, which has

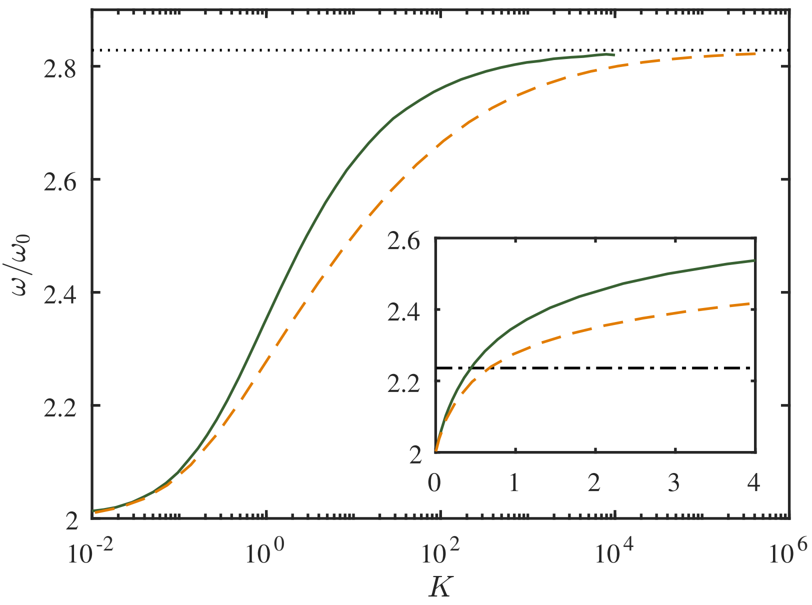

FIGURE 7.1: Comparison of the calculated monopole oscillation frequencies. The solid green line shows the results of Mestrom *et al.* [71] using a trial wave function, the dashed orange line shows simulation results, and the dotted black line shows the Thomas-Fermi limit. The inset shows a zoom around small values of K with a linear x-axis, and the Thomas-Fermi limit of a mean-field BEC shown in dash-dotted black.

a wider profile as a consequence of the repulsive three-body interaction. Performing the simulation for different values of N, ω_0, or D results in the same behaviour of ω as a function of K.

The simulated results of Fig. 7.1 show that the monopole oscillation frequency at $a = 0$ depends strongly on the value of D, and differs remarkably from the expected oscillation frequency of $2\omega_0$ for a BEC at $a = 0$ excluding the three-body interactions. Furthermore, the calculated oscillation frequency exceeds the Thomas-Fermi limit of a mean-field BEC already for $K \sim 0.7$ corresponding to an experimentally feasible atom number of 8×10^4 for the considered trap. As a consequence, the monopole frequency serves as a strong experimental signature of the three-body scattering hypervolume and its magnitude can be inferred from the experimentally measured oscillation frequency.

7.2 Experimental Feasibility

In order to measure the three-body scattering hypervolume, the mean-field contribution to the energy density must removed by tuning a to 0 by addressing a Feshbach resonance which features a zero-crossing in the scattering length. This is realizable using ^{39}K due to its rich Feshbach resonance structure.

At low magnetic fields, the $|1,0\rangle$ state features a zero-crossing at 44 G, which was shown in Fig. 2.1(b). However, as evident from the LHY fluid experiments presented in Ch. 6, using this state is complicated by its large three-body loss coefficient. Calculations by the group of S. Kokkelmans show that even in the vicinity of the zero-crossing, the three-body loss coefficient is $\sim 3\times 10^{-28}\,\mathrm{cm^6s^{-1}}$, which is an order of magnitude larger than the background value of $7.74\times 10^{-29}\,\mathrm{cm^6s^{-1}}/3! = 1.29\times 10^{-29}\,\mathrm{cm^6s^{-1}}$ used for the other states in Ch. 6.

Fortunately, all three states of the $F = 1$ manifold feature wide Feshbach resonances at larger magnetic fields. Figure 7.2(a) shows the intrastate Feshbach resonances of the three states in the magnetic field regime of 300 to 600 G. The scattering length as a function of magnetic field is shown in red for the $|1,-1\rangle$ state, in green for the $|1,0\rangle$ state, and in orange for the $|1,1\rangle$ state. Of these, the zero-crossing for the $|1,1\rangle$ state is preferred since its Feshbach resonance has been employed and studied in several other experiments, such as those in Refs. [83, 85, 89, 140, 189, 226, 227, 236]. Furthermore, the $|1,1\rangle$ state is the absolute ground state of ^{39}K, and it is therefore expected to feature the smallest losses since e.g. two-body spin-changing collisions are forbidden. The magnetic field for the zero-crossing of this state is marked by a dashed black line in Fig. 7.2(a)

In Fig. 7.2(b) a zoom around the $|1,1\rangle$ zero-crossing is shown where the calculated scattering length is provided by the group of S. Kokkelmans. Based on this calculation the location of the zero-crossing is found to be 350.7 G, which matches the value obtained by using the usual formula for the scattering length in the vicinity of a Feshbach resonance[1] [27]

$$a(B) = a_{\mathrm{bg}}\left(1 - \frac{\Delta}{B - B_0}\right), \tag{7.5}$$

---

[1] Equation (7.5) was also given in Sec. 2.2.1, but is repeated here for ease of reference.

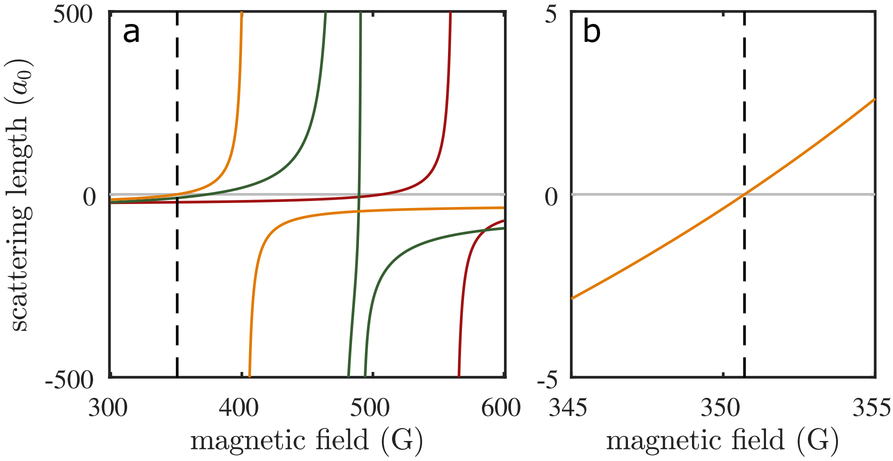

FIGURE 7.2: Intrastate Feshbach resonances for the $F = 1$ manifold of ^{39}K at large magnetic fields. (a) The scattering length is shown as a function of magnetic field is shown in red for $|1, -1\rangle$ [83], in green for $|1, 0\rangle$ [146], and in orange for $|1, 1\rangle$ [189]. The magnetic field for the zero-crossing of the $|1, 1\rangle$ state is marked by a dashed black line. (b) Zoom around the zero-crossing for the $|1, 1\rangle$ state. The calculated scattering length is provided by the group of S. Kokkelmans and is based on the K–K potentials of Ref. [213].

with background scattering length $a_{\mathrm{bg}} = -29\, a_0$ and width parameter $\Delta = -52\,\mathrm{G}$ from Ref. [83] and the resonance position $B_0 = 402.70(3)\,\mathrm{G}$ from Ref. [189].

7.2.1 Magnetic Field Dependence

In Ref. [71], the three-body scattering hypervolume was calculated as a function of a in a regime around $a = 0$. Since the value of a can be calculated as a function of magnetic field using Eq. (7.5), the dependence of the monopole frequency on the magnetic field can be simulated using GPELab.

Fig. 7.3 shows the simulated monopole oscillation frequency as a function of magnetic field and a for a constant atom number of $N = 1 \times 10^5$ and varying trap frequencies ω_0 as given in the legend. The Thomas-Fermi limit for a mean-field BEC is shown by the dashed line. The simulation was performed using the same method as for the results in Fig. 7.1, and the used values for D are extracted as a function of a from the results of Ref. [71] using a Lennard-Jones potential. Within the investigated range, $\mathrm{Re}(D)$ varies from 144 to 104 r_{vdW} (from lower to higher magnetic fields).

The simulated monopole oscillation frequency depends strongly on the trap frequency for $a = 0$, where the variation in trap frequency corresponds to changing K from 0.1 to 4.3. For larger magnetic fields where $a > 0$, the dependence on the trap frequency decreases as the mean-field term scaling with an becomes dominant, and the monopole oscillation frequency tends towards the mean-field Thomas-Fermi limit. These simulation results again predict a large effect of three-body interactions on the monopole oscillation frequency in the vicinity of $a = 0$, and measuring the effect experimentally is therefore viable.

7.2.2 Inelastic Losses

The effect of inelastic losses can readily be implemented in the simulations by including the imaginary part of D in Eq. (7.2). The three-body loss coefficient for atoms in the $|1,1\rangle$ state has previously been measured to $L_3 = 1.3 \times 10^{-29}\,\mathrm{cm}^6\mathrm{s}^{-1}$ in the region of the zero-crossing [227], and from Eq. (7.3) this corresponds to $\mathrm{Im}(D) = -59\, r_{\mathrm{vdW}}^4$, which is on the same order of magnitude as the results for $\mathrm{Im}(D)$ given in Ref. [71].

Including losses generally has two effects on the simulated results. The first is illustrated in Fig. 7.4, which shows simulated radii (a) and atom numbers (b) as a function of time for $\mathrm{Re}(D) = 135\, r_{\mathrm{vdW}}$ and $\mathrm{Im}(D) = -59\, r_{\mathrm{vdW}}^4$. The ground states were calculated using a trap frequency $\omega_0 = 2\pi \times 300\,\mathrm{Hz}$ and varying atom numbers N as given in the legend. The oscillations were initialized by abruptly increasing the trap frequency by 10 % to $\omega_{\mathrm{f}} = 2\pi \times 330\,\mathrm{Hz}$, and the corresponding values of K also given in the legend are calculated from ω_{f}. For larger N or ω_{f}, the losses tend to extinguish the oscillations since their effect scales with the square of the density as evident from Eq. (7.2). This is effect is seen in the atom number, where the relative effect of losses are larger for larger N. For small K, the oscillation frequency can be extracted by fitting the model function Eq. (6.15) used for the LHY fluid experiments to the simulated radii, however, for larger K the oscillations are damped too strongly for this to work. The second effect of the losses is an effective lowering of K with increasing evolution time as

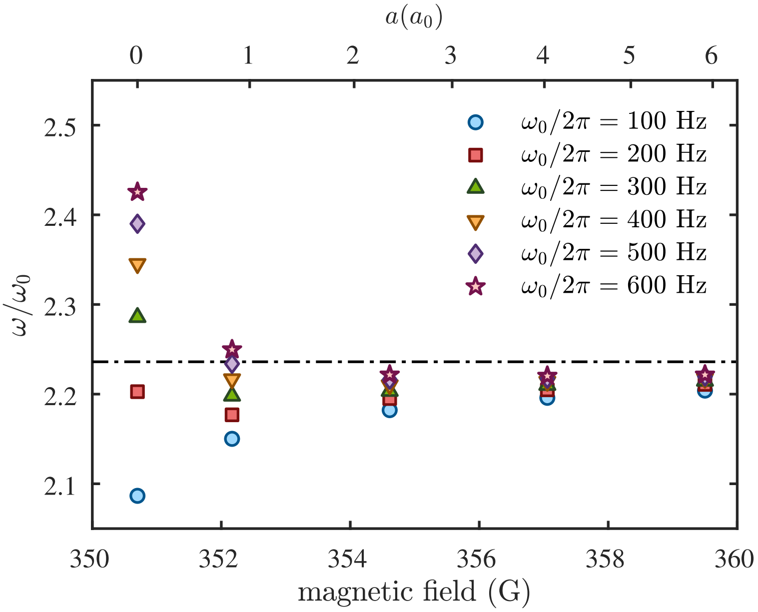

FIGURE 7.3: Simulated oscillation frequencies for vanishing and small positive scattering lengths. The markers show simulated monopole oscillation frequencies for atom number $N = 1 \times 10^5$ using the trap frequencies given in the legend. The Thomas-Fermi limit of $\omega = \sqrt{5}\omega_0$ for a mean-field BEC is shown in dash-dotted black. The simulation results at $a = 0$ correspond to K varying from 0.1 to 4.3. The values of Re(D) used in the simulation vary from 144 to 104 r_{vdW} within the investigated range (from lower to higher magnetic field), and are based on the results of Ref. [71] using a Lennard-Jones type potential.

the atom number decreases. As a consequence, the oscillation frequency is chirped towards lower values.

Experimentally, the first issue can be circumvented by increasing the oscillation amplitude. One method is to perform a larger jump in the trap frequency, corresponding to a bigger change in the powers of the trapping beams. Another method consists of quenching the system into $a = 0$ similar to the LHY fluid experiments of Ch. 6, which could be done by either abruptly changing the magnetic field or using a fast transfer into the state. These methods, however, result in a more challenging comparison to theory, since the resulting large-amplitude oscillations are expected to influence

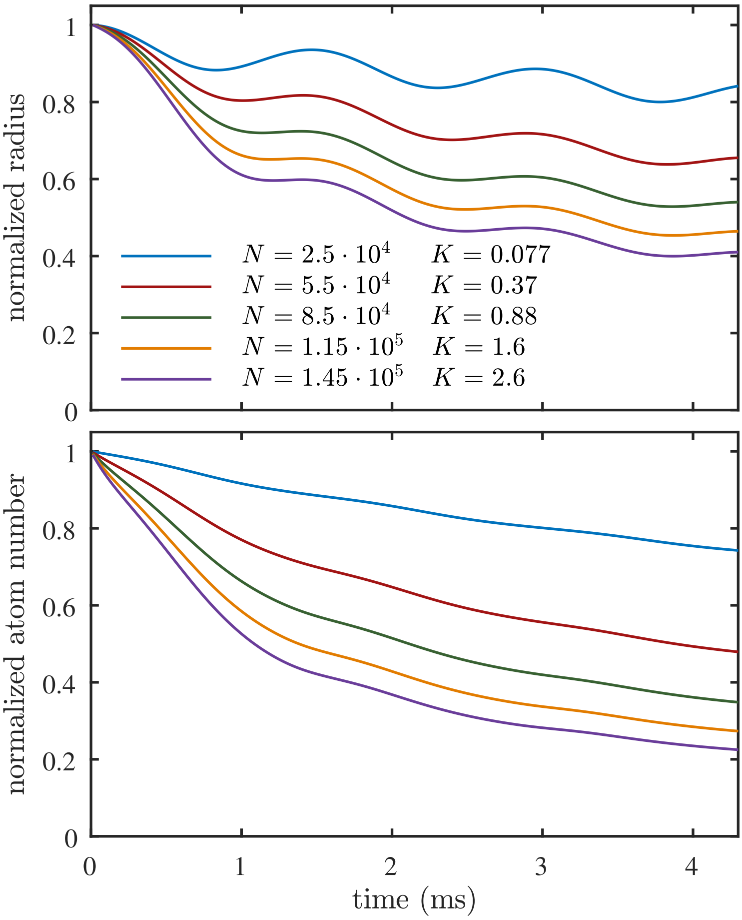

Figure 7.4: Simulation results for vanishing scattering length including inelastic losses. The root-mean-square radius (a) and atom number (b) normalized to their initial values are shown as a function of time. The ground states were calculated using a trap frequency of $\omega_0 = 2\pi \times 300\,\mathrm{Hz}$ and the oscillations were initialized by abruptly increasing ω_0 by 10 %. The atom numbers and corresponding values of K based on the final trap frequency are given in the legend.

the oscillation frequency. This is especially the case for the second method, where the system is initialized in a state that is very different from the ground state after the quench. In any case, inelastic losses will affect the oscillation frequency, and a complete simulation of the system is likely necessary in order to extract Re(D).

Alternatively, the resonance frequency could potentially be extracted through modulation spectroscopy. In this method, monopole oscillations would be excited by modulating the powers in the trapping beams, and the system response could be investigated as a function of the modulation frequency. This method can for example be used for trap frequency measurements, where the number of atoms that are lost due to parametric heating are used as the spectroscopic signal.

7.3 Production of ^{39}K BECs in the Absolute Ground State

The remainder of the chapter describes the current status of the experimental effort towards measuring the three-body scattering hypervolume. The shown results should be considered as work in progress, and the described methods are subject to change with further investigation. Compared to Ch. 4, which provided an overview of the apparatus, the following sections feature more details on the experimental procedure, which allows the content of this chapter to be used as a reference for future progress.

As explained in the previous section, a ^{39}K BEC in the $|1,1\rangle$ state is desired in order to address the zero-crossing of the scattering length at 350.7 G. To simplify the experimental procedure and enable the production of large BECs, the evaporative cooling is therefore performed in the $|1,1\rangle$ state in the vicinity of the Feshbach resonance at 402.7 G as done previously in Refs. [140, 143, 226].

7.3.1 State Preparation

The procedure for the production of ^{39}K BECs in the $|1,1\rangle$ state is similar to the normal method explained in Ch. 4, up to and including the transfer to the ODT. At this point the sample consists of a thermal cloud of ^{39}K atoms in the $|2,2\rangle$ state. After the transfer to the ODT, the coils are switched to Helmholtz configuration realizing a homogenous magnetic field along the vertical direction, which is ramped to a strength of 27 G over a 5 ms duration.

Here, a rapid adiabatic passage is performed from the $|2,2\rangle$ to the $|1,1\rangle$ state. The state transfer is performed by sweeping the homogeneous magnetic field from 27 G to 33 G over a duration 10 ms, while irradiating the sample with a constant radio frequency of 526.992 MHz. The frequency of the radiation was chosen based on a spectroscopic measurement performed at a Helmholtz current corresponding to the centre of the magnetic field sweep. The duration and range of the magnetic field ramp was optimized experimentally by analysing the resulting state composition after separating the m_F components with a magnetic field gradient during TOF expansion.

7.3.2 Imaging of ^{39}K at Moderate Magnetic Fields

After the transfer to the $|1,1\rangle$ state, the magnetic field is linearly ramped to the vicinity of the Feshbach resonance at 402.7 G over a duration of 250 ms. At this point, however, a complication appears due to the design of the mount of the Helmholtz coils, which is made of copper to ensure efficient water cooling.

The normal scheme for absorption imaging takes place using a homogenous magnetic field of 1 G along the x-direction in which the imaging light propagates. This magnetic field is applied during TOF expansion, while the vertical field from the main Helmholtz coils is turned off. This procedure works for magnetic fields strengths up to at least 150 G, which was used in the experiments of Ref. [137]. However, rapidly turning off the coils from a large magnetic field results in Eddy-currents in the copper mount, and the magnetic field direction is thus unable to change to the x-direction within the duration of the TOF expansion [129]. This issue could be circumvented by rebuilding the mount in a non-conducting material, or by performing the imaging at large magnetic fields using the method of Ref. [237], which, however, would require a significant reconfiguration of the optical setup.

Since the normal imaging scheme does not work after ramping to high magnetic fields, the imaging is performed while keeping on the Helmholtz field, which thus sets the vertical z-direction as the quantization axis. However, to avoid big changes in the optical setup, the imaging is performed at moderate magnetic field strength as follows: After releasing the atoms from the ODT, the magnetic field strength is kept in the range of 400 G during the first 4 ms of TOF. Subsequently, the magnetic field is ramped to a desired strength of 60 G over a duration of 5 ms. The following 7 ms of TOF expansion and the imaging are then performed at this magnetic field, and the frequencies of the imaging and repump light must therefore be tuned such that they are resonant with the relevant transitions at 60 G.

The energies of the relevant states are shown as a function of the magnetic field strength in Fig. 7.5. The energies of the $4^2\mathrm{S}_{1/2}$ manifold are shown in the lower panel and were calculated using the Breit-Rabi formula (Eq. (4.4)). The energies of the states in the $4^2\mathrm{P}_{3/2}$ manifold are shown in the upper panel and were calculated by numerically diagonalizing the Hamiltonian $H = H_{\mathrm{hfs}} + H_B$, where H_{hfs} is the hyperfine Hamiltonian (Steck [122] Eq. 15) and H_B is the Hamiltonian describing the interaction with the magnetic field (Steck [122] Eq. 20). The states are coloured according to the their low-field quantum number F, and the high-field quantum numbers $|m_J, m_I\rangle$ are given to the right.

At a magnetic field of 60 G, the lower $4^2\mathrm{S}_{1/2}$ manifold is in the intermediate magnetic field regime, while the states of the upper $4^2\mathrm{P}_{3/2}$ manifold are in the Paschen-Back regime. In the Paschen-Back regime, the electronic and nuclear angular momenta become uncoupled, and selection rules for dipole allowed transitions are therefore given by

$$\Delta I = 0, \tag{7.6}$$

$$\Delta m_I = 0, \tag{7.7}$$

$$\Delta J = \pm 1 \tag{7.8}$$

$$\Delta m_J = 0, \pm 1, \tag{7.9}$$

and the nuclear spin I is therefore unaffected by the radiation according to the first two rules.

The proposed transitions for the imaging scheme are shown in Fig. 7.5 by the blue and red arrows, and in the following, the quantum numbers of the states in the $4^2\mathrm{P}_{3/2}$ manifold with $J = 3/2$ are denoted by primes. The blue arrow corresponds to repumping light which transfers the atoms from the $|-1/2, 3/2\rangle$ to the $|1/2', 3/2'\rangle$ state. From here the atoms can decay back to either the $|-1/2, 3/2\rangle$ or $|1/2, 3/2\rangle$ states. The imaging is

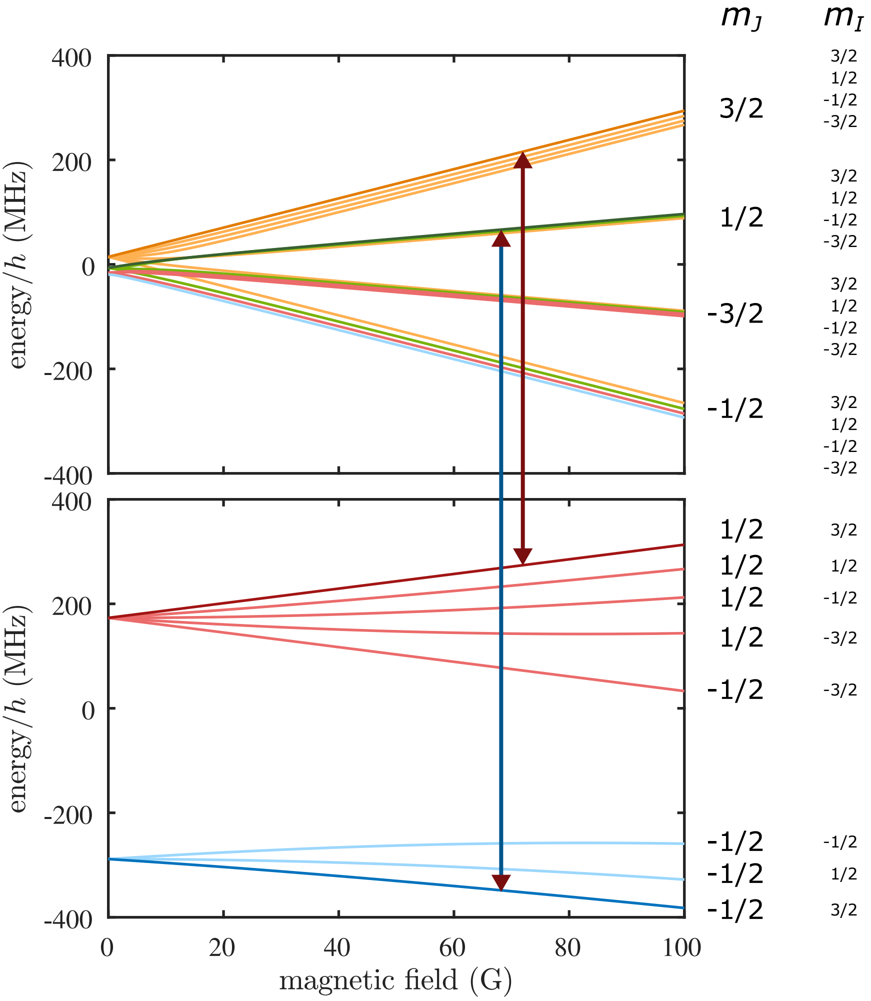

FIGURE 7.5: Energy as a function of magnetic field for the $4^2S_{1/2}$ (lower) and $4^2P_{3/2}$ (upper) manifolds of ^{39}K. The origins of the two y-axes are separated by 391.1 THz. The states are coloured according to their weak-field quantum numbers $F = 1$ (blue), 2 (red), 3 (green), 4 (orange). The strong field quantum numbers of the states $|m_J, m_I\rangle$ are given to the right. The repump and imaging transitions are shown by the blue and red arrow, respectively.

therefore performed on the $|1/2, 3/2\rangle$ to $|3/2', 3/2'\rangle$ transition, which is closed according to the selection rules given in Eq. (7.9).

The imaging is performed using the same laser beams as normally such that the imaging light propagates along the x-direction, while the repumping light hits the atoms along the z-direction from above. In order to achieve an absorption signal, the laser frequencies and polarizations must be changed such that they can drive the transitions described above. The imaging and repump light are supplied by separate lasers, which are the same as those used for cooling and repumping light in the MOT phase. The imaging beam is supplied by the cooling laser and this name is therefore also used here.

The frequencies of the two lasers are both locked relative to a master laser which is stabilized via saturated absorption spectroscopy to the $F = 1, F = 2 \rightarrow F'$ crossover resonance in ^{39}K [238], which lies 49 MHz above the unperturbed $4^2\mathrm{S}_{1/2} \rightarrow 4^2\mathrm{P}_{3/2}$ transition frequency of 391.1 THz. The beat frequencies between the master laser and the cooling and repump lasers, respectively, are recorded on fast photodiodes, and the beat frequencies are stabilized to references set by a frequency synthesizer using phase locked loops. The locking scheme was designed in this way to enable easy switching between the different isotopes of K by changing the reference frequency of the beat locks [128, 129]. This ability is also used here, since it enables the frequencies to be changed without changing the optical setup. In order to match the transitions given in Fig. 7.5, the frequencies of the imaging and repump beams must be shifted upwards by ~ 100 MHz compared to the usual imaging scheme, which is achieved by changing the beat lock frequencies after the MOT phase of the experiment using GPIB commands.

In the desired imaging scheme, both beams address σ^+-transitions, and the beam polarizations must be chosen accordingly, while taking into account the quantization axis set by the homogenous magnetic field in the vertical direction. The repumping light propagates along this direction and hits the atomic cloud from above. In order to drive the σ^+ transition, a quarter-wave plate is therefore inserted in its beam path to achieve a circular polarization. The imaging beam hits the atoms along the x-direction which is perpendicular to the quantization axis. In order to drive the σ^+-transition, the light polarization is therefore chosen to be linear along the y-direction by exchanging the quarter-wave plate, used in the normal imaging scheme, for a half-wave plate.

The ability of the linearly polarized light to drive $\sigma^{\pm}$-transitions can be seen by considering the dipole matrix element $\langle \mathrm{g}|\hat{\mathbf{e}} \cdot \mathbf{d}|\mathrm{e}\rangle$ with the unit polarization vector pointing in the y-direction $\hat{\mathbf{e}} = (0, 1, 0)$ and $\mathbf{d} = -e\mathbf{r}_e = -e(x, y, z)$. In this case, $\hat{\mathbf{e}} \cdot \mathbf{d} = -ey = -er \sin\theta \sin\phi$ and the azimuthal part of the dipole matrix element becomes

$$\begin{aligned} &\int_0^{2\pi} \mathrm{d}\phi \, e^{i(m_\mathrm{e}-m_\mathrm{g})\phi} \sin\phi \\ &\qquad = \frac{1}{2i} \left[\int_0^{2\pi} \mathrm{d}\phi \, e^{i(m_\mathrm{e}-m_\mathrm{g}+1)\phi} - \int_0^{2\pi} \mathrm{d}\phi \, e^{i(m_\mathrm{e}-m_\mathrm{g}-1)\phi} \right], \end{aligned} \tag{7.10}$$

where m_g and m_e are the magnetic quantum numbers of the $|\mathrm{g}\rangle$ and $|\mathrm{e}\rangle$ states, respectively, and ϕ is the azimuthal angle. The integrals in the square brackets equal zero unless $m_\mathrm{e} - m_\mathrm{g} = \mp 1$, respectively, and thus correspond to $\sigma^{\pm}$-transitions [239].

Figure 7.6(a) shows the measured atomic signal as a function of the frequency of the imaging light using the imaging scheme described above. The red line shows a Lorentzian fit to the data, which yields a centre frequency of 411(2) MHz and corresponds to a magnetic field of 69(1) G. This value is 9 G above the expected magnetic field of 60 G from the calibration, which shows that the magnetic field does not settle on its final value within the 7 ms from the end of the current ramp and the imaging.

Figure 7.6(b) shows the measured atomic signal as a function of the rotation angle of the half-wave plate, which controls the polarization direction of the imaging beam. The blue line is a sinusoidal fit to the data, which yields an oscillation period of 89.2(2)° and agrees very well with the expected period of 90°, given the low amount of data points. The data shows how the absorption signal can be extinguished completely by choosing the polarization to be parallel to the magnetic field axis thus that the light is unable to drive the required σ^{+} transition.

The frequency of the repump light can now be chosen based on the measured magnetic field strength of 69 G. The measurement is performed similar to that of Fig. 7.6(a) with the beat lock frequency of the imaging light kept constant at 411 MHz, while the frequency of the repump light relative to the master laser is varied. The measurement resulted in a more than 30 MHz wide signal with a flat top, signalling that the repump transition is saturated.

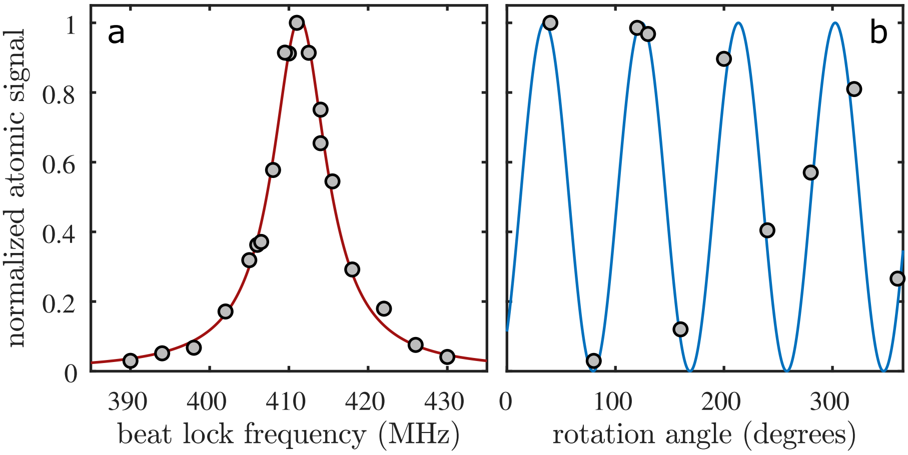

FIGURE 7.6: Absorption signal depending on the frequency of the imaging beam and its polarization direction. (a) Normalized atomic signal as a function of the frequency difference between the imaging laser and the master laser, which is controlled by the reference frequency of the beat lock. The red line shows a Lorentzian fit to the data. The fitted centre frequency of 411(2) MHz corresponds to a magnetic field of 69(1) G. (b) Normalized atomic signal as a function of the rotation angle of the half-wave plate controlling the polarization direction of the imaging beam. The blue line shows a sinusoidal fit to the data with a fitted oscillation period of 89.2(2)°.

7.3.3 Atom Number Calibration

With a working imaging scheme, a preliminary calibration of the measured atom number can be performed using the method of Reinaudi *et al.* [162].

The intensity attenuation of the imaging beam can be described by the Lambert-Beer law, which for a two-level atom interacting with resonant light and including saturation effects is given by

$$\frac{\mathrm{d}I}{\mathrm{d}x} = -\frac{\sigma_0 n(x)}{1 + I/I_{\mathrm{sat}}} I. \tag{7.11}$$

Here, $n(x)$ is the atomic density, $I_{\mathrm{sat}} = 1.75\,\mathrm{mW/cm^2}$ is the saturation intensity of the D2 line of ^{39}K [121], and $\sigma_0 = 3\lambda^2/2\pi$ is the resonant scattering cross section with λ the wavelength of the transition. Integrating

Eq. (7.11) along the x-direction yields the column density $\tilde{n}$,

$$\tilde{n}\sigma_0 = \ln\left(\frac{I_0}{I}\right) + \frac{I_0 - I}{I_{\text{sat}}}, \tag{7.12}$$

where $\tilde{n}\sigma_0$ is referred to as the optical density, and the probe image $I(x, y)$ contains the shadow cast by the atoms, while the reference image $I_0(x, y)$ contains only the probe beam.

In the method of Reinaudi *et al.* [162], the absorption imaging is calibrated by introducing an effective saturation intensity $I_{\text{sat}}^{\text{eff}} = \alpha^* I_{\text{sat}}$. Here, the correction factor α^* takes into account experimental factors causing the system to deviate from a simple two-level model, such as the multi-level structure of the atoms, and the polarization of the imaging light. With this correction factor, Eq. (7.12) takes the form

$$\tilde{n}\sigma_0 = \alpha^* \ln\left(\frac{I_0}{I}\right) + \frac{I_0 - I}{I_{\text{sat}}}, \tag{7.13}$$

and the calibration consists of determining α^* by imaging atomic clouds prepared with a constant optical density, while varying the intensity of the imaging light.

In practice, the calibration is performed by preparing thermal clouds of ^{39}K in the $|1, 1\rangle$ state at a large magnetic field of $\sim$ 390 G, which are imaged using the scheme presented in the previous section. The intensity of the imaging beam is varied, while the absorbed number of photons is held constant by adjusting the exposure time accordingly between 18 and 228 µs.

The intensities $I(y, z)$ and $I_0(y, z)$ are extracted for each pixel (y, z) within a region of interest (ROI), and the correction parameter is determined from a fit of Eq. (7.13) to the data, where the three terms have been summed across the ROI

$$\sum_{\text{ROI}} \tilde{n}(y, z)\sigma_0 = \alpha^* \sum_{\text{ROI}} \ln\left(\frac{I_0(y, z)}{I(y, z)}\right) + \sum_{\text{ROI}} \frac{I_0(y, z) - I(y, z)}{I_{\text{sat}}}. \tag{7.14}$$

The fit parameters are thus α^* and the sum of the optical density across the region of interest $\sum_{\text{ROI}} \tilde{n}(y, z)\sigma_0$.

The calibration data is shown in Fig. 7.7, together with the fit of Eq. (7.14), which yields a correction factor of $\alpha^* = 3.6(8)$. The total atom number can be determined from the other fit parameter as $N = A_{\text{px}} \sum_{\text{ROI}} \tilde{n}(y, z) = 3.6(5) \times 10^5$, where A_{px} is the pixel area in the imaging plane of the atoms.

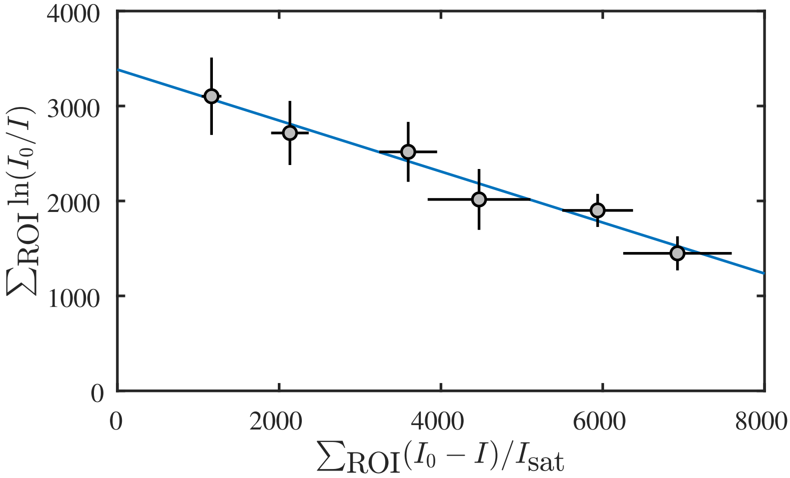

FIGURE 7.7: Preliminary calibration of the atom number using the method of Reinaudi *et al.* [162]. The intensity of the imaging beam I_0 was varied while the absorbed number of photons was held constant by adjusting the exposure time accordingly. The line shows a fit of Eq. (7.14) to the data, which yields the correction factor $\alpha^* = 3.6(8)$.

7.3.4 Magnetic Field Calibration

In order to accurately address the Feshbach resonance at 402.7 G, the magnetic field must be calibrated in this region. The magnetic field is typically inferred from radiofrequency spectroscopy measurements on cold thermal clouds, performed between the $|1,-1\rangle$ and $|1,0\rangle$ states as described in Sec. 4.2.4. In this method, the state composition after the radiofrequency pulse is determined by applying a magnetic field gradient during TOF to separate the states such that they can be analysed separately.

At a magnetic field of 69 G, where the new imaging scheme takes place, the splittings between the $F = 1$ states are too large to simultaneously image all components, and the usual procedure cannot be applied. Instead, since the repump light is *only* resonant with the $|1,1\rangle$ state, a successful transfer to another state results in a smaller number of evaluated atoms.

In practice, the calibration is performed by ramping the current in the Helmholtz coils to the target value over 250 ms after performing the rapid adiabatic passage described in Sec. 7.3.1. Here, the $|1,1\rangle \rightarrow |1,0\rangle$ transition

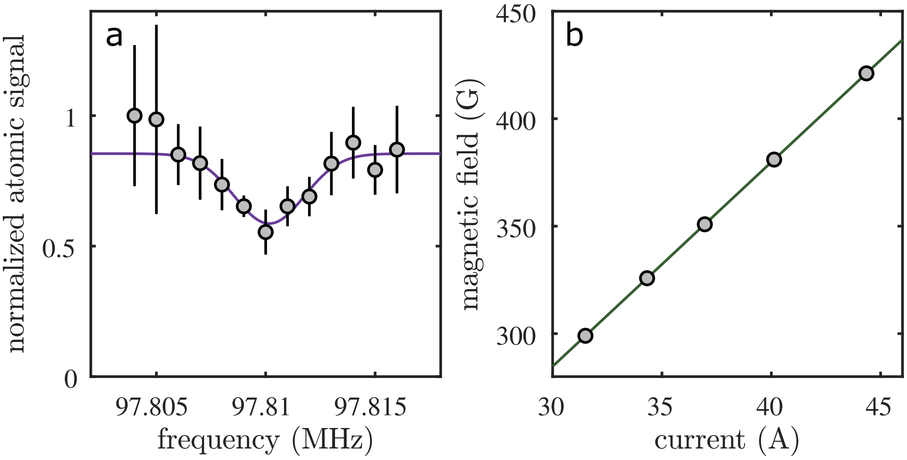

Figure 7.8: Magnetic field calibration at high currents. (a) Typical spectroscopic signal from driving the $|1,1\rangle$ to $|1,0\rangle$ transition. The normalized atomic signal of the $|1,1\rangle$ state is shown as a function of the applied radio frequency, and the purple line is a Gaussian fit to the data. The data corresponds to a Helmholtz current of 40.13 A. The magnetic field is determined from the centre frequency of the Gaussian fit using the Breit-Rabi formula (Eq. (4.4)). (b) Magnetic field calibration. The magnetic fields determined from the spectroscopic measurements are shown as a function of the Helmholtz current, together with a linear fit to the data. The error bars are smaller than the markers.

is addressed using a square rf pulse of 250 µs duration, and subsequently, the atoms are imaged as described in Sec. 7.3.2.

Figure 7.8(a) shows typical spectroscopic data for a Helmholtz current of 40.13 A. The normalized atomic signal is shown as function of the applied radio frequency, together with a Gaussian fit to the data. The magnetic field is determined from the centre frequency using the Breit-Rabi formula (Eq. (4.4)). Figure 7.8(b) shows the resulting magnetic fields from the spectroscopy data as a function of the Helmholtz current. The line shows a linear fit to the data, which gives the magnetic field calibration. The fit yields a slope of 9.501(2) G/A and an offset of -0.29(8) G.

7.3.5 BEC production

Bose-Einstein condensation is typically performed at a magnetic field where the scattering length is in the range of 100 to 200 a_0. For the Feshbach resonance of the $|1,1\rangle$ state at 402.7 G, this corresponds to a magnetic field range of $\sim$ 391 to 396 G.

After transfer to the $|1,1\rangle$ state, the magnetic field is ramped to its target value over 250 ms. From here the powers in the trapping beams are lowered in exponential ramps with a total duration of $\sim$ 7 to 10 seconds, which, depending on the final trap depth, results in BECs consisting of $\sim 1 \times 10^5$ atoms. In Fig. 7.9(a) a processed absorption image of such a BEC is shown, which was produced at a homogenous magnetic field of 395.9 G corresponding to 193 a_0. Figure 7.9(b) shows the optical density integrated along the vertical direction fitted with a bimodal model, where the thermal part is shown in orange, and the sum of the thermal and BEC distributions is shown in red.

7.4 Preparatory Experiments with ^{39}K at Large Magnetic Fields

With a working scheme for BEC production and a calibrated magnetic field and imaging system, initial experiments towards a measurement of the three-body scattering hypervolume can now be performed. In this section, two preliminary experiments are presented and discussed. In the first, an experimental verification of the expected magnetic field for the location of the zero-crossing is attempted, while in the second, a measurement of the three-body loss coefficient in the vicinity of the Feshbach resonance is presented.

7.4.1 Location of the Zero-crossing

Performing a measurement of the three-body scattering hypervolume requires precise knowledge of the magnetic field where $a = 0$. For other Feshbach resonances, this magnetic field has been determined experimentally by measuring the point of least efficient rethermalization. This has

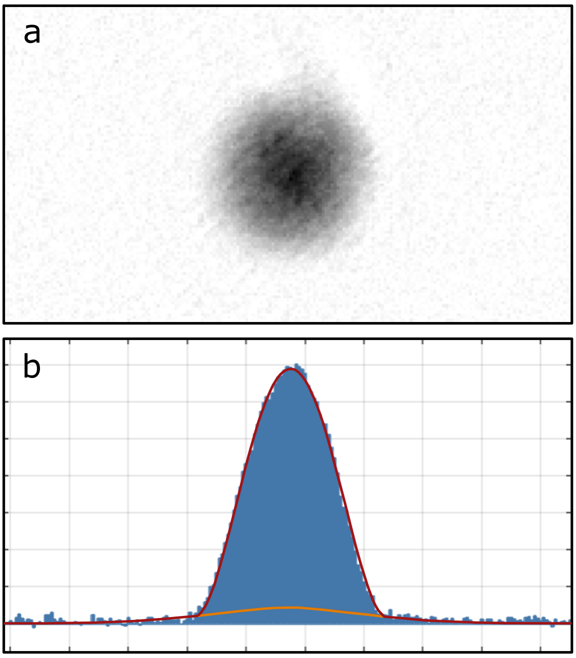

FIGURE 7.9: Absorption image of a quasi-pure Bose-Einstein condensate in the $|1,1\rangle$ state consisting of 1.1×10^5 atoms after 16 ms of time-of-flight expansion. (a) Absorption image after processing. (b) Integrated optical density (blue) and a bimodal fit to the data. The thermal part of the fit is shown in orange, and the bimodal distribution containing both the thermal and condensed parts is shown in red.

been done by performing evaporative cooling of thermal clouds at different magnetic fields and measuring the resulting temperature. The location of the zero-crossing can then be determined by a Gaussian fit to the temperature as a function of the magnetic field strength [85, 240].

A more sophisticated method was first used by Thalhammer *et al.* [241] and has previously been employed to measure the zero-crossing of both interspecies [100] and interstate [48] resonances using this apparatus. During thermalization, the temperature decreases exponentially with a rate proportional to the elastic scattering cross section, which scales with a^2 as shown in Sec. 2.2. The final temperature after a fixed thermalization time is thus given by [241]

$$T = A_1 + A_2 \exp\left(-A_3 a^2(B)\right), \tag{7.15}$$

where A_i, $i = 1, 2, 3$, contain information about the temperature and rethermalization rates, and $a(B)$ is given by Eq. (7.5).

In a first effort to determine the location of the zero-crossing experimentally, evaporative cooling of atoms in the $|1,1\rangle$ state was performed in the ODT at different magnetic field strengths with a final trap depth of $U_0/k_\mathrm{B} \sim 2\,\mu\mathrm{K}$. The resulting temperature of the thermal cloud is shown as a function of magnetic field in Fig. 7.10(a), however, the data features no peak to be identified as the location of the zero-crossing.

An alternative experiment was therefore performed in the following way: First, initial evaporative cooling was performed at a magnetic field of 392.6 G corresponding to $a = 120\,a_0$ until a final trap depth of $U_0/k_\mathrm{B} \sim 3\,\mu\mathrm{K}$. Here, the magnetic field was ramped to its target value over a 10 ms duration and after 5 ms of hold time, the powers in the trapping beams were abruptly lowered yielding a trap depth of $U_0/k_\mathrm{B} \sim 0.6\,\mu\mathrm{K}$. The sudden reduction of the potential depth results in the most energetic atoms leaving the trap, which corresponds to cutting away the high-velocity tail of the Maxwell-Boltzmann distribution for the atomic velocities. Afterwards, the sample was held in the trap for a duration of 1 second, where the system was allowed to rethermalize, before subsequent TOF expansion and absorption imaging.

The final temperature after the experimental procedure is shown as function of the magnetic field in Fig. 7.10. As expected, the evaluated temperature decreases for higher magnetic fields as the rethermalization becomes more efficient with increasing scattering length, and for lower fields there is a weak signature of a peak in the temperature. A fit of Eq. (7.15) to the data is shown, where the coefficients A_i, and the width of the Feshbach resonance Δ enter as free parameters. The fit yields a width parameter of $\Delta = -59(5)\,\mathrm{G}$, which differs from the expected width of $\Delta = -52\,\mathrm{G}$ [83]. The data, however, only features a very weak signature of a peak, and the discrepancy is therefore not surprising. The peak could potentially be made narrower by increasing the rethermalization time, which would amplify the effect of the small differences in scattering length around the zero-crossing. When characterizing the interstate Feshbach resonance at 114 G for scattering between atoms in the

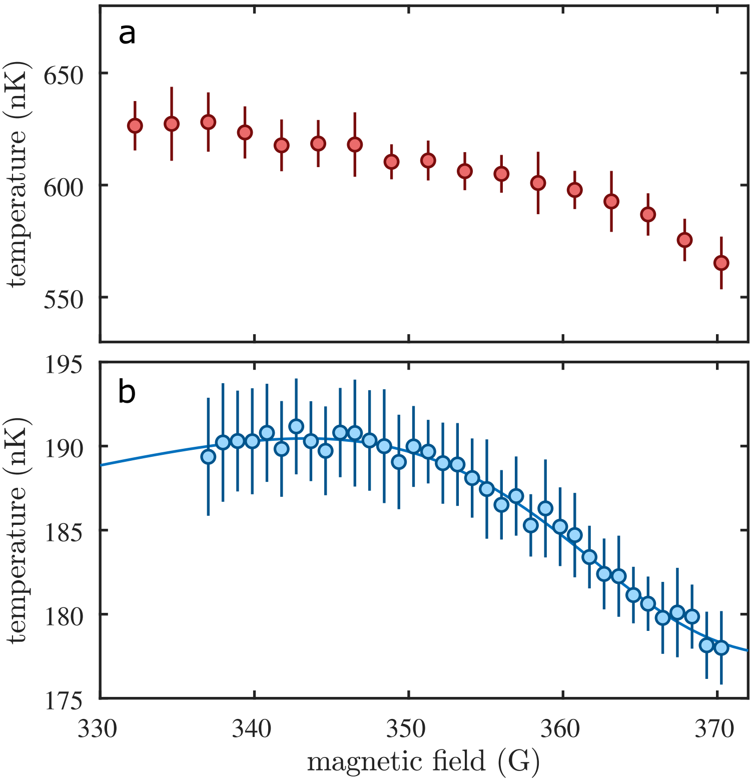

Figure 7.10: Rethermalization measurement in the vicinity of the zero-crossing. The final temperature of the sample as a function of magnetic field is shown using two different methods. (a) The sample was evaporately cooled at different magnetic fields until a final trap depth of $U_0/k_B \sim 2\,\mu\mathrm{K}$. (b) The depth of the trap potential was abruptly reduced, and the sample was allowed to rethermalize for 1 second in the new trap. The line shows a fit of Eq. (7.15) to the data which yields a width parameter of $\Delta = -59(5)\,\mathrm{G}$ for the Feshbach resonance.

$|1,-1\rangle$ and $|1,0\rangle$ states, a rethermalization time of 5 seconds was necessary in to get a sufficiently sharp peak at the zero-crossing [87]. The measurement of the interstate zero-crossing used another method than the one employed here, nonetheless, increasing the hold time after lowering the trap depth is an obvious next step.

Note that at this point, it is unclear to which extend the three-body scattering hypervolume influences the rethermalization in the vicinity of $a = 0$. However, since the probability for three atoms to interact scales with the density cubed, three-body interactions are likely to have negligible effects on the dilute thermal clouds.

Alternatively, the position of the zero-crossing (and possibly the size of D) could be determined from measurements of the size of the condensate. This was done using ^{39}K by Roati *et al.* [226], where the minimal size after TOF expansion was identified with the zero-crossing of the scattering length. A similar experiment was used to measure the influence of the magnetic dipole interaction on a ^{7}Li BEC, where phase-contrast imaging was employed to measure the in-trap size of the condensate [230].

7.4.2 Loss Measurements

A complete simulation of the dynamics of the system requires knowledge of the three-body loss coefficient, which corresponds to the imaginary part of D through Eq. (7.3). With a known value of $\mathrm{Im}(D)$ the system dynamics can be simulated for different values of $\mathrm{Re}(D)$ and a comparison of experiment and simulation can thus be used to infer the size of $\mathrm{Re}(D)$.

The three-body loss rate can be determined by measuring the evolution in the atom number and temperature as a function of hold time in the trap, and this method has been used extensively in the context of Efimov physics, where the presence of an Efimov state results in an increased three-body loss coefficient [85, 89, 135, 136, 242].

In an inhomogeneous system, the loss rate of the atom number can be determined by integrating the local three-body loss rate [88] over the sample. For a thermal cloud, the density distribution is given by the temperature T and the geometric mean of the trap frequencies ω_0, and the atom number thus follows the differential equation [88]

$$\frac{\mathrm{d}N}{\mathrm{d}t} = -\gamma \frac{N^3}{T^3}, \tag{7.16}$$

where $\gamma = L_3(m\omega_0^2/2\pi k_B)^3/\sqrt{27}$.

Since three-body recombination primarily results in losses from the centre of the trap where the density is highest, the atomic cloud experiences *anti-evaporation* heating. Furthermore, if the recombination products remain trapped, the released binding energy contributes with *recombination heating*. Including both effects, the differential equation for the temperature becomes

$$\frac{\mathrm{d}T}{\mathrm{d}t} = \gamma \frac{N^2}{T^3} \frac{T + T_\mathrm{h}}{3}, \tag{7.17}$$

where $k_B T_\mathrm{h}$ is the energy gained from recombination heating per lost atom.

The loss coefficient can be determined from experimental data by numerically solving the coupled differential equations of Eqs. (7.16) and (7.17) and comparing the solution to the data. In practice this is done by performing a least-squares fit of the numerically determined solution to the data with the initial atom number N_0, initial temperature T_0, the recombination heat T_h and the three-body loss coefficient L_3 entering as free parameters

A preliminary loss measurement was performed at a magnetic field of 400.7 G corresponding to $a \sim 700\, a_0$. The atomic sample was evaporatively cooled until a trap depth of $U_0/k_B \sim 2\,\mu\mathrm{K}$ after which the potential depth was increased to $U_0/k_B \sim 4\,\mu\mathrm{K}$ in order to stop further evaporative cooling. Subsequently, the sample was held in the trap for a variable time allowing three-body recombination to take place, before TOF expansion and absorption imaging.

The results of the loss measurement is shown in Fig. 7.11 with panels (a) and (b) showing the atom number and temperature as a function of time, respectively. With increasing hold time, the atom number decreases due to three-body recombination, while the temperature increases due to anti-evaporation and recombination heating. The apparent settling of the temperature at $\sim 400\,\mathrm{nK}$ could indicate the onset of evaporative cooling as the temperature matches the typical 1/10 ratio of the temperature to the trap depth for successfully confining atoms in an ODT. The lines show a fit of the solution to the coupled differential equations of Eqs. (7.16) and (7.17) as described above. The data marked by open circles have been excluded from the fit to avoid the influence of evaporative cooling. The fit yields $T_\mathrm{h} = 0.5(1)\,\mu\mathrm{K}$ and a three-body loss coefficient $L_3 = 2.1(2) \times 10^{-24}\,\mathrm{cm}^6\mathrm{s}^{-1}$,

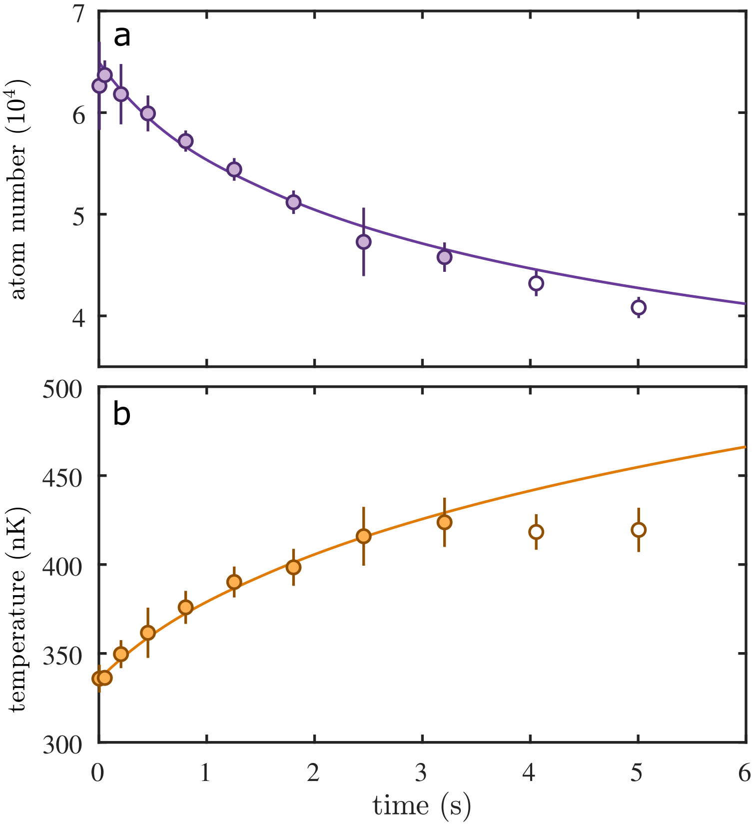

FIGURE 7.11: Measurement of the three-body loss coefficient at a magnetic field of 400.7 G corresponding to $a \sim 700\, a_0$. (a) Atom number and (b) temperature as a function of hold time in the optical dipole trap. The lines show a fitted solution to the coupled differential equations of Eqs. (7.16) and (7.17). The data marked by open circles have been excluded from the fit, since the settling of the temperature indicated the onset of evaporation cooling. The fit yields a recombination heat of $T_\mathrm{h} = 0.5(1)\,\mu\mathrm{K}$ and a three-body loss coefficient of $L_3 = 2.1(2) \times 10^{-24}\,\mathrm{cm}^6\mathrm{s}^{-1}$.

which has the same order of magnitude as the value measured by Zaccanti *et al.* [89] using the same state and magnetic field.

For smaller interaction strengths, initial measurements using thermal clouds have proven unsuccessful since the three-body recombination rate is too low to observe a significant loss in the atom number within a realistic experimental duration. For low and vanishing scattering lengths, the loss coefficient therefore has to be measured by observing three-body recombination losses in a BEC as done for $a < 600\ a_0$ by Zaccanti *et al.* [89].

7.5 Summary and Outlook

In this chapter, preparatory work for a new experiment using a ^{39}K BEC with vanishing s-wave scattering length was presented, with the aim of measuring the three-body scattering hypervolume D.

Initial simulations of the system were carried out, and the results agreed with the analytical results of Mestrom *et al.* [71] and showed how the monopole oscillation frequency of the system serves as a strong probe of the three-body scattering hypervolume. Further simulations could explore how the system responds to different methods of initializing the oscillations when the effect of losses is included. Furthermore, it will be interesting to simulate the system response to a modulation of the trapping potential, and evaluate whether this method provides a clearer experimental signal than oscillation measurements, which are strongly influenced by losses. A third set of simulations could investigate the in-trap and post-TOF sizes of the BEC to evaluate of there is a measurable difference in sizes compared to calculations excluding three-body interactions.

On the experimental side, ^{39}K BECs were successfully produced at the large magnetic field strengths necessary to address the zero-crossing of the scattering length. A new imaging scheme with the quantization axis in the vertical direction was implemented, and a preliminary calibration of the imaging system was performed. Following this, the magnetic field was calibrated in the regime of the Feshbach resonance, and initial attempts of locating the zero-crossing experimentally were presented. Finally, an example measurement of the three-body loss coefficient in the vicinity of the Feshbach resonance was performed.

The next experimental steps will consist of improving the measurements presented in Sec. 7.4 to determine the magnetic field of the zero-crossing and the three-body loss coefficient. With these parameters determined, the stage is set for performing oscillation measurements at $a = 0$. By comparing the experimental measurements to simulations including the imaginary part of D through the determined three-body loss coefficient, it should be possible to infer the size of the real part of the three-body scattering hypervolume and compare to the results of Mestrom *et al.* [71].

CHAPTER 8

Conclusion and Outlook

In this thesis, the work performed during my PhD studies was presented. The project considered three separate research directions, which were all pursued using BECs of ^{39}K with tunable interactions.

In Ch. 5, the dynamical evolution of impurities interacting with a BEC was investigated by using an interferometric method to track the state evolution. This enabled measuring the evolution of the system from a coherent superposition state into polaronic quasiparticles. Across the investigated interaction strengths, good agreement was found between the experimental results and theoretical predictions, which highlights the increasing understanding of polaron physics.

The experimental realization of a LHY fluid was presented in Ch. 6. By comparing the measured oscillation frequency of the system with detailed numerical simulations, it was possible to verify the creation of a LHY fluid, where the interactions are governed by quantum fluctuations. The monopole oscillation frequency of the system was investigated as a function of the LHY interaction strength and showed excellent agreement with the theoretical predictions. Furthermore, the measured oscillation frequency was found to be stable against variations around the ideal magnetic field and initial atom number ratio, showing that quantum fluctuations dominate the interactions in a regime around the ideal values. The results pave the way for new quantum simulation experiments and measurements of even higher order effects.

In Ch. 7, progress towards a new experiment strongly related to the LHY fluid experiment was presented. Here, the aim is measure the three-body scattering hypervolume through measurements of the collective excitations at the magnetic field where the s-wave scattering length vanishes. For ^{39}K, this point is located at large magnetic field strengths, which necessitates changing the experimental procedure compared to the previous experiments. Within the PhD project, BECs of ^{39}K were created at the required magnetic fields, and the stage is therefore set for these experiments.

In addition to the ongoing work towards a measurement of the three-body scattering hypervolume, several other research directions are being pursued which are discussed below.

Impurity Dynamics

Together with the spectroscopic measurements [48–50, 138], the interferometric experiments presented in this thesis contribute to a complete picture of the Bose polaron in both frequency and time domain. A new article is in preparation where the timescales of polaron formation, decay, and the different probing techniques are compared [243]. Moreover, the polaron energy is extracted from the interferometric data, and a first measurement of impurity dynamics with strongly repulsive impurity-medium interactions is presented. Further investigations could explore weaker repulsive interactions, where it should be possible to observe a quantum beat between the two polaron branches, or a measurement of the quasiparticle residue through Rabi oscillations as was done for the Fermi polaron [42].

Bipolarons

Even without significant direct interactions between the impurities, bosonic polarons may interact by exchanging density fluctuations in the BEC [244]. These polaron-polaron interactions can lead to the formation of a bound state named a bipolaron, which has been investigated theoretically for weak [245] and strong interactions [196]. Importantly, for strong interactions, the bipolaron energy is shifted significantly compared to that of the polaron, and a spectroscopic measurement of the bipolaron energy is therefore currently pursued.

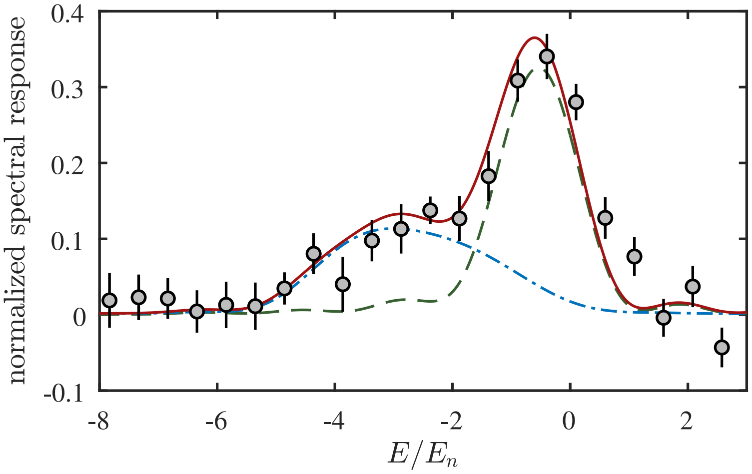

FIGURE 8.1: Ejection spectrum measured for an impurity-medium interaction strength of $1/k_n a = -0.12$ and a $30\,\mu s$ evolution time. The measured normalized spectral response is shown as circles, and the red line shows a fitted line shape function, which includes additional broadening from the inhomogeneous density distribution and finite length of the spectroscopy pulse. The contribution from polarons is shown by the dashed green, while the part associated with bipolarons is shown in dash-dotted blue.

Until now, the most promising results have employed the following technique: An initial imbalanced superposition state is first created using a short rf pulse as in the interferometric experiments. In a following variable evolution time, polarons and bipolarons are allowed to dynamically form, before a spectroscopy pulse ejects atoms out of the bipolaron state and into a third state. A typical spectroscopy signal using this method is shown in Fig. 8.1 and consists of a main peak due to the ejection of polarons, and a shoulder which is tentatively associated with bipolarons. A physically motivated line shape model (red line) containing contributions from both polarons (dashed green) and bipolarons (dash-dotted blue) is fitted to data and can be used to extract the bipolaron energy. Further details on these experiments and the fitting procedure are out of the scope of this work, but can be found in the thesis of Magnus G. Skou [163].

Box Potential

The above-mentioned experiments all suffer from complications due to the inhomogeneous density distribution present in the harmonic oscillator potential. For interferometric measurements, the inhomogeneous density contributes with an additional decoherence mechanism, whereas spectroscopic signals are broadened due to the density dependence of the polaron and bipolaron energies.

This effect can be eliminated by the use of a so-called box trap [198], which for BECs with a sufficiently large scattering length, results in a uniform density distribution. Such a box trap can be constructed using laser light that is blue-detuned compared to an atomic transition, which results in a repulsive potential as explained in Sec. 3.7. A typical configuration consists of a cylindrical trap geometry, which can be realized using a hollow tube beam and two end caps [246–248]. Experiments on two-dimensional systems have similarly been realized using a hollow beam and a tight optical lattice [249, 250]. Common to these experiments is the need to produce a hollow beam. This can be done actively using programmable spatial light modulators [246] or by "painting" a time-averaged potential [251], or via passive components such as custom-made masks [249] and axicons [247, 248, 250, 252]. The possibility of constructing a cylindrical beam using the axicon setup of Hueck *et al.* [250] has been investigated in the Master's thesis of Anders P. Hansen [253], and a 10 W laser with a wavelength of 532 nm has been purchased for providing the necessary light.

In addition to the potential provided by the light beams, gravity contributes with a linear potential in the vertical direction. In order to create a flat-bottomed three-dimensional potential, the effect of gravity must therefore be cancelled using a linear potential with opposite gradient. This can be achieved optically by creating a time-averaged potential for the atoms using acousto-optic deflectors [58, 254], by using a magnetic field gradient [246, 247], or via a static electric field gradient in the case of polar molecules [248].

In order to perform the experiments on impurity physics, the following criteria must be fulfilled: First, the employed medium state must have a positive scattering length to enable stable BEC production. Secondly, the scattering length of the medium atoms must be sufficiently large that the

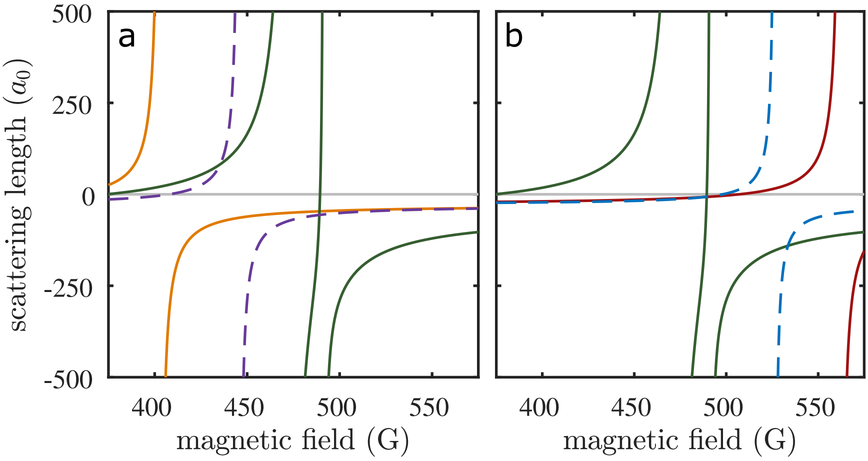

FIGURE 8.2: Feshbach resonance structure relevant for impurity physics using ^{39}K at large magnetic fields. The scattering lengths for different state combinations are shown as function of the magnetic field based on the calculated resonances structure of Lysebo and Veseth [146]. (a) Scattering length as a function of magnetic field for interactions between atoms in state $|1,1\rangle$ (solid orange), $|1,0\rangle$ (solid green), and between the states (dashed purple). (b) Scattering length as a function of magnetic field for interactions between atoms in state $|1,0\rangle$ (solid green), $|1,-1\rangle$ (solid red), and between the states (dashed blue).

mean-field repulsion results in a sizeable region of uniform density. Third, a Feshbach resonance between the impurity and medium states must be available for tuning the interaction strength, and finally, the employed states must all experience the same trapping potential, which puts an additional requirement on the gravity compensation.

The first method has the advantage, that the same Feshbach resonance at 113.8 G used in the previous experiments on impurity physics can be readily employed, since the “painted” potential can be made independent on the magnetic sublevels by using linearly polarized light [26]. However, at this magnetic field the scattering length of the usual medium state $|1,-1\rangle$ is only 9 a_0, which might be insufficient to realize a large region of uniform density with the available atom numbers. This could readily be investigated using GPELab to calculate the ground states of a BECs with varying atom number confined in a realistic box potential. Using this resonance is not possible if gravity compensation is to be performed with a magnetic field gradient, since the $|1,-1\rangle$ and $|1,0\rangle$ states have different magnetic moments in the vicinity of 113.8 G.

In order to use a magnetic field gradient for gravity compensation, one has to perform the experiments at a magnetic field strength, where the states are in the Paschen-Back regime. Here, the energies of the relevant states of the lowest hyperfine manifold of ^{39}K have the same linear dependence[1] proportional to $m_J B$, where B is the magnetic field strength and $m_J = -1/2$ (see Eq. (4.3)), which allows the same gradient to compensate for gravity for all of the states.

Fortunately, the $F = 1$ manifold of ^{39}K features Feshbach resonances in the Paschen-Back regime that allow experiments on impurity physics. These are shown in Fig. 8.2 for the $|1,1\rangle$ and $|1,0\rangle$ state combination in panel (a), while the $|1,0\rangle$ and $|1,-1\rangle$ combination is shown in panel (b). The $|1,0\rangle$ state could be used as the medium, since it features a scattering length $\sim$ 100 a_0 at the location of the resonance between the $|1,0\rangle$ and $|1,1\rangle$ states at $\sim$ 450 G as shown in panel (a). Alternatively, the Feshbach resonance structure of the $|1,0\rangle$ and $|1,-1\rangle$ states enables experiments with an approximately constant negative impurity-medium scattering length with a varying medium scattering length using the $|1,-1\rangle$ resonance at $\sim$ 560 G as shown in panel (b).

In summary, the presented results and discussed possibilities highlight the versatility of using ^{39}K in quantum gas experiments, since its Feshbach resonance structure enables a multitude of exciting research directions.

---

[1] There is a minor difference between the gradients caused by the nuclear magnetic moment, however, the corresponding nuclear g-factor is about a factor 1×10^{-4} smaller than g_J.

APPENDIX A

Supplementary Material – LHY Fluid Experiments

This appendix contains additional information for the LHY fluid experiments presented in Ch. 6. Appendix A.1 contains a table with the measured trap frequencies, in Appendix A.2 the effect of neglecting the LHY correction in the simulation is discussed, and in Appendix A.3 simulation results for an initially equal mixture are shown.

A.1 Measured Trap Frequencies

Table A.1 shows the measured trap frequencies used in the LHY fluid experiments along with the frequency differences with respect to the individual axes.

A.2 Effect of Neglecting the LHY Correction

In Fig. A.1 the simulated oscillations for $\delta a = 0$ are shown with (a-c) and without (d-f) including the LHY correction. The simulations were performed using a spherical trap with $\omega_0 = 2\pi \times 110.9\,\mathrm{Hz}$ and total atom number $N = 9.4 \times 10^4$ corresponding to the experiment of Sec. 6.4.2. The

Figure		$\omega_0/2\pi$ (Hz)	$(\omega'_x - \omega_0)/2\pi$ (Hz)	$(\omega'_y - \omega_0)/2\pi$ (Hz)	$(\omega'_z - \omega_0)/2\pi$ (Hz)
5.6	○	113.1(6)	3(1)	0.1(9)	−3.3(8)
	□	113.7(1)	4.8(2)	1.6(2)	−6(1)
	◇	115.3(4)	0.4(4)	−4(1)	3.5(4)
	▽	111.1(3)	1.1(8)	−3.5(6)	2.5(7)
5.6	△				
5.7	○	110.9(5)	1(1)	−4.2(9)	3(1)
5.8	○				

TABLE A.1: Measured trap frequencies corresponding to the experiments of Ch. 6. The geometric mean are given along with the deviations from the mean along each axis.

results for the components in the $|1\rangle$ and $|2\rangle$ states are shown in solid orange and dashed purple, respectively. The upper panels show the simulated root-mean-square radii without including losses. Panel (a) thus corresponds to a LHY fluid undergoing large amplitude oscillations due to the experimental preparation method, while panel (b) shows the evolution of a system which starts out as non-interacting due to the cancellation of mean-field interactions. Despite the irregular oscillations, fitting Eq. (6.15) to the simulated radii yields an oscillation frequency of $\omega/\omega_0 \sim 2$ as evident from the dotted orange line in Fig. 6.10. The simulated radii when including losses are shown in the middle panels of Fig. A.1, and the lower panels show the corresponding evolutions in the atom number. Panel (b) thus shows the radial evolution of a system, which starts out as a LHY fluid, but where the mean-field interactions increase as a consequence of the cascading inelastic losses evident in panel (c). For the simulations in panel (e), the repulsive LHY interactions are not present to counteract the mean-field energy, which appears due to the losses. These cause the component in the $|2\rangle$ state to experience an increasing mean-field attraction, which further amplifies the losses and causes the population to decrease rapidly as shown in panel (f). The component in the $|1\rangle$ state consequently experiences an increasing repulsion, which causes a violent expansion after the first contraction and results in a prominent kink in the simulated radius. The complicated dynamics of the wave functions result in bad fits of Eq. (6.15) and the orange lines in Fig. 6.10 therefore only resemble the qualitative behaviour of the monopole oscillation frequency.

A.3 Equal Mixture Simulations

In Fig. A.2 simulated oscillations for $\delta a = 0$ are shown for an equal mixture of the components in states $|1\rangle$ (solid orange) and $|2\rangle$ (dashed purple). The simulations were performed using a spherical trap with $\omega_0 = 2\pi \times 110.9\,\mathrm{Hz}$ and total atom number $N = 9.4 \times 10^4$ corresponding to the experiment of Sec. 6.4.3. Panel (a) shows the root-mean-square radii as a function of time without losses, and the radii including losses are shown in panel (b) with the corresponding evolution of the atom numbers in panel (c). The simulations correspond to the rightmost points of the dotted and solid blue lines of Fig. 6.11, respectively. The results without losses show the irregular oscillations of the component in the $|1\rangle$ state, which causes the steep decline in the extracted oscillation frequency in Fig. 6.11. This behaviour is not present for the simulations including losses, as the relative atom number N_2/N_1 is pulled towards lower values by the losses.

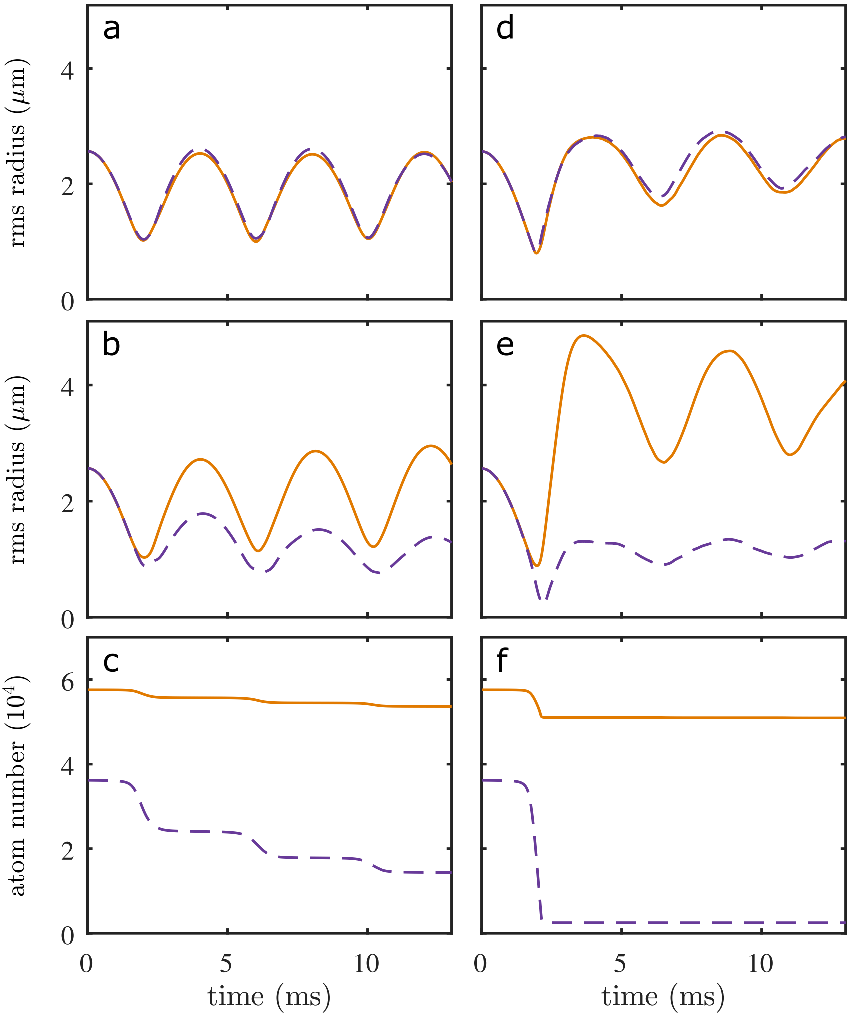

Figure A.1: Results of the dynamical two-component simulations for $\omega_0 = 2\pi \times 110.9$ Hz and $N = 9.4 \times 10^4$ corresponding to $U = 4.1$. Results for the components in the $|1\rangle$ and $|2\rangle$ states are shown in solid orange and dashed purple, respectively. The simulations were performed for $\delta a = 0$ correspond to the simulation data for this value in Fig. 6.10. The simulations were performed with (a-c) and without (d-f) including the LHY correction. The simulated root-mean-square radii are shown as a function of time excluding (upper panels) and including (middle panels) inelastic losses. The corresponding evolutions in the atom numbers for the simulations including losses are shown in the lower panels.

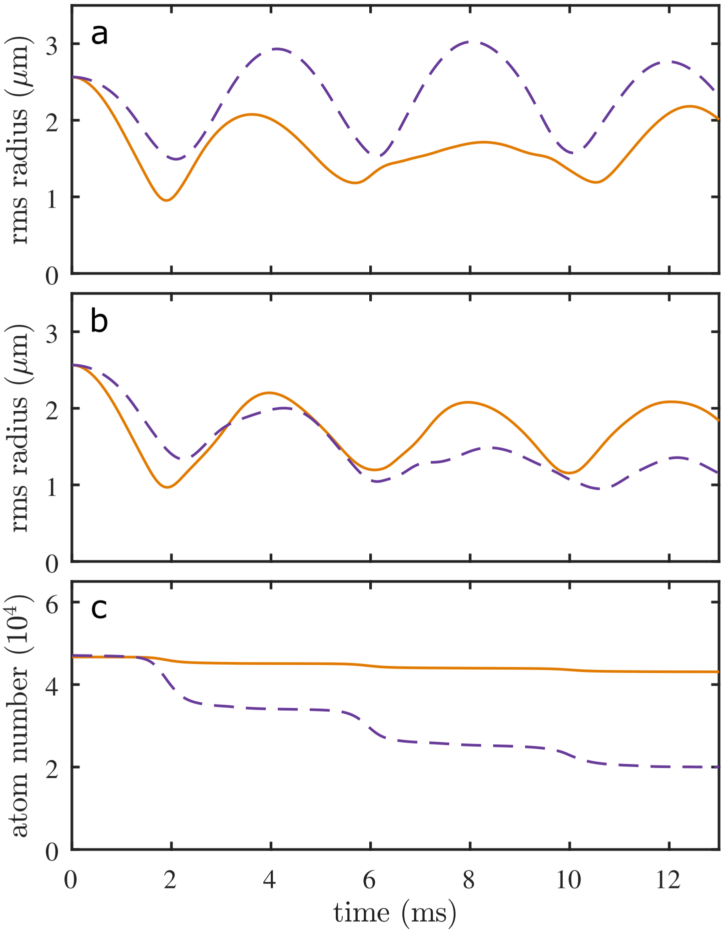

FIGURE A.2: Results of the dynamical two-component simulations for $\omega_0 = 2\pi \times 110.9\,\mathrm{Hz}$ and $N = 9.4 \times 10^4$ starting from an equal mixture of states $|1\rangle$ (solid orange) and $|2\rangle$ (dashed purple). (a) Simulated radii without including losses. (b-c) Simulated radii (b) and atom numbers (c) including inelastic losses.

Bibliography

[1] M. Planck, Zur Theorie des Gesetzes der Energieverteilung in Normalspectrum, Verh. Deutsch. Phys. Gesell. **2**, 237–245 (1900).

[2] A. Einstein, Über einem die Erzeugung und Verwandlung des Lichtes betreffenden heuristischen Gesichtspunkt, Annalen der physik **4** (1905).

[3] N. Bohr, On the constitution of atoms and molecules, The London, Edinburgh, and Dublin Philosophical Magazine and Journal of Science **26**, 1–25 (1913).

[4] A. H. Compton, A Quantum Theory of the Scattering of X-rays by Light Elements, Physical Review **21**, 483–502 (1923).

[5] C. Davisson and L. H. Germer, Diffraction of Electrons by a Crystal of Nickel, Physical Review **30**, 705–740 (1927).

[6] G. P. Thomson, The Diffraction of Cathode Rays by Thin Films of Platinum, Nature **120**, 802–802 (1927).

[7] I. Estermann and O. Stern, Beugung von Molekularstrahlen, Zeitschrift für Physik **61**, 95–125 (1930).

[8] E. Schrödinger, An Undulatory Theory of the Mechanics of Atoms and Molecules, Physical Review **28**, 1049–1070 (1926).

[9] M. Born, Zur Quantenmechanik der Stoßvorgänge, Zeitschrift für Physik **37**, 863–867 (1926).

[10] S. N. Bose, Plancks Gesetz und Lichtquantenhypothese, Zeitschrift für Physik **26**, 178–181 (1924).

[11] A. Einstein, Quantentheorie des einatomigen idealen Gases, SB Preuss. Akad. Wiss. phys.-math. Klasse (1924).

[12] C. J. Pethick and H. Smith, Bose–Einstein Condensation in Dilute Gases (Cambridge University Press, 2008).

[13] M. H. Anderson, J. R. Ensher, M. R. Matthews, C. E. Wieman, and E. A. Cornell, Observation of Bose-Einstein Condensation in a Dilute Atomic Vapor, Science **269**, 198–201 (1995).

[14] K. B. Davis, M. .-. Mewes, M. R. Andrews, N. J. van Druten, D. S. Durfee, D. M. Kurn, and W. Ketterle, Bose-Einstein Condensation in a Gas of Sodium Atoms, Physical Review Letters **75**, 3969–3973 (1995).

[15] C. C. Bradley, C. A. Sackett, J. J. Tollett, and R. G. Hulet, Evidence of Bose-Einstein Condensation in an Atomic Gas with Attractive Interactions, Physical Review Letters **75**, 1687–1690 (1995).

[16] B. DeMarco and D. S. Jin, Onset of Fermi Degeneracy in a Trapped Atomic Gas, Science **285**, 1703–1706 (1999).

[17] *The Nobel Prize in Physics 2001*, NobelPrize.org, `https://www.nobelprize.org/prizes/physics/2001/summary/` (visited on 07/23/2021).

[18] *Ultracold Atom News*, `https://ucan.physics.utoronto.ca/research-groups/` (visited on 07/23/2021).

[19] J. Bardeen and W. H. Brattain, The Transistor, A Semi-Conductor Triode, Physical Review **74**, 230–231 (1948).

[20] T. H. Maiman, Stimulated Optical Radiation in Ruby, Nature **187**, 493–494 (1960).

[21] A. G. J. MacFarlane, J. P. Dowling, and G. J. Milburn, Quantum technology: the second quantum revolution, Philosophical Transactions of the Royal Society of London. Series A: Mathematical, Physical and Engineering Sciences **361**, 1655–1674 (2003).

[22] T. D. Ladd, F. Jelezko, R. Laflamme, Y. Nakamura, C. Monroe, and J. L. O'Brien, Quantum computers, Nature **464**, 45–53 (2010).

[23] S. Pirandola, S. Pirandola, U. L. Andersen, L. Banchi, M. Berta, D. Bunandar, R. Colbeck, D. Englund, T. Gehring, C. Lupo, C. Ottaviani, J. L. Pereira, M. Razavi, J. S. Shaari, J. S. Shaari, M. Tomamichel, M. Tomamichel, V. C. Usenko, G. Vallone, P. Villoresi, and P. Wallden, Advances in quantum cryptography, Advances in Optics and Photonics **12**, 1012–1236 (2020).

[24] C. L. Degen, F. Reinhard, and P. Cappellaro, Quantum sensing, Reviews of Modern Physics **89**, 035002 (2017).

[25] R. Feynman, Simulating physics with computers, International Journal of Theoretical Physics **21** (1982).

[26] R. Grimm, M. Weidemüller, and Y. B. Ovchinnikov, Optical Dipole Traps for Neutral Atoms, in *Advances In Atomic, Molecular, and Optical Physics*, Vol. 42, edited by B. Bederson and H. Walther (Academic Press, Jan. 1, 2000), pp. 95–170.

[27] C. Chin, R. Grimm, P. Julienne, and E. Tiesinga, Feshbach resonances in ultracold gases, Reviews of Modern Physics **82**, 1225–1286 (2010).

[28] I. M. Georgescu, S. Ashhab, and F. Nori, Quantum simulation, Reviews of Modern Physics **86**, 153–185 (2014).

[29] I. Bloch, J. Dalibard, and S. Nascimbène, Quantum simulations with ultracold quantum gases, Nature Physics **8**, 267–276 (2012).

[30] C. Gross and I. Bloch, Quantum simulations with ultracold atoms in optical lattices, Science **357**, 995–1001 (2017).

[31] R. Blatt and C. F. Roos, Quantum simulations with trapped ions, Nature Physics **8**, 277–284 (2012).

[32] A. Aspuru-Guzik and P. Walther, Photonic quantum simulators, Nature Physics **8**, 285–291 (2012).

[33] S. A. Wilkinson and M. J. Hartmann, Superconducting quantum many-body circuits for quantum simulation and computing, Applied Physics Letters **116**, 230501 (2020).

[34] L. Landau, Über die Bewegung der Elektronen in Kristalgitter, Physikalische Zeitschrift der Sowjetunion **3**, 644–645 (1933).

[35] S. Pekar, Autolocalization of the electron in an inertially polarizable dielectric medium, Journal of Experimental and Theoretical Physics **16**, 335 (1946).

[36] L. Landau and S. Pekar, Effective mass of a polaron, Journal of Experimental and Theoretical Physics **18**, 419–423 (1948).

[37] E. Dagotto, Correlated electrons in high-temperature superconductors, Reviews of Modern Physics **66**, 763–840 (1994).

[38] R. F. Bishop, On the ground state of an impurity in a dilute fermi gas, Annals of Physics **78**, 391–420 (1973).

[39] A. Schirotzek, C.-H. Wu, A. Sommer, and M. W. Zwierlein, Observation of Fermi Polarons in a Tunable Fermi Liquid of Ultracold Atoms, Physical Review Letters **102**, 230402 (2009).

[40] S. Nascimbène, N. Navon, K. J. Jiang, L. Tarruell, M. Teichmann, J. McKeever, F. Chevy, and C. Salomon, Collective Oscillations of an Imbalanced Fermi Gas: Axial Compression Modes and Polaron Effective Mass, Physical Review Letters **103**, 170402 (2009).

[41] N. Navon, S. Nascimbène, F. Chevy, and C. Salomon, The Equation of State of a Low-Temperature Fermi Gas with Tunable Interactions, Science **328**, 729–732 (2010).

[42] C. Kohstall, M. Zaccanti, M. Jag, A. Trenkwalder, P. Massignan, G. M. Bruun, F. Schreck, and R. Grimm, Metastability and coherence of repulsive polarons in a strongly interacting Fermi mixture, Nature **485**, 615–618 (2012).

[43] M. Koschorreck, D. Pertot, E. Vogt, B. Fröhlich, M. Feld, and M. Köhl, Attractive and repulsive Fermi polarons in two dimensions, Nature **485**, 619–622 (2012).

[44] M. Cetina, M. Jag, R. S. Lous, J. T. M. Walraven, R. Grimm, R. S. Christensen, and G. M. Bruun, Decoherence of Impurities in a Fermi Sea of Ultracold Atoms, Physical Review Letters **115**, 135302 (2015).

[45] M. Cetina, M. Jag, R. S. Lous, I. Fritsche, J. T. M. Walraven, R. Grimm, J. Levinsen, M. M. Parish, R. Schmidt, M. Knap, and E. Demler, Ultrafast many-body interferometry of impurities coupled to a Fermi sea, Science **354**, 96–99 (2016).

[46] Z. Yan, P. B. Patel, B. Mukherjee, R. J. Fletcher, J. Struck, and M. W. Zwierlein, Boiling a Unitary Fermi Liquid, Physical Review Letters **122**, 093401 (2019).

[47] N. Darkwah Oppong, L. Riegger, O. Bettermann, M. Höfer, J. Levinsen, M. M. Parish, I. Bloch, and S. Fölling, Observation of Coherent Multiorbital Polarons in a Two-Dimensional Fermi Gas, Physical Review Letters **122**, 193604 (2019).

[48] N. B. Jørgensen, L. Wacker, K. T. Skalmstang, M. M. Parish, J. Levinsen, R. S. Christensen, G. M. Bruun, and J. J. Arlt, Observation of Attractive and Repulsive Polarons in a Bose-Einstein Condensate, Physical Review Letters **117**, 055302 (2016).

[49] M.-G. Hu, M. J. Van de Graaff, D. Kedar, J. P. Corson, E. A. Cornell, and D. S. Jin, Bose Polarons in the Strongly Interacting Regime, Physical Review Letters **117**, 055301 (2016).

[50] Z. Z. Yan, Y. Ni, C. Robens, and M. W. Zwierlein, Bose polarons near quantum criticality, Science **368**, 190–194 (2020).

[51] M. G. Skou, T. G. Skov, N. B. Jørgensen, K. K. Nielsen, A. Camacho-Guardian, T. Pohl, G. M. Bruun, and J. J. Arlt, Non-equilibrium quantum dynamics and formation of the Bose polaron, Nature Physics **17**, 731–735 (2021).

[52] M. G. Skou, T. G. Skov, N. B. Jørgensen, and J. J. Arlt, Initial Dynamics of Quantum Impurities in a Bose–Einstein Condensate, Atoms **9**, 22 (2021).

[53] N. B. Jørgensen, G. M. Bruun, and J. J. Arlt, Dilute Fluid Governed by Quantum Fluctuations, Physical Review Letters **121**, 173403 (2018).

[54] T. G. Skov, M. G. Skou, N. B. Jørgensen, and J. J. Arlt, Observation of a Lee-Huang-Yang Fluid, Physical Review Letters **126**, 230404 (2021).

[55] T. D. Lee, K. Huang, and C. N. Yang, Eigenvalues and Eigenfunctions of a Bose System of Hard Spheres and Its Low-Temperature Properties, Physical Review **106**, 1135–1145 (1957).

[56] D. S. Petrov, Quantum Mechanical Stabilization of a Collapsing Bose-Bose Mixture, Physical Review Letters **115**, 155302 (2015).

[57] C. R. Cabrera, L. Tanzi, J. Sanz, B. Naylor, P. Thomas, P. Cheiney, and L. Tarruell, Quantum liquid droplets in a mixture of Bose-Einstein condensates, Science **359**, 301–304 (2018).

[58] G. Semeghini, G. Ferioli, L. Masi, C. Mazzinghi, L. Wolswijk, F. Minardi, M. Modugno, G. Modugno, M. Inguscio, and M. Fattori, Self-Bound Quantum Droplets of Atomic Mixtures in Free Space, Physical Review Letters **120**, 235301 (2018).

[59] P. Cheiney, C. R. Cabrera, J. Sanz, B. Naylor, L. Tanzi, and L. Tarruell, Bright Soliton to Quantum Droplet Transition in a Mixture of Bose-Einstein Condensates, Physical Review Letters **120**, 135301 (2018).

[60] G. Ferioli, G. Semeghini, L. Masi, G. Giusti, G. Modugno, M. Inguscio, A. Gallemí, A. Recati, and M. Fattori, Collisions of Self-Bound Quantum Droplets, Physical Review Letters **122**, 090401 (2019).

[61] C. D'Errico, A. Burchianti, M. Prevedelli, L. Salasnich, F. Ancilotto, M. Modugno, F. Minardi, and C. Fort, Observation of quantum droplets in a heteronuclear bosonic mixture, Physical Review Research **1**, 033155 (2019).

[62] H. Kadau, M. Schmitt, M. Wenzel, C. Wink, T. Maier, I. Ferrier-Barbut, and T. Pfau, Observing the Rosensweig instability of a quantum ferrofluid, Nature **530**, 194–197 (2016).

[63] I. Ferrier-Barbut, H. Kadau, M. Schmitt, M. Wenzel, and T. Pfau, Observation of Quantum Droplets in a Strongly Dipolar Bose Gas, Physical Review Letters **116**, 215301 (2016).

[64] M. Schmitt, M. Wenzel, F. Böttcher, I. Ferrier-Barbut, and T. Pfau, Self-bound droplets of a dilute magnetic quantum liquid, Nature **539**, 259–262 (2016).

[65] L. Chomaz, S. Baier, D. Petter, M. J. Mark, F. Wächtler, L. Santos, and F. Ferlaino, Quantum-Fluctuation-Driven Crossover from a Dilute Bose-Einstein Condensate to a Macrodroplet in a Dipolar Quantum Fluid, Physical Review X **6**, 041039 (2016).

[66] F. Böttcher, J.-N. Schmidt, M. Wenzel, J. Hertkorn, M. Guo, T. Langen, and T. Pfau, Transient Supersolid Properties in an Array of Dipolar Quantum Droplets, Physical Review X **9**, 011051 (2019).

[67] L. Chomaz, D. Petter, P. Ilzhöfer, G. Natale, A. Trautmann, C. Politi, G. Durastante, R. M. W. van Bijnen, A. Patscheider, M. Sohmen, M. J. Mark, and F. Ferlaino, Long-Lived and Transient Supersolid Behaviors in Dipolar Quantum Gases, Physical Review X **9**, 021012 (2019).

[68] L. Tanzi, E. Lucioni, F. Famà, J. Catani, A. Fioretti, C. Gabbanini, R. N. Bisset, L. Santos, and G. Modugno, Observation of a Dipolar Quantum Gas with Metastable Supersolid Properties, Physical Review Letters **122**, 130405 (2019).

[69] S. Tan, Three-boson problem at low energy and implications for dilute Bose-Einstein condensates, Physical Review A **78**, 013636 (2008).

[70] W. Zwerger, Quantum-unbinding near a zero temperature liquid–gas transition, Journal of Statistical Mechanics: Theory and Experiment, 103104 (2019).

[71] P. M. A. Mestrom, V. E. Colussi, T. Secker, G. P. Groeneveld, and S. J. J. M. F. Kokkelmans, Van der Waals Universality near a Quantum Tricritical Point, Physical Review Letters **124**, 143401 (2020).

[72] D. J. Griffiths, Introduction to Quantum Mechanics, 2nd Edition (Pearson, 2004).

[73] W. Ketterle, D. Durfee, and D. Stamper-Kurn, Bose-Einstein Condensation in Atomic Gases, in *Proceedings of the International School of Physics "Enrico Fermi", Course CXL, edited by M. Inguscio, S. Stringari, and C. Wieman* (IOS Press, Amsterdam), pp. 67–176.

[74] D. V. Schroeder, An Introduction to Thermal Physics (Pearson, 1999).

[75] G. M. Bruun, Trapped ultra cold atoms and Bose-Einstein condensation, Lecture notes for the course "Quantum Physics with Cold Atoms and Ions", Aarhus University (2017).

[76] M. Naraschewski and D. M. Stamper-Kurn, Analytical description of a trapped semi-ideal Bose gas at finite temperature, Physical Review A **58**, 2423–2426 (1998).

[77] J. R. Ensher, D. S. Jin, M. R. Matthews, C. E. Wieman, and E. A. Cornell, Bose-Einstein Condensation in a Dilute Gas: Measurement of Energy and Ground-State Occupation, Physical Review Letters **77**, 4984–4987 (1996).

[78] P. E. Hodgson, E. Gadioli, and E. Gadioli Erba, Introductory Nuclear Physics (Oxford University Press, 2003).

[79] B. H. Bransden and C. J. Joachain, Physics of Atoms and Molecules, 2nd Edition (Pearson Education, 2003).

[80] H. Feshbach, A unified theory of nuclear reactions. II, Annals of Physics **19**, 287–313 (1962).

[81] U. Fano, Effects of Configuration Interaction on Intensities and Phase Shifts, Physical Review **124**, 1866–1878 (1961).

[82] S. Inouye, M. R. Andrews, J. Stenger, H.-J. Miesner, D. M. Stamper-Kurn, and W. Ketterle, Observation of Feshbach resonances in a Bose–Einstein condensate, Nature **392**, 151–154 (1998).

[83] C. D'Errico, M. Zaccanti, M. Fattori, G. Roati, M. Inguscio, G. Modugno, and A. Simoni, Feshbach resonances in ultracold ^{39}K, New Journal of Physics **9**, 223–223 (2007).

[84] R. Chapurin, X. Xie, M. J. Van de Graaff, J. S. Popowski, J. P. D'Incao, P. S. Julienne, J. Ye, and E. A. Cornell, Precision Test of the Limits to Universality in Few-Body Physics, Physical Review Letters **123**, 233402 (2019).

[85] S. Roy, M. Landini, A. Trenkwalder, G. Semeghini, G. Spagnolli, A. Simoni, M. Fattori, M. Inguscio, and G. Modugno, Test of the Universality of the Three-Body Efimov Parameter at Narrow Feshbach Resonances, Physical Review Letters **111**, 053202 (2013).

[86] L. Tanzi, C. R. Cabrera, J. Sanz, P. Cheiney, M. Tomza, and L. Tarruell, Feshbach resonances in potassium Bose-Bose mixtures, Physical Review A **98**, 062712 (2018).

[87] N. B. Jørgensen, Observation of Bose Polarons in a Quantum Gas Mixture (Aarhus University, 2018).

[88] T. Weber, J. Herbig, M. Mark, H.-C. Nägerl, and R. Grimm, Three-Body Recombination at Large Scattering Lengths in an Ultracold Atomic Gas, Physical Review Letters **91**, 123201 (2003).

[89] M. Zaccanti, B. Deissler, C. D'Errico, M. Fattori, M. Jona-Lasinio, S. Müller, G. Roati, M. Inguscio, and G. Modugno, Observation of an Efimov spectrum in an atomic system, Nature Physics **5**, 586–591 (2009).

[90] F. Dalfovo, S. Giorgini, L. P. Pitaevskii, and S. Stringari, Theory of Bose-Einstein condensation in trapped gases, Reviews of Modern Physics **71**, 463–512 (1999).

[91] S. L. Cornish, N. R. Claussen, J. L. Roberts, E. A. Cornell, and C. E. Wieman, Stable ^{85}Rb Bose-Einstein Condensates with Widely Tunable Interactions, Physical Review Letters **85**, 1795–1798 (2000).

[92] J. L. Roberts, N. R. Claussen, S. L. Cornish, E. A. Donley, E. A. Cornell, and C. E. Wieman, Controlled Collapse of a Bose-Einstein Condensate, Physical Review Letters **86**, 4211–4214 (2001).

[93] J. M. Gerton, D. Strekalov, I. Prodan, and R. G. Hulet, Direct observation of growth and collapse of a Bose–Einstein condensate with attractive interactions, Nature **408**, 692–695 (2000).

[94] E. A. Donley, N. R. Claussen, S. L. Cornish, J. L. Roberts, E. A. Cornell, and C. E. Wieman, Dynamics of collapsing and exploding Bose–Einstein condensates, Nature **412**, 295–299 (2001).

[95] T. Lahaye, J. Metz, B. Fröhlich, T. Koch, M. Meister, A. Griesmaier, T. Pfau, H. Saito, Y. Kawaguchi, and M. Ueda, d-Wave Collapse and Explosion of a Dipolar Bose-Einstein Condensate, Physical Review Letters **101**, 080401 (2008).

[96] P. A. Ruprecht, M. J. Holland, K. Burnett, and M. Edwards, Time-dependent solution of the nonlinear Schrödinger Equation for Bose-Condensed Trapped Neutral Atoms, Physical Review A **51**, 4704–4711 (1995).

[97] P. A. Altin, G. R. Dennis, G. D. McDonald, D. Döring, J. E. Debs, J. D. Close, C. M. Savage, and N. P. Robins, Collapse and three-body loss in a ^{87}Rb Bose-Einstein condensate, Physical Review A **84**, 033632 (2011).

[98] Y. Kagan, B. Svistunov, and G. Shlyapnikov, Effect of Bose condensation on inelastic processes in gases, ZhETF Pisma Redaktsiiu **42**, 169 (1985).

[99] E. A. Burt, R. W. Ghrist, C. J. Myatt, M. J. Holland, E. A. Cornell, and C. E. Wieman, Coherence, Correlations, and Collisions: What One Learns about Bose-Einstein Condensates from Their Decay, Physical Review Letters **79**, 337–340 (1997).

[100] L. Wacker, N. B. Jørgensen, D. Birkmose, R. Horchani, W. Ertmer, C. Klempt, N. Winter, J. Sherson, and J. J. Arlt, Tunable dual-species Bose-Einstein condensates of ^{39}K and ^{87}Rb, Physical Review A **92**, 053602 (2015).

[101] X. Antoine and R. Duboscq, GPELab, a Matlab toolbox to solve Gross–Pitaevskii equations I: Computation of stationary solutions, Computer Physics Communications **185**, 2969–2991 (2014).

[102] X. Antoine and R. Duboscq, GPELab, a Matlab toolbox to solve Gross–Pitaevskii equations II: Dynamics and stochastic simulations, Computer Physics Communications **193**, 95–117 (2015).

[103] W. Bao and Q. Du, Computing the ground state solution of Bose-Einstein condensates by a normalized gradient flow, SIAM Journal on Scientific Computing **25**, 1674–1697 (2004).

[104] P. Amara, D. Hsu, and J. E. Straub, Global energy minimum searches using an approximate solution of the imaginary time Schrödinger equation, The Journal of Physical Chemistry **97**, 6715–6721 (1993).

[105] N. Bogoliubov, On the theory of superfluidity, J. Phys **11**, 23 (1947).

[106] R. Lopes, C. Eigen, N. Navon, D. Clément, R. P. Smith, and Z. Hadzibabic, Quantum Depletion of a Homogeneous Bose-Einstein Condensate, Physical Review Letters **119**, 190404 (2017).

[107] D. A. Steck, Quantum and Atom Optics, available online at http://steck.us/teaching (revision 0.13.4, 24 September 2020).

[108] A. D. Cronin, J. Schmiedmayer, and D. E. Pritchard, Optics and interferometry with atoms and molecules, Reviews of Modern Physics **81**, 1051–1129 (2009).

[109] N. V. Vitanov, T. Halfmann, B. W. Shore, and K. Bergmann, Laser-Induced Population Transfer by Adiabatic Passage Techniques, Annual Review of Physical Chemistry **52**, 763–809 (2001).

[110] T. Lu, X. Miao, and H. Metcalf, Nonadiabatic transitions in finite-time adiabatic rapid passage, Physical Review A **75**, 063422 (2007).

[111] N. F. Ramsey, A New Molecular Beam Resonance Method, Physical Review **76**, 996–996 (1949).

[112] N. F. Ramsey, A Molecular Beam Resonance Method with Separated Oscillating Fields, Physical Review **78**, 695–699 (1950).

[113] A. D. Ludlow, M. M. Boyd, J. Ye, E. Peik, and P. O. Schmidt, Optical atomic clocks, Reviews of Modern Physics **87**, 637–701 (2015).

[114] T. W. Hänsch and A. L. Schawlow, Cooling of gases by laser radiation, Optics Communications **13**, 68–69 (1975).

[115] D. Wineland and H. Dehmelt, Proposed 10^{14} $\delta\nu/\nu$ laser fluorescence spectroscopy on Ti^+ mono-ion oscillator, Bull. Am. Phys. Soc. **20** (1975).

[116] D. J. Wineland, R. E. Drullinger, and F. L. Walls, Radiation-Pressure Cooling of Bound Resonant Absorbers, Physical Review Letters **40**, 1639–1642 (1978).

[117] S. Chu, L. Hollberg, J. E. Bjorkholm, A. Cable, and A. Ashkin, Three-dimensional viscous confinement and cooling of atoms by resonance radiation pressure, Physical Review Letters **55**, 48–51 (1985).

[118] J. Prodan, A. Migdall, W. D. Phillips, I. So, H. Metcalf, and J. Dalibard, Stopping Atoms with Laser Light, Physical Review Letters **54**, 992–995 (1985).

[119] E. L. Raab, M. Prentiss, A. Cable, S. Chu, and D. E. Pritchard, Trapping of Neutral Sodium Atoms with Radiation Pressure, Physical Review Letters **59**, 2631–2634 (1987).

[120] P. D. Lett, W. D. Phillips, S. L. Rolston, C. E. Tanner, R. N. Watts, and C. I. Westbrook, Optical molasses, JOSA B **6**, 2084–2107 (1989).

[121] T. G. Tiecke, Properties of Potassium, available online at https://www.tobiastiecke.nl (revision 1.03, June, 2019).

[122] D. A. Steck, Rubidium 87 D Line Data, available online at http://steck.us/alkalidata (revision 2.2.1, 21 November 2019).

[123] D. Sesko, C. G. Fan, and C. E. Wieman, Production of a cold atomic vapor using diode-laser cooling, JOSA B **5**, 1225–1227 (1988).

[124] P. D. Lett, R. N. Watts, C. I. Westbrook, W. D. Phillips, P. L. Gould, and H. J. Metcalf, Observation of Atoms Laser Cooled below the Doppler Limit, Physical Review Letters **61**, 169–172 (1988).

[125] Y. Shevy, D. S. Weiss, P. J. Ungar, and S. Chu, Bimodal speed distributions in laser-cooled atoms, Physical Review Letters **62**, 1118–1121 (1989).

[126] J. Dalibard and C. Cohen-Tannoudji, Laser cooling below the Doppler limit by polarization gradients: simple theoretical models, JOSA B **6**, 2023–2045 (1989).

[127] S. Chu, J. E. Bjorkholm, A. Ashkin, and A. Cable, Experimental Observation of Optically Trapped Atoms, Physical Review Letters **57**, 314–317 (1986).

[128] N. Winter, Creation of ^{39}K Bose-Einstein Condensates with Tunable Interaction (Aarhus University, 2013).

[129] L. J. Wacker, Few-body Physics with Ultracold Potassium Rubidium Mixtures (Aarhus University, 2015).

[130] G. Kleine-Bühning, Lange Kohärenzzeit optisch gefangener Ensembles (Leibniz Universität Hannover, 2011).

[131] J. Will, Symmetrieabhängige Frequenzverschiebungen in Atomuhren (Leibniz Universität Hannover, 2012).

[132] G. Kleine Büning, J. Will, W. Ertmer, C. Klempt, and J. Arlt, A slow gravity compensated atom laser, Applied Physics B **100**, 117–123 (2010).

[133] G. Kleine Büning, J. Will, W. Ertmer, E. Rasel, J. Arlt, C. Klempt, F. Ramirez-Martinez, F. Piéchon, and P. Rosenbusch, Extended Coherence Time on the Clock Transition of Optically Trapped Rubidium, Physical Review Letters **106**, 240801 (2011).

[134] A. Chu, J. Will, J. Arlt, C. Klempt, and A. M. Rey, Simulation of XXZ Spin Models Using Sideband Transitions in Trapped Bosonic Gases, Physical Review Letters **125**, 240504 (2020).

[135] L. J. Wacker, N. B. Jørgensen, D. Birkmose, N. Winter, M. Mikkelsen, J. Sherson, N. Zinner, and J. J. Arlt, Universal Three-Body Physics in Ultracold KRb Mixtures, Physical Review Letters **117**, 163201 (2016).

[136] L. J. Wacker, N. B. Jørgensen, K. T. Skalmstang, M. G. Skou, A. G. Volosniev, and J. J. Arlt, Temperature dependence of an Efimov resonance in ^{39}K, Physical Review A **98**, 052706 (2018).

[137] K. L. Lee, N. B. Jørgensen, I.-K. Liu, L. Wacker, J. J. Arlt, and N. P. Proukakis, Phase separation and dynamics of two-component Bose-Einstein condensates, Physical Review A **94**, 013602 (2016).

[138] L. A. Peña Ardila, N. B. Jørgensen, T. Pohl, S. Giorgini, G. M. Bruun, and J. J. Arlt, Analyzing a Bose polaron across resonant interactions, Physical Review A **99**, 063607 (2019).

[139] T. Kishimoto, J. Kobayashi, K. Noda, K. Aikawa, M. Ueda, and S. Inouye, Direct evaporative cooling of ^{41}K into a Bose-Einstein condensate, Physical Review A **79**, 031602 (2009).

[140] R. L. D. Campbell, R. P. Smith, N. Tammuz, S. Beattie, S. Moulder, and Z. Hadzibabic, Efficient production of large ^{39}K Bose-Einstein condensates, Physical Review A **82**, 063611 (2010).

[141] V. Gokhroo, G. Rajalakshmi, R. K. Easwaran, and C. S. Unnikrishnan, Sub-Doppler deep-cooled bosonic and fermionic isotopes of potassium in a compact 2D^{+}-3D mot set-up, Journal of Physics B: Atomic, Molecular and Optical Physics **44**, 115307 (2011).

[142] M. Landini, S. Roy, L. Carcagní, D. Trypogeorgos, M. Fattori, M. Inguscio, and G. Modugno, Sub-Doppler laser cooling of potassium atoms, Physical Review A **84**, 043432 (2011).

[143] M. Landini, S. Roy, G. Roati, A. Simoni, M. Inguscio, G. Modugno, and M. Fattori, Direct evaporative cooling of ^{39}K atoms to Bose-Einstein condensation, Physical Review A **86**, 033421 (2012).

[144] G. Breit and I. I. Rabi, Measurement of Nuclear Spin, Physical Review **38**, 2082–2083 (1931).

[145] A. Marte, T. Volz, J. Schuster, S. Dürr, G. Rempe, E. G. M. van Kempen, and B. J. Verhaar, Feshbach Resonances in Rubidium 87: Precision Measurement and Analysis, Physical Review Letters **89**, 283202 (2002).

[146] M. Lysebo and L. Veseth, Feshbach resonances and transition rates for cold homonuclear collisions between ^{39}K and ^{41}K atoms, Physical Review A **81**, 032702 (2010).

[147] F. Ferlaino, C. D'Errico, G. Roati, M. Zaccanti, M. Inguscio, G. Modugno, and A. Simoni, Feshbach spectroscopy of a K-Rb atomic mixture, Physical Review A **73**, 040702 (2006).

[148] A. Simoni, M. Zaccanti, C. D’Errico, M. Fattori, G. Roati, M. Inguscio, and G. Modugno, Near-threshold model for ultracold KRb dimers from interisotope Feshbach spectroscopy, Physical Review A **77**, 052705 (2008).

[149] C. Klempt, T. van Zoest, T. Henninger, O. Topic, E. Rasel, W. Ertmer, and J. Arlt, Ultraviolet light-induced atom desorption for large rubidium and potassium magneto-optical traps, Physical Review A **73**, 013410 (2006).

[150] L. G. Marcassa, G. D. Telles, S. R. Muniz, and V. S. Bagnato, Collisional losses in a K-Rb cold mixture, Physical Review A **63**, 013413 (2000).

[151] W. Ketterle, K. B. Davis, M. A. Joffe, A. Martin, and D. E. Pritchard, High densities of cold atoms in a dark spontaneous-force optical trap, Physical Review Letters **70**, 2253–2256 (1993).

[152] M. H. Anderson, W. Petrich, J. R. Ensher, and E. A. Cornell, Reduction of light-assisted collisional loss rate from a low-pressure vapor-cell trap, Physical Review A **50**, R3597–R3600 (1994).

[153] C. G. Townsend, N. H. Edwards, K. P. Zetie, C. J. Cooper, J. Rink, and C. J. Foot, High-density trapping of cesium atoms in a dark magneto-optical trap, Physical Review A **53**, 1702–1714 (1996).

[154] N. Radwell, G. Walker, and S. Franke-Arnold, Cold-atom densities of more than 10^{12} cm^{-3} in a holographically shaped dark spontaneous-force optical trap, Physical Review A **88**, 043409 (2013).

[155] N. Nemitz, F. Baumer, F. Münchow, S. Tassy, and A. Görlitz, Production of heteronuclear molecules in an electronically excited state by photoassociation in a mixture of ultracold Yb and Rb, Physical Review A **79**, 061403 (2009).

[156] S. Dutta, A. Altaf, J. Lorenz, D. S. Elliott, and Y. P. Chen, Interspecies collision-induced losses in a dual species ^{7}Li–^{85}Rb magneto-optical trap, Journal of Physics B: Atomic, Molecular and Optical Physics **47**, 105301 (2014).

[157] W. Ketterle and N. J. V. Druten, Evaporative Cooling of Trapped Atoms, in *Advances In Atomic, Molecular, and Optical Physics*, Vol. 37, edited by B. Bederson and H. Walther (Academic Press, Jan. 1, 1996), pp. 181–236.

[158] G. Modugno, G. Ferrari, G. Roati, R. J. Brecha, A. Simoni, and M. Inguscio, Bose-Einstein Condensation of Potassium Atoms by Sympathetic Cooling, Science **294**, 1320–1322 (2001).

[159] G. Modugno, M. Modugno, F. Riboli, G. Roati, and M. Inguscio, Two Atomic Species Superfluid, Physical Review Letters **89**, 190404 (2002).

[160] D. M. Brink and C. V. Sukumar, Majorana spin-flip transitions in a magnetic trap, Physical Review A **74**, 035401 (2006).

[161] T. Esslinger, I. Bloch, and T. W. Hänsch, Bose-Einstein condensation in a quadrupole-Ioffe-configuration trap, Physical Review A **58**, R2664–R2667 (1998).

[162] G. Reinaudi, T. Lahaye, Z. Wang, and D. Guéry-Odelin, Strong saturation absorption imaging of dense clouds of ultracold atoms, Optics Letters **32**, 3143–3145 (2007).

[163] M. G. Skou, Quantum Impurity Dynamics and Formation of Polarons and Bipolarons in Bose-Einstein Condensates (Aarhus University, 2021).

[164] A. Altmeyer, S. Riedl, C. Kohstall, M. J. Wright, R. Geursen, M. Bartenstein, C. Chin, J. H. Denschlag, and R. Grimm, Precision Measurements of Collective Oscillations in the BEC-BCS Crossover, Physical Review Letters **98**, 040401 (2007).

[165] M. Scherer, B. Lücke, J. Peise, O. Topic, G. Gebreyesus, F. Deuretzbacher, W. Ertmer, L. Santos, C. Klempt, and J. J. Arlt, Spontaneous symmetry breaking in spinor Bose-Einstein condensates, Physical Review A **88**, 053624 (2013).

[166] D. S. Lobser, A. E. S. Barentine, E. A. Cornell, and H. J. Lewandowski, Observation of a persistent non-equilibrium state in cold atoms, Nature Physics **11**, 1009–1012 (2015).

[167] G. Baym and C. Pethick, Landau Fermi-liquid theory: concepts and applications (John Wiley & Sons, 2008).

[168] P. A. Lee, N. Nagaosa, and X.-G. Wen, Doping a Mott insulator: Physics of high-temperature superconductivity, Reviews of Modern Physics **78**, 17–85 (2006).

[169] N. Mannella, W. L. Yang, X. J. Zhou, H. Zheng, J. F. Mitchell, J. Zaanen, T. P. Devereaux, N. Nagaosa, Z. Hussain, and Z.-X. Shen, Nodal quasiparticle in pseudogapped colossal magnetoresistive manganites, Nature **438**, 474–478 (2005).

[170] M. E. Gershenson, V. Podzorov, and A. F. Morpurgo, Colloquium: Electronic transport in single-crystal organic transistors, Reviews of Modern Physics **78**, 973–989 (2006).

[171] A. S. Alexandrov and J. T. Devreese, Advances in polaron physics, Vol. 159 (Springer, 2010).

[172] P. Massignan, M. Zaccanti, and G. M. Bruun, Polarons, dressed molecules and itinerant ferromagnetism in ultracold Fermi gases, Reports on Progress in Physics **77**, 034401 (2014).

[173] R. Schmidt, M. Knap, D. A. Ivanov, J.-S. You, M. Cetina, and E. Demler, Universal many-body response of heavy impurities coupled to a Fermi sea: a review of recent progress, Reports on Progress in Physics **81**, 024401 (2018).

[174] P. W. Anderson, Infrared Catastrophe in Fermi Gases with Local Scattering Potentials, Physical Review Letters **18**, 1049–1051 (1967).

[175] J. Kondo, Resistance Minimum in Dilute Magnetic Alloys, Progress of Theoretical Physics **32**, 37–49 (1964).

[176] F. Scazza, G. Valtolina, P. Massignan, A. Recati, A. Amico, A. Burchianti, C. Fort, M. Inguscio, M. Zaccanti, and G. Roati, Repulsive Fermi Polarons in a Resonant Mixture of Ultracold ^{6}Li Atoms, Physical Review Letters **118**, 083602 (2017).

[177] S. Ospelkaus, C. Ospelkaus, O. Wille, M. Succo, P. Ernst, K. Sengstock, and K. Bongs, Localization of Bosonic Atoms by Fermionic Impurities in a Three-Dimensional Optical Lattice, Physical Review Letters **96**, 180403 (2006).

[178] R. Scelle, T. Rentrop, A. Trautmann, T. Schuster, and M. K. Oberthaler, Motional Coherence of Fermions Immersed in a Bose Gas, Physical Review Letters **111**, 070401 (2013).

[179] T. Rentrop, A. Trautmann, F. A. Olivares, F. Jendrzejewski, A. Komnik, and M. K. Oberthaler, Observation of the Phononic Lamb Shift with a Synthetic Vacuum, Physical Review X **6**, 041041 (2016).

[180] N. Spethmann, F. Kindermann, S. John, C. Weber, D. Meschede, and A. Widera, Dynamics of Single Neutral Impurity Atoms Immersed in an Ultracold Gas, Physical Review Letters **109**, 235301 (2012).

[181] J. Catani, G. Lamporesi, D. Naik, M. Gring, M. Inguscio, F. Minardi, A. Kantian, and T. Giamarchi, Quantum dynamics of impurities in a one-dimensional Bose gas, Physical Review A **85**, 023623 (2012).

[182] F. Meinert, M. Knap, E. Kirilov, K. Jag-Lauber, M. B. Zvonarev, E. Demler, and H.-C. Nägerl, Bloch oscillations in the absence of a lattice, Science **356**, 945–948 (2017).

[183] Y. E. Shchadilova, R. Schmidt, F. Grusdt, and E. Demler, Quantum Dynamics of Ultracold Bose Polarons, Physical Review Letters **117**, 113002 (2016).

[184] K. K. Nielsen, L. A. P. Ardila, G. M. Bruun, and T. Pohl, Critical slowdown of non-equilibrium polaron dynamics, New Journal of Physics **21**, 043014 (2019).

[185] S. I. Mistakidis, G. C. Katsimiga, G. M. Koutentakis, T. Busch, and P. Schmelcher, Quench Dynamics and Orthogonality Catastrophe of Bose Polarons, Physical Review Letters **122**, 183001 (2019).

[186] M. Drescher, M. Salmhofer, and T. Enss, Theory of a resonantly interacting impurity in a Bose-Einstein condensate, Physical Review Research **2**, 032011 (2020).

[187] M. Drescher, M. Salmhofer, and T. Enss, Quench Dynamics of the Ideal Bose Polaron at Zero and Nonzero Temperatures, Physical Review A **103**, 033317 (2021).

[188] M. M. Parish and J. Levinsen, Quantum dynamics of impurities coupled to a Fermi sea, Physical Review B **94**, 184303 (2016).

[189] R. J. Fletcher, R. Lopes, J. Man, N. Navon, R. P. Smith, M. W. Zwierlein, and Z. Hadzibabic, Two- and three-body contacts in the unitary Bose gas, Science **355**, 377–380 (2017).

[190] C. Gross, Spin squeezing, entanglement and quantum metrology with Bose–Einstein condensates, Journal of Physics B: Atomic, Molecular and Optical Physics **45**, 103001 (2012).

[191] E. Braaten, D. Kang, and L. Platter, Short-Time Operator Product Expansion for rf Spectroscopy of a Strongly Interacting Fermi Gas, Physical Review Letters **104**, 223004 (2010).

[192] S. P. Rath and R. Schmidt, Field-theoretical study of the Bose polaron, Physical Review A **88**, 053632 (2013).

[193] M. Knap, A. Shashi, Y. Nishida, A. Imambekov, D. A. Abanin, and E. Demler, Time-Dependent Impurity in Ultracold Fermions: Orthogonality Catastrophe and Beyond, Physical Review X **2**, 041020 (2012).

[194] A. Sommer, M. Ku, and M. W. Zwierlein, Spin transport in polaronic and superfluid Fermi gases, New Journal of Physics **13**, 055009 (2011).

[195] A. B. Bardon, S. Beattie, C. Luciuk, W. Cairncross, D. Fine, N. S. Cheng, G. J. A. Edge, E. Taylor, S. Zhang, S. Trotzky, and J. H. Thywissen, Transverse Demagnetization Dynamics of a Unitary Fermi Gas, Science **344**, 722–724 (2014).

[196] A. Camacho-Guardian, L. A. Peña Ardila, T. Pohl, and G. M. Bruun, Bipolarons in a Bose-Einstein Condensate, Physical Review Letters **121**, 013401 (2018).

[197] S. M. Yoshida, S. Endo, J. Levinsen, and M. M. Parish, Universality of an Impurity in a Bose-Einstein Condensate, Physical Review X **8**, 011024 (2018).

[198] N. Navon, R. P. Smith, and Z. Hadzibabic, Quantum Gases in Optical Boxes, arXiv:12106.09716 (2021).

[199] Y.-i. Shin, A. Schirotzek, C. H. Schunck, and W. Ketterle, Realization of a Strongly Interacting Bose-Fermi Mixture from a Two-Component Fermi Gas, Physical Review Letters **101**, 070404 (2008).

[200] N. Navon, S. Piatecki, K. Günter, B. Rem, T. C. Nguyen, F. Chevy, W. Krauth, and C. Salomon, Dynamics and Thermodynamics of the Low-Temperature Strongly Interacting Bose Gas, Physical Review Letters **107**, 135301 (2011).

[201] S. B. Papp, J. M. Pino, R. J. Wild, S. Ronen, C. E. Wieman, D. S. Jin, and E. A. Cornell, Bragg Spectroscopy of a Strongly Interacting ^{85}Rb Bose-Einstein Condensate, Physical Review Letters **101**, 135301 (2008).

[202] D. M. Larsen, Binary mixtures of dilute bose gases with repulsive interactions at low temperature, Annals of Physics **24**, 89–101 (1963).

[203] F. Minardi, F. Ancilotto, A. Burchianti, C. D'Errico, C. Fort, and M. Modugno, Effective expression of the Lee-Huang-Yang energy functional for heteronuclear mixtures, Physical Review A **100**, 063636 (2019).

[204] M.-O. Mewes, M. R. Andrews, N. J. van Druten, D. M. Kurn, D. S. Durfee, C. G. Townsend, and W. Ketterle, Collective Excitations of a Bose-Einstein Condensate in a Magnetic Trap, Physical Review Letters **77**, 988–991 (1996).

[205] D. M. Stamper-Kurn, H.-J. Miesner, S. Inouye, M. R. Andrews, and W. Ketterle, Collisionless and Hydrodynamic Excitations of a Bose-Einstein Condensate, Physical Review Letters **81**, 500–503 (1998).

[206] D. S. Jin, J. R. Ensher, M. R. Matthews, C. E. Wieman, and E. A. Cornell, Collective Excitations of a Bose-Einstein Condensate in a Dilute Gas, Physical Review Letters **77**, 420–423 (1996).

[207] D. S. Jin, M. R. Matthews, J. R. Ensher, C. E. Wieman, and E. A. Cornell, Temperature-Dependent Damping and Frequency Shifts in Collective Excitations of a Dilute Bose-Einstein Condensate, Physical Review Letters **78**, 764–767 (1997).

[208] S. Stringari, Collective Excitations of a Trapped Bose-Condensed Gas, Physical Review Letters **77**, 2360–2363 (1996).

[209] M. Edwards, P. A. Ruprecht, K. Burnett, R. J. Dodd, and C. W. Clark, Collective Excitations of Atomic Bose-Einstein Condensates, Physical Review Letters **77**, 1671–1674 (1996).

[210] F. Dalfovo, C. Minniti, and L. P. Pitaevskii, Frequency shift and mode coupling in the nonlinear dynamics of a Bose-condensed gas, Physical Review A **56**, 4855–4863 (1997).

[211] G. Natale, R. M. W. van Bijnen, A. Patscheider, D. Petter, M. J. Mark, L. Chomaz, and F. Ferlaino, Excitation Spectrum of a Trapped Dipolar Supersolid and Its Experimental Evidence, Physical Review Letters **123**, 050402 (2019).

[212] L. Tanzi, J. G. Maloberti, G. Biagioni, A. Fioretti, C. Gabbanini, and G. Modugno, Evidence of superfluidity in a dipolar supersolid from nonclassical rotational inertia, Science **371**, 1162–1165 (2021).

[213] E. Tiemann, P. Gersema, K. K. Voges, T. Hartmann, A. Zenesini, and S. Ospelkaus, Beyond Born-Oppenheimer approximation in ultracold atomic collisions, Physical Review Research **2**, 013366 (2020).

[214] F. Ancilotto, M. Barranco, M. Guilleumas, and M. Pi, Self-bound ultradilute Bose mixtures within local density approximation, Physical Review A **98**, 053623 (2018).

[215] H. Hu and X.-J. Liu, Consistent Theory of Self-Bound Quantum Droplets with Bosonic Pairing, Physical Review Letters **125**, 195302 (2020).

[216] S. Lepoutre, L. Fouché, A. Boissé, G. Berthet, G. Salomon, A. Aspect, and T. Bourdel, Production of strongly bound ^{39}K bright solitons, Physical Review A **94**, 053626 (2016).

[217] V. Cikojević, L. V. Markić, M. Pi, M. Barranco, and J. Boronat, Towards a quantum Monte Carlo–based density functional including finite-range effects: Excitation modes of a ^{39}K quantum droplet, Physical Review A **102**, 033335 (2020).

[218] H. Hu and X.-J. Liu, Collective excitations of a spherical ultradilute quantum droplet, Physical Review A **102**, 053303 (2020).

[219] L. Lavoine, A. Hammond, A. Recati, D. Petrov, and T. Bourdel, Beyond-mean-field effects in Rabi-coupled two-component Bose-Einstein condensate, arXiv:2105.11723 (2021).

[220] C. Ospelkaus and S. Ospelkaus, Heteronuclear quantum gas mixtures, Journal of Physics B: Atomic, Molecular and Optical Physics **41**, 203001 (2008).

[221] A. L. Fetter and J. D. Walecka, Quantum Theory of Many-particle Systems (Courier Corporation, June 20, 2003), 646 pp.

[222] R. S. Christensen, J. Levinsen, and G. M. Bruun, Quasiparticle Properties of a Mobile Impurity in a Bose-Einstein Condensate, Physical Review Letters **115**, 160401 (2015).

[223] L. Khaykovich, F. Schreck, G. Ferrari, T. Bourdel, J. Cubizolles, L. D. Carr, Y. Castin, and C. Salomon, Formation of a Matter-Wave Bright Soliton, Science **296**, 1290–1293 (2002).

[224] T. Weber, J. Herbig, M. Mark, H.-C. Nägerl, and R. Grimm, Bose-Einstein Condensation of Cesium, Science **299**, 232–235 (2003).

[225] T. Kraemer, J. Herbig, M. Mark, T. Weber, C. Chin, H.-C. Nägerl, and R. Grimm, Optimized production of a cesium Bose–Einstein condensate, Applied Physics B **79**, 1013–1019 (2004).

[226] G. Roati, M. Zaccanti, C. D'Errico, J. Catani, M. Modugno, A. Simoni, M. Inguscio, and G. Modugno, ^{39}K Bose-Einstein

Condensate with Tunable Interactions, Physical Review Letters **99**, 010403 (2007).

[227] M. Fattori, C. D'Errico, G. Roati, M. Zaccanti, M. Jona-Lasinio, M. Modugno, M. Inguscio, and G. Modugno, Atom Interferometry with a Weakly Interacting Bose-Einstein Condensate, Physical Review Letters **100**, 080405 (2008).

[228] M. Gustavsson, E. Haller, M. J. Mark, J. G. Danzl, G. Rojas-Kopeinig, and H.-C. Nägerl, Control of Interaction-Induced Dephasing of Bloch Oscillations, Physical Review Letters **100**, 080404 (2008).

[229] T. Lahaye, T. Koch, B. Fröhlich, M. Fattori, J. Metz, A. Griesmaier, S. Giovanazzi, and T. Pfau, Strong dipolar effects in a quantum ferrofluid, Nature **448**, 672–675 (2007).

[230] S. E. Pollack, D. Dries, M. Junker, Y. P. Chen, T. A. Corcovilos, and R. G. Hulet, Extreme Tunability of Interactions in a Li 7 Bose-Einstein Condensate, Physical Review Letters **102**, 090402 (2009).

[231] S. Zhu and S. Tan, Three-body scattering hypervolumes of particles with short-range interactions, arXiv:1710.04147 (2021).

[232] E. Braaten and H. .-. Hammer, Universality in few-body systems with large scattering length, Physics Reports **428**, 259–390 (2006).

[233] A. Derevianko, W. R. Johnson, M. S. Safronova, and J. F. Babb, High-Precision Calculations of Dispersion Coefficients, Static Dipole Polarizabilities, and Atom-Wall Interaction Constants for Alkali-Metal Atoms, Physical Review Letters **82**, 3589–3592 (1999).

[234] S. Falke, H. Knöckel, J. Friebe, M. Riedmann, E. Tiemann, and C. Lisdat, Potassium ground-state scattering parameters and Born-Oppenheimer potentials from molecular spectroscopy, Physical Review A **78**, 012503 (2008).

[235] R. Chapurin, Precise Measurements of Few-Body Physics in Ultracold ^{39}K Bose Gas (University of Colorado, 2019).

[236] R. J. Fletcher, A. L. Gaunt, N. Navon, R. P. Smith, and Z. Hadzibabic, Stability of a Unitary Bose Gas, Physical Review Letters **111**, 125303 (2013).

[237] M. Hans, F. Schmutte, C. Viermann, N. Liebster, M. Sparn, M. K. Oberthaler, and H. Strobel, High signal to noise absorption imaging of alkali atoms at moderate magnetic fields, Review of Scientific Instruments **92**, 023203 (2021).

[238] A. Banerjee and V. Natarajan, Absolute-frequency measurements of the D_2 line and fine-structure interval in ^{39}K, Physical Review A **70**, 052505 (2004).

[239] W. Demtröder, Atoms, Molecules and Photons, 2nd Edition (Springer, 2010).

[240] M. Zaccanti, C. D'Errico, F. Ferlaino, G. Roati, M. Inguscio, and G. Modugno, Control of the interaction in a Fermi-Bose mixture, Physical Review A **74**, 041605 (2006).

[241] G. Thalhammer, G. Barontini, L. De Sarlo, J. Catani, F. Minardi, and M. Inguscio, Double Species Bose-Einstein Condensate with Tunable Interspecies Interactions, Physical Review Letters **100**, 210402 (2008).

[242] T. Kraemer, M. Mark, P. Waldburger, J. G. Danzl, C. Chin, B. Engeser, A. D. Lange, K. Pilch, A. Jaakkola, H.-C. Nägerl, and R. Grimm, Evidence for Efimov quantum states in an ultracold gas of caesium atoms, Nature **440**, 315–318 (2006).

[243] M. G. Skou, K. K. Nielsen, T. G. Skov, A. M. Morgen, N. B. Jørgensen, A. Camacho-Guardian, T. Pohl, G. M. Bruun, and J. J. Arlt, Life and Death of the Bose Polaron, in preparation.

[244] A. Camacho-Guardian and G. M. Bruun, Landau Effective Interaction between Quasiparticles in a Bose-Einstein Condensate, Physical Review X **8**, 031042 (2018).

[245] J. T. Devreese and A. S. Alexandrov, Fröhlich polaron and bipolaron: recent developments, Reports on Progress in Physics **72**, 066501 (2009).

[246] A. L. Gaunt, T. F. Schmidutz, I. Gotlibovych, R. P. Smith, and Z. Hadzibabic, Bose-Einstein Condensation of Atoms in a Uniform Potential, Physical Review Letters **110**, 200406 (2013).

[247] B. Mukherjee, Z. Yan, P. B. Patel, Z. Hadzibabic, T. Yefsah, J. Struck, and M. W. Zwierlein, Homogeneous Atomic Fermi Gases, Physical Review Letters **118**, 123401 (2017).

[248] R. Bause, A. Schindewolf, R. Tao, M. Duda, X.-Y. Chen, G. Quéméner, T. Karman, A. Christianen, I. Bloch, and X.-Y. Luo, Collisions of ultracold molecules in bright and dark optical dipole traps, Physical Review Research **3**, 033013 (2021).

[249] L. Chomaz, L. Corman, T. Bienaimé, R. Desbuquois, C. Weitenberg, S. Nascimbène, J. Beugnon, and J. Dalibard, Emergence of coherence via transverse condensation in a uniform quasi-two-dimensional Bose gas, Nature Communications **6**, 6162 (2015).

[250] K. Hueck, N. Luick, L. Sobirey, J. Siegl, T. Lompe, and H. Moritz, Two-Dimensional Homogeneous Fermi Gases, Physical Review Letters **120**, 060402 (2018).

[251] K. Henderson, C. Ryu, C. MacCormick, and M. G. Boshier, Experimental demonstration of painting arbitrary and dynamic potentials for Bose–Einstein condensates, New Journal of Physics **11**, 043030 (2009).

[252] I. Manek, Y. B. Ovchinnikov, and R. Grimm, Generation of a hollow laser beam for atom trapping using an axicon, Optics Communications **147**, 67–70 (1998).

[253] A. P. Hansen, Cylindrical Optical Dipole Trap for Ultracold Atoms, Master’s thesis (Aarhus University, 2021).

[254] K. Shibata, H. Ikeda, R. Suzuki, and T. Hirano, Compensation of gravity on cold atoms by a linear optical potential, Physical Review Research **2**, 013068 (2020).